

# Li/Mg-Based Hydrides for High-Capacity Hydrogen and Lithium Storage Applications

Panyu Gao, Xiaoyue Zhang, Xuechun Hu, Xuebin Yu,\* Dalin Sun, Fang Fang,\* and Guanglin Xia\*

The rapid development of energy storage systems with high energy density and safety is crucial to meet the increasing demand for renewable energy storage and portable electronics. Li/Mg-based hydrides have gained significant attention for both hydrogen and lithium storage due to their lightweight composition and high hydrogen content. Recent advancements in catalytic design, thermodynamic tuning, nanostructuring, and external field-driven methods have markedly enhanced their hydrogen storage performance. For lithium storage, strategies to optimize ion transport and structural stability have improved ionic conductivity, reaction kinetics, and reversibility, enabling the development of high-performance energy storage systems. This review provides a detailed analysis of the progress, challenges, and opportunities in Li/Mg-based hydrides. It emphasizes breakthroughs in material modification, innovative synthesis methods, and performance optimization, showcasing their potential in hydrogen and lithium storage applications. Key challenges include balancing catalytic and thermodynamic regulation and exploring new driving methods for hydrogen storage, while enhancing ionic conductivity and refining doping techniques for lithium storage remain critical. By integrating insights into their dual roles, this work lays a strong foundation for the continued development and application of Li/Mg-based hydrides in next-generation energy storage technologies.

Exponential growth of electrochemical energy storage systems, particularly lithium-ion batteries (LIBs), has been witnessed over the last decade.<sup>[3]</sup> Due to the urgent need for ever-growing markets from portable electronics to grid-scale energy storage, the development of rechargeable LIBs with higher energy and power densities and higher safety is a long-standing research focus. One of the main factors that determines the energy density of LIBs is the specific capacity of the negative electrode.<sup>[4]</sup> Recently, some Li/Mg-based hydrides are capable of electrochemically reacting with Li ions via traditional conversion reactions and hence could work as the negative electrodes of LIBs with much higher theoretical capacities than the typical conversion-type anodes owing to the light weight of H atoms.<sup>[5]</sup> For example, the theoretical specific capacity of MgH<sub>2</sub> reaches 2038 mAh g<sup>-1</sup>, 5.5 times than widely adopted commercial graphite anode.<sup>[6]</sup> Moreover, the replacement of the liquid electrolyte in conventional LIBs with solid electrolytes (SEs) is regarded as an effective way to further improve their energy

densities and safety by reducing flammability. In this regard, induced by the presence of H atoms with light weight in the polyanions (e.g., [BH<sub>4</sub>]<sup>-</sup> and [B<sub>12</sub>H<sub>12</sub>]<sup>2-</sup>), an effective ion transfer based on the paddle-wheel mechanism through facile rotation of these polyanions could be realized.<sup>[7]</sup>

In addition, hydrogen is regarded as an ideal clean energy source with the highest energy content per unit mass (120 MJ kg<sup>-1</sup> H<sub>2</sub>) and the capability of producing energy without any harmful effects to the environment.<sup>[8]</sup> Unfortunately, the extremely low volumetric energy density (i.e., 0.01 MJ L<sup>-1</sup> H<sub>2</sub> at ambient conditions and 8.5 MJ L<sup>-1</sup> H<sub>2</sub> for the liquefied H<sub>2</sub>) owing to the low density of hydrogen poses a major obstacle for the development of hydrogen storage as practical energy storage technology.<sup>[9]</sup> Common ways to storage hydrogen are high-pressure compression and cryogenic H<sub>2</sub> liquefaction, which suffer from additional pressure control technology with serious risks of high-pressure over 70 MPa and the liquid boil-off problems in cryogenic systems, respectively. By comparison, the storage of hydrogen in metal hydrides realized by chemically bonding of hydrogen with metals and/or other functional atoms under moderate temperatures and pressure is regarded as an effective

## 1. Introduction

The ever-growing energy consumption leads to the excessive use of fossil fuels and thus the deteriorating environment of our earth, which has become a serious issue of urgent concern to our society and hence promotes the development of sustainable energy solutions.<sup>[1]</sup> Therefore, the development of energy storage systems that could harvest and storage energy from renewable sources, such as solar and wind energy, attract intensive attention.<sup>[2]</sup> To date, various energy storage technologies have been demonstrated for rapid and efficient energy storage/release.

P. Gao, X. Zhang, X. Hu, X. Yu, D. Sun, F. Fang, G. Xia  
Department of Materials Science  
Fudan University  
Shanghai 200433, China  
E-mail: yuxuebin@fudan.edu.cn; f\_fang@fudan.edu.cn;  
xianguanglin@fudan.edu.cn

The ORCID identification number(s) for the author(s) of this article can be found under <https://doi.org/10.1002/adfm.202425155>

DOI: 10.1002/adfm.202425155

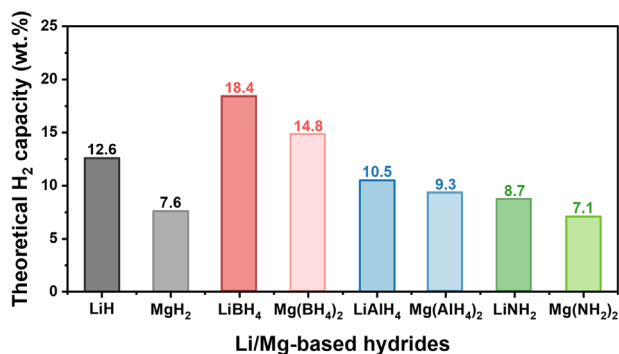


Figure 1. Theoretical H<sub>2</sub> capacity of typical Li/Mg-based hydrides.

and efficient way with higher volumetric and gravimetric storage capacities than high-pressure gaseous storage and low-temperature liquid storage methods.<sup>[10]</sup> Since 2000, considering the much lower weight of Li and Mg than most of other metals, Li and Mg-based hydrides, including LiBH<sub>4</sub>, Mg(BH<sub>4</sub>)<sub>2</sub>, LiAlH<sub>4</sub>, Mg(AlH<sub>4</sub>)<sub>2</sub>, LiNH<sub>2</sub>, Mg(NH<sub>2</sub>)<sub>2</sub>, MgH<sub>2</sub>, LiH, etc., have been widely considered as potential hydrogen storage materials owing to extremely high theoretical gravimetric and volumetric hydrogen storage densities (Figure 1).<sup>[11]</sup> Particularly, the theoretical gravimetric and volumetric hydrogen storage capacity of LiBH<sub>4</sub> reach 18.4 wt% H<sub>2</sub> and 121 kg m<sup>-3</sup>, which is five and three times higher than that of high-pressure gaseous storage of 70 MPa.<sup>[12]</sup>

Hence, it is concluded that, induced by the unique structures of H atoms with high contents, Li/Mg-based hydrides serve as a series of interesting class of energy storage materials with tunable functionalities across a broad range of applications. However, a comprehensive review regarding to the relationship between hydrogen storage and lithium storage application of Li/Mg-based hydrides has not yet been published. In this review, we will discuss the recent achievements, challenges, and opportunities of the development of Li/Mg-based hydrides for hydrogen storage and lithium storage application. In each section, the major achievements for the individual material are briefly summarized, and the remaining challenges toward their practical applications are discussed in detail.

## 2. Hydrogen Storage

Although Li/Mg-based hydrides exhibit theoretical advantages in hydrogen capacity, they typically suffer from high thermodynamic and kinetic barriers, resulting in high operating temperatures.<sup>[13]</sup> Furthermore, some hydrides, such as Mg(BH<sub>4</sub>)<sub>2</sub>, demonstrate poor reversibility, while for imides and amides, suppressing the generation of NH<sub>3</sub> by-product remains a significant challenge.<sup>[14]</sup> These issues pose major obstacles to the practical application of Li/Mg-based hydrides for hydrogen storage.

To address these challenges and improve the kinetic and thermodynamic properties of Li/Mg-based hydrides, researchers have developed various strategies to modify these materials. This section will summarize the progress and challenges in hydrogen storage using Li/Mg-based hydrides across four key approaches: catalytic modification, composite destabilization systems, na-

noengineering, and external field-driven techniques. Here, we present a timeline illustrating the application of Li/Mg-based hydrides for hydrogen storage based on the modification strategies discussed above, as shown in Figure 2.

### 2.1. Catalysis

Incorporating catalysts or additives is one of the most effective methods to reduce kinetic energy barriers, facilitating the hydrogen adsorption, dissociation, diffusion, and bonding with metal atoms. Although catalytic mechanisms vary across hydrogen storage systems, the primary mechanisms could be summarized as following effects:<sup>[15]</sup>

- 1) Hydrogen pump effect: During dehydrogenation, transition metals (TMs) preferentially bind with hydrogen atoms to form hydride clusters (TMH<sub>x</sub>) with lower energy barriers, facilitating hydrogen release from TMH<sub>x</sub> and enhancing the dehydrogenation kinetics.
- 2) Spillover effect: Hydrogen dissociate at the active sites of catalysts, which then migrate to other areas of the catalyst or nearby carriers, enhancing hydrogen storage by altering dissociation and diffusion pathways.
- 3) Channel effect: The catalysts act as transport channels for hydrogen atoms, accelerating hydrogen transfer and improving absorption/desorption rates.
- 4) Electron transfer effect: In multivalent catalysts, excess electrons generated from electron transfer processes participate in hydrogen ab-/desorption, facilitating hydrogen dissociation and recombination and thus enhancing the kinetics of the hydrogen storage system.
- 5) Nucleation induction effect: Lattice-matching catalysts to the products reduce interface nucleation energy, thereby promoting heterogeneous nucleation and being conducive to product formation on the catalyst surface.

Based on the composition, catalysts could be categorized into three types: metals, metal-based compounds, and composite materials. This section focuses on the kinetic enhancement effects and mechanisms of these catalysts in kinds of hydrogen storage systems (e.g., Mg/MgH<sub>2</sub>, borohydrides), and reviews the recent trends in catalyst design. Typical catalytic systems and hydrogen storage performance are summarized in Table 1.

#### 2.1.1. Metals

In the Mg/MgH<sub>2</sub> systems, metallic additives would manifest in three distinct forms of action:<sup>[16]</sup> i) alloying with Mg to form solid solutions, creating more hydrogen diffusion channels through interfacial stress, thereby enhancing hydrogen storage performance; ii) generating hydride clusters that function as “hydrogen pumps,” reducing the energy barriers for hydrogen ab-/desorption; iii) remaining in the unreacted elemental form, serving as a spillover catalyst to alter the hydrogen dissociation and diffusion pathways, thus enhancing hydrogen absorption kinetics.

The first group of metals, such as Ni,<sup>[17]</sup> Co,<sup>[18]</sup> and Cu,<sup>[19]</sup> form Mg-based alloys by solid solution during cycling process.

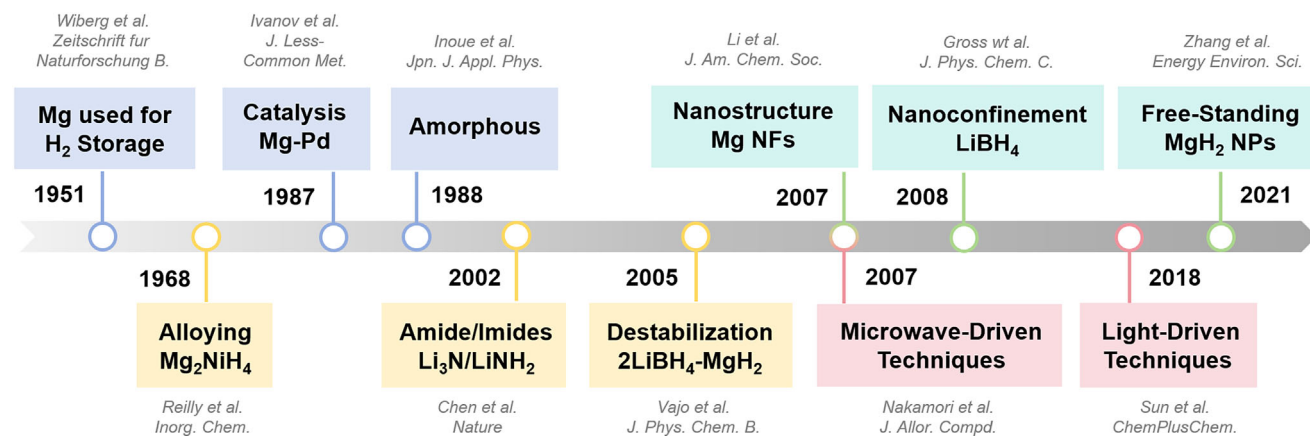


**Figure 2.** Development and corresponding milestones of Li/Mg-based materials in hydrogen storage.<sup>[59,80,90,129,227]</sup>

**Table 1.** Summary of key hydrogen storage performance indicators of various catalytic system.

Hydride	Catalyst	Doping ratio (wt%)	Dehydrogenation temperature (onset/peak, °C)	Hydrogenation performance	$E_a$ (des)/ $E_a$ (ads)	Cycling capacity	Refs.
Mg/MgH <sub>2</sub>	Ni	16.1	225/285	/	88.2/-	6.1 wt% (50th)	[20]
	Pd	5	246.5/290	2.8 MPa 275 °C 6.6 wt%	-/-	/	[233]
	Ti	10	-/317.5	3 MPa 75 °C 6.6 wt%	171/50	/	[234]
	Fe	5	177.6/222.6	3.2 MPa 200 °C 6.8 wt%	40.7/-	5.1 wt% (50th)	[235]
	Mo	1.73	217.8/310.2	3 MPa 250 °C 6.6 wt%	110.0/-	6.4 wt% (10th)	[236]
	PdNi	10	149/270	3.5 MPa 207 °C 5.7 wt%	62/74	6.3 wt% (10th)	[29]
	CuNi	10	190/245	1 MPa 250 °C 6.1 wt%	81/-	5.8 wt% (10th)	[21b]
	ZrCo	10	195/268.7	3 MPa 250 °C 6.5 wt%	90/58	5.7 wt% (10th)	[30d]
	FeCo	5	200/250.9	3.2 MPa 300 °C 6.7 wt%	65/53	6.4 wt% (10th)	[30b]
	TiVNbZrFe	10	209/227	0.5 MPa 300 °C 5.5 wt%	63/-	6.16 wt% (100th)	[32]
	V <sub>4</sub> Nb <sub>18</sub> O <sub>55</sub>	10	207/225	5 MPa 200 °C 6.0 wt%	78/-	6.0 wt% (10th)	[37]
	TiNb <sub>2</sub> O <sub>7</sub>	7	177/226	5 MPa 200 °C 6.0 wt%	96/-	6.3 wt% (10th)	[237]
	P-Li <sub>3</sub> VO <sub>4</sub>	10	214/272	3 MPa 100 °C 6.1 wt%	92/-	5.6 wt% (100th)	[238]
	HELMO-NO <sub>3</sub>	10	184.1/240	5 MPa 150 °C 6.7 wt%	54/17	6.5 wt% (50th)	[239]
	LiBH <sub>4</sub>	VNbc	10	170/235	5 MPa 200 °C 5.6 wt%	73/	5.7 wt% (10th)
Ni@C		3	233.7/285	2 MPa 275 °C 5.62 wt%	83/-	5.7 wt% (10th)	[241]
NiCoFeCuMg@C		10	167.2/289	/	112/-	5.8 wt% (20th)	[242]
TiCl <sub>3</sub>		41	100/390	7 MPa 500 °C 3.5 wt%	/	/	[39]
TiF <sub>3</sub>		32	80/110 390	7 MPa 500 °C 5.9 wt%	/	/	[39]
ZnF <sub>2</sub>		31	100/120 470	7 MPa 500 °C 4.3 wt%	/	/	[39]
TiO <sub>2</sub>		21	240/340	5 MPa 0 to 500 °C 4.3 wt%	174/-	6.7 wt% (10th)	[243]
CoB		50	175/350	/	-/-	4.8 wt% (4th)	[40]
Ni/Ni <sub>4</sub> B <sub>3</sub>		25	250/423	35 MPa 550 °C 7.9 wt%	100/-	7.9 wt% (2nd)	[244]
Ni/C		50	230/450	10 MPa 400 °C 4.1 wt%	136/-	3.7 wt% (3rd)	[52b]
Mg(BH <sub>4</sub> ) <sub>2</sub>	CoNi/C	40	130/210 355	10 MPa 400 °C 4.7 wt%	95/-	4.3 wt% (3rd)	[52a]
	NbF <sub>5</sub>	10	120/300	12 MPa 400 °C 5.5 wt%	120 182/-	4 wt% (4th)	[245]
	K <sub>2</sub> NbF <sub>7</sub>	14	118/322.6	10 MPa 280 °C 2.6 wt%	118/-	2.6 wt% (2nd)	[246]
	K <sub>2</sub> TiF <sub>6</sub>	11	105.4/333.6	10 MPa 280 °C 2.2 wt%	105/-	2.2 wt% (2nd)	[246]
	NbH <sub>x</sub> @Ti <sub>3</sub> C <sub>2</sub>	30	71.2/310	10 MPa 250 °C 5.1 wt%	106 82/-	4.2 wt% (4th)	[247]
	VF <sub>4</sub> @Ti <sub>3</sub> C <sub>2</sub>	20	90/310	9 MPa 275 °C 2.7 wt%	172/-	1.7 wt% (4th)	[248]

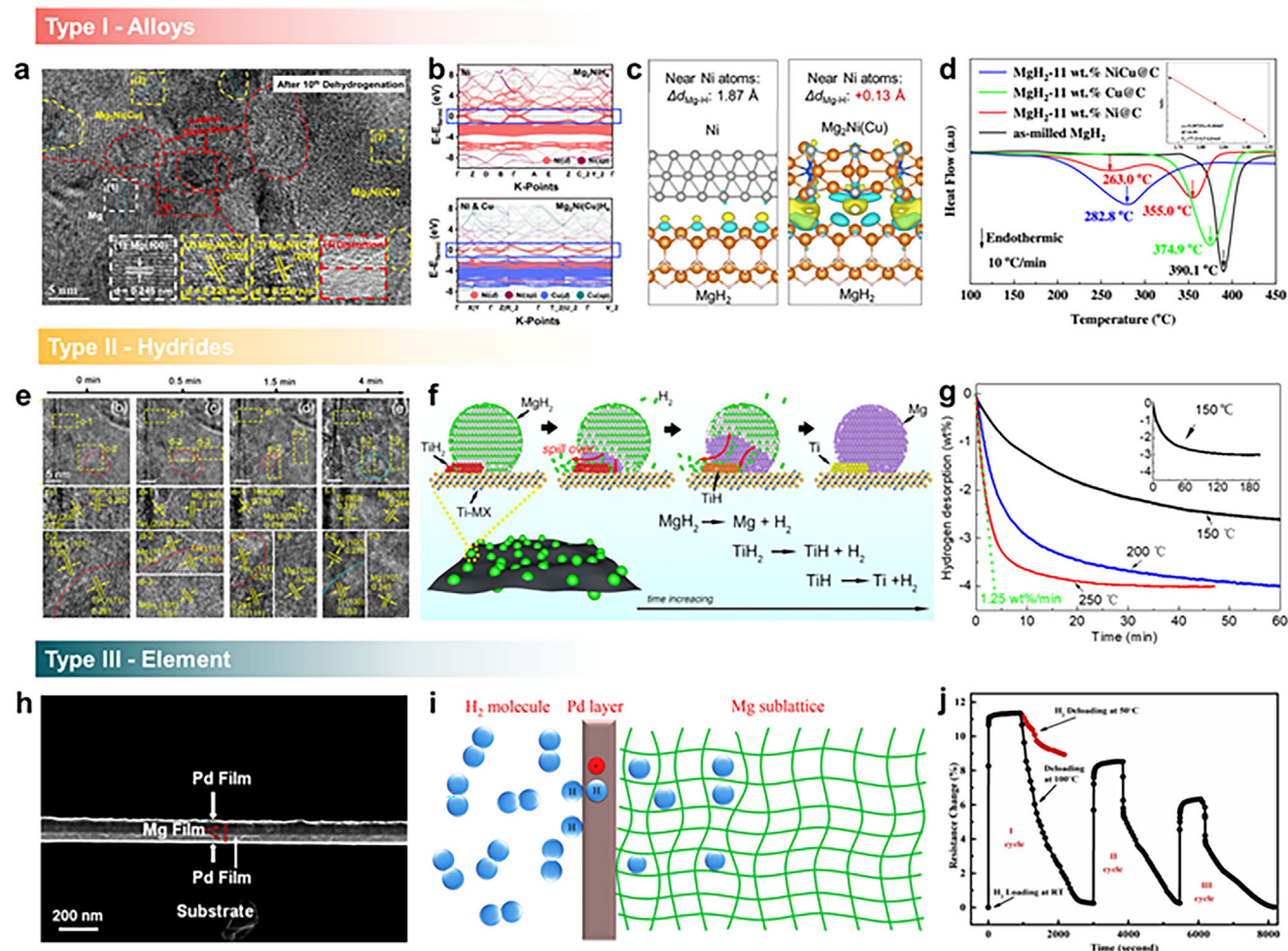


**Figure 3.** a) TEM image of  $\text{MgH}_2$  under the catalysis of  $\text{CuNi}$ . b) Band structures of  $\text{Ni}$  and  $\text{Mg}_2\text{Ni}(\text{Cu})\text{H}_4$ . c) The charge density differences of  $\text{MgH}_2$  under the catalysis of  $\text{Ni}$  and  $\text{Mg}_2\text{Ni}(\text{Cu})\text{H}_4$ . The blue area represents electron migration, while the yellow area represents electron aggregation. Reproduced with permission.<sup>[21b]</sup> Copyright 2024, Springer Nature. d) The hydrogen storage performance of  $\text{MgH}_2$  under the catalysis of  $\text{Ni}$ ,  $\text{Cu}$ , and  $\text{NiCu}$ . Reproduced with permission.<sup>[21a]</sup> Copyright 2022, Elsevier. e) In situ HRTEM images showing the evolution of the microstructure upon hydrogen desorption induced by the electron beam irradiation. f) Schematic illustration of the proposed mechanism for the fast dehydrogenation. g) Isothermal dehydrogenation curves of  $\text{MgH}_2$  at  $\text{Ti-MX}$  at different temperatures. Reproduced with permission.<sup>[26]</sup> Copyright 2021, American Chemical Society. h) FE-SEM cross-section images of as-deposited  $\text{Pd/Mg/Pd}$  tri-layers. i) Schematic diagram of reaction mechanism between hydrogen and  $\text{Pd/Mg}$  lattice. j) Resistance variation of  $\text{Pd/Mg/Pd}$  tri-layers. Reproduced with permission.<sup>[28]</sup> Copyright 2015, Elsevier.

Peng et al. demonstrated that highly dispersed  $\text{Mg}_2\text{Ni}$  alloys can be in situ formed at the interface through the hydrogenation of  $\text{NiCp}_2$ .<sup>[20]</sup> The unique  $\text{Mg}_2\text{Ni}$  alloys disrupt the periodic structure of the  $\text{Mg}$  phase at the interface and alter the lattice tension of surface  $\text{MgH}_2$ . The resulting distortion energy may enhance the ab-/desorption kinetics of  $\text{Mg/MgH}_2$  and reduce the activation energy from 160.7 to 88.2  $\text{kJ mol}^{-1}$ . Remarkably, even after 50 cycles, it could maintain a reversible hydrogen capacity of over 6 wt%  $\text{H}_2$  within 20 min. Introducing the  $\text{CuNi}$  alloy via mechanical ball milling leverages the infinite solubility between  $\text{Cu}$ ,  $\text{Ni}$  metals, and  $\text{Mg}$ , enabling the formation of  $\text{Mg}_2\text{Ni}(\text{Cu})\text{H}_4$  species, which induces additional lattice distortions due to different lattice structure with  $\text{MgH}_2$  (Figure 3a).<sup>[21]</sup> These distortions are considered to create favorable pathways for hydrogen diffusion, contributing to enhanced kinetics in hydrogen storage and release.

The addition of  $\text{Cu}$  further modifies the electronic structure of  $\text{Mg}_2\text{Ni}(\text{Cu})\text{H}_4$ , increasing the electron density of the  $d$ -band and weakening the  $\text{Mg-H}$  bond (Figure 3b,c). These adjustments reduce the dehydrogenation activation energy to 77.2  $\text{kJ mol}^{-1}$ , with hydrogen desorption initiating at 175 °C (Figure 3d,e,f).

Certain early transition metals, including  $\text{Ti}$ ,  $\text{V}$ ,  $\text{Nb}$ , and  $\text{Ce}$ , possess relatively high  $d$ -band centers and exhibit strong adsorption affinity toward hydrogen. These metals preferentially combine with  $\text{H}$  atoms to form hydride clusters. While such behavior has been considered detrimental (hydrogen poisoning) in traditional organic synthesis<sup>[22]</sup> and ammonia chemistry<sup>[23]</sup> applications, it presents advantageous properties in boosting the dehydrogenation kinetics of  $\text{Mg/MgH}_2$  system, primarily limited by the strong  $\text{Mg-H}$  bonds. When contact with  $\text{MgH}_2$ , the ionic  $\text{H}^-$  in  $\text{MgH}_2$  strongly interact with the transition metals,

forming TM–H bonds, which consequently weakens the Mg–H bonds.<sup>[24]</sup> Liang et al. compared the catalytic effects of these metals on MgH<sub>2</sub>, finding that, for dehydrogenation kinetics, V > Ti > Ni > Mn, with MgH<sub>2</sub>–V achieving an activation energy as low as 62.3 kJ mol<sup>-1</sup>, while Ti-containing systems exhibited the best hydrogenation kinetics.<sup>[25]</sup> Further studies indicated that TiH<sub>2</sub> and VH<sub>0.81</sub> formed during hydrogenation, play a crucial role for fast dehydrogenation, though the detailed mechanisms remain unclear. Zhu et al. indicated that TiH<sub>2</sub>, functioning as a “hydrogen pump” with self-dehydrogenation characteristics, decomposes into TiH and Ti during dehydrogenation, promoting Mg phase nucleation and growth (Figure 3e,f), thereby enhancing the hydrogen storage performance of the Mg/MgH<sub>2</sub> system.<sup>[26]</sup> Specifically, at 250 °C, the peak dehydrogenation rate can reach 1.25 wt% H<sub>2</sub> min<sup>-1</sup>, achieving complete dehydrogenation within 20 min (Figure 3g).

Additionally, another group of metals, including Fe and Pd, remains in their elemental form, primarily acting as spillover catalysts and enhancing hydrogen absorption kinetics in Mg by modifying the dissociation and diffusion pathways of H<sub>2</sub>.<sup>[27]</sup> For instance, in the Pd/Mg/Pd tri-layer system, with Pd and Mg layers of 10 and 50 nm thickness respectively (Figure 3h), H<sub>2</sub> dissociation occurs preferentially on the Pd film surface due to its lower hydrogen dissociation activation energy.<sup>[28]</sup> Additionally, Pd atoms alter the potential well landscape of the Mg lattice by decreasing the potential depth. Since H atoms must hop between potential wells, this adjustment facilitates H atom diffusion through the metal and lowers the binding energy required for hydride formation, as illustrated in Figure 3i. As a result, Pd/Mg/Pd system enables hydrogen absorption at room temperature under 0.2 MPa pressure within few seconds. However, the catalytic effect of Pd alone is insufficient for MgH<sub>2</sub> to desorb hydrogen at low temperatures (Figure 3j). Xu et al. developed a PdNi bimetallic alloy that leverages the electronic transfer synergy between Pd and Ni to adjust the *d*-band center, enhancing catalytic activity compared to Pd or Ni alone.<sup>[29]</sup> The activation energy for dehydrogenation decreases to 62.5 kJ mol<sup>-1</sup>, resulting in reversible hydrogen storage at near-ambient temperatures, with initiating dehydrogenation at 150 °C and achieving a high reversible capacity of 6.36 wt% H<sub>2</sub>. These findings demonstrate that the synergistic effects of multiple metals provide additional catalytic benefits, endowing MgH<sub>2</sub> with superior hydrogen storage performance.

Inspired by the superior catalytic effect of metals, recent research has shifted from the single metal catalysts to binary or multi-metal systems for obtaining better catalytic performance. Different intermetallic compounds serve varied catalytic roles, such as ZrCo and TiFe acting as “hydrogen pumps,” FeCo facilitating a “hydrogen overflow” effect, and CeNi combining hydrogen channeling with overflow catalysis.<sup>[30]</sup> In cases of sufficient abundance of metal elements, like in high-entropy alloys, the variety of introduced metal elements affects the electronic structure and surface activity of alloys to some extent. Nevertheless, the primary catalytic effect arises from the unique “cocktail effect” and numerous grain boundaries and defect structures.<sup>[31]</sup> The MgH<sub>2</sub>–TiVNbZrFe composite, with reported optimal performance, desorbs H<sub>2</sub> at ~200 °C and absorbs at room temperature.<sup>[32]</sup> However, for multi-metal catalysts, identifying the function of each component and understanding the impact of

their synergistic interactions on the microstructure pose greater challenges. Therefore, more advanced and diverse in situ characterization techniques are highly necessary (Figure 3).

Complex coordination hydrides involve both strong ionic and covalent bonds, and the hydrogen ab-/desorption processes entail intricate reaction pathways, leading to significantly higher kinetic barriers compared to metal hydrides. In Li/Mg-based borohydride systems, doped metals typically participate in the reactions, forming corresponding borides as main catalysts, which will be discussed specifically in the next section of metal-based compounds.

### 2.1.2. Metal-Based Compounds

Metal compounds, particularly multivalent transition metal compounds, which include oxides, halides, borides, and carbides, can also accelerate H<sub>2</sub> dissociation and enhance storage performance. These compounds primarily catalyze through electron transfer mechanisms, where their extra variable valence electrons facilitate electron exchange between M–H or B–H bonds, thereby lowering the energy barriers for hydrogen ab-/desorption reactions.

In metal oxides, metal cations play a pivotal catalytic role. For instance, the multivalent 3d transition metal Ti can induce electron transfer, forming various Ti-based compounds, such as Ti<sup>0</sup>, Ti<sup>2+</sup>, Ti<sup>3+</sup>, and Ti<sup>4+</sup>, upon reaction with hydrides. Interfaces among these Ti compounds are conducive to electron transfer, significantly reducing the dehydrogenation activation energies of MgH<sub>2</sub> and Mg(BH<sub>4</sub>)<sub>2</sub> from 135 and 61.1 kJ mol<sup>-1</sup> to 30.8 and 56.5 kJ mol<sup>-1</sup>, respectively.<sup>[33]</sup> This allows MgH<sub>2</sub> to desorb hydrogen at 175 °C, and enables Mg(BH<sub>4</sub>)<sub>2</sub> to achieve over 4.5 wt% reversible hydrogen capacity at 270 °C, surpassing typical hydrogen absorption limits. While Ti–H formation facilitates Mg–H bond weakening, it simultaneously introduces higher hydrogen diffusion barriers, creating new rate-determining steps.<sup>[34]</sup> Different valence states of Ti exhibit significant variations in hydrogen adsorption capacity, indicating that modulating Ti valence states could effectively regulate Ti–H bond strength.<sup>[35]</sup> Guan et al. incorporated multivalent Ti into the MgO lattice, leveraging the stable MgO framework to enhance both chemical and structural stability of the catalyst while regulating Ti–H bond strength to accelerate hydrogen diffusion. Even after 1000 cycles, it still maintains excellent dehydrogenation kinetics, achieving a hydrogen release of 5.28 wt% H<sub>2</sub> within 10 min at 280 °C.<sup>[36]</sup> Similarly, Nb and V also show catalytic potential through electron transfer. It is disclosed that Nb/V interfaces not only maximize the benefits of bimetallic catalysis but also facilitate enhanced electron transfer, with Nb weakening the Mg–H bond and V alleviating the excessively strong H adsorption by Nb (Figure 4a,b).<sup>[37]</sup> At 260 °C, such an interface enables 6.0 wt% H<sub>2</sub> release within only 5 min. Remarkably, even at room temperature, Mg catalyzed by V<sub>4</sub>Nb<sub>18</sub>O<sub>55</sub> can achieve complete hydrogenation, while bulk MgH<sub>2</sub> hardly absorbs hydrogen, suggesting that electron transfer in multi-metallic oxides can lead to synergistic catalytic effects.

The catalytic effect of halide catalysts in the Mg/MgH<sub>2</sub> system is also determined by transition metal cations, thus rendering a comparable performance to homologous oxides. However, as for borohydrides, certain halides react with borohydrides to

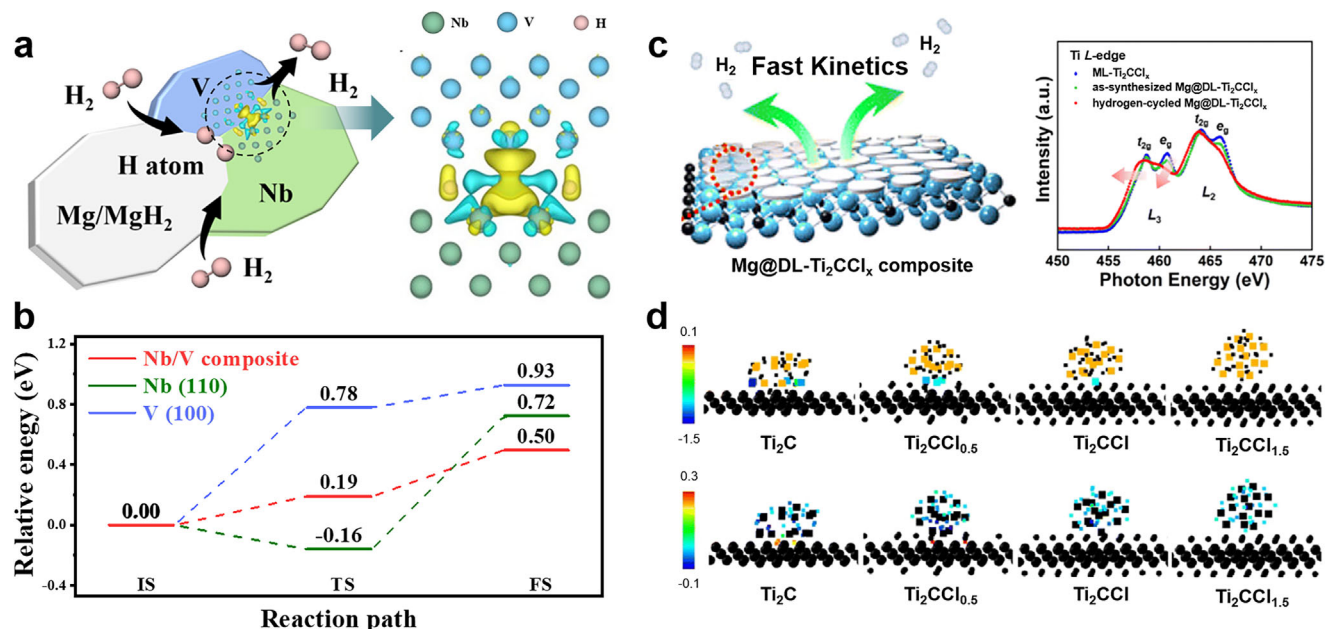


**Figure 4.** a) Charge density difference plot for the transition state of the dehydrogenation of MgH<sub>2</sub> on Nb/V composites. b) Calculated energy profiles for the H<sub>2</sub> desorption of MgH<sub>2</sub> on V (100), Nb (110), and Nb/V composites. Reproduced with permission.<sup>[37]</sup> Copyright 2022, Wiley-VCH. c) Ti L-edge NEXAFS of ML-Ti<sub>2</sub>CCl<sub>x</sub>, as-synthesized and hydrogen-cycled Mg@DL-Ti<sub>2</sub>CCl<sub>x</sub>. d) Changes in the Bader charge of Mg atoms and H atoms in the MgH<sub>2</sub>@DL-Ti<sub>2</sub>CCl<sub>x</sub> interface models evaluated based on the DFT calculations. Reddish color indicates electron loss and bluish color indicates electron gain and others are colored in black for simplicity. Reproduced with permission.<sup>[42]</sup> Copyright 2024, Royal Society of Chemistry.

form highly active metal hydrides/borides nanoparticles and induce anion exchange, which further weakens ionic and covalent bonds, providing significant catalytic advantages.<sup>[38]</sup> Au et al. discovered that doping LiBH<sub>4</sub> with TiCl<sub>3</sub>, TiF<sub>3</sub>, and ZnF<sub>2</sub> lowers the initial hydrogen release temperature to below 100 °C.<sup>[39]</sup> Specifically, LiBH<sub>4</sub> catalyzed by TiF<sub>3</sub> shows the lowest onset dehydrogenation temperature of 60 °C and achieves an impressive 5 wt% H<sub>2</sub> capacity before 100 °C. Cai et al. conducted an in-depth study on CoB, which possesses a unique uncompensated electronic structure characterized by electron-deficient B and electron-rich metal ions with a lattice structure analogous to TiB<sub>2</sub>.<sup>[40]</sup> During dehydrogenation, the electron-rich metal ions donate electrons to LiBH<sub>4</sub>, altering the charge distribution on [BH<sub>4</sub>]<sup>-</sup>, leading to structural distortion and ultimately facilitating H<sub>2</sub> release. The electron-deficient B atoms facilitate B nucleation and modify its chemical state, thereby reducing kinetic barriers. Other metal borides, such as FeB, SiB<sub>4</sub>, and Ni<sub>4</sub>B<sub>3</sub>, also exhibit similar uncompensated electronic structures and comparable catalytic effects.<sup>[41]</sup> Notably, the morphology of catalysts significantly influences charge transfer efficiency, thereby further affecting catalytic activity. Mulberry-like CoB with the highest specific surface area demonstrates the best catalytic performance, achieving 10.4 wt% H<sub>2</sub> dehydrogenation within 1 h at 350 °C and complete reversibility at 400 °C under 10 MPa hydrogen pressure.

In metal carbides/nitrides, MXenes offer unique, tunable layered structures and abundant surface functional groups, providing inherent compositional and structural advantages over other compounds. Introducing Ti-MXene into MgH<sub>2</sub> creates heterogeneous interfaces between MgH<sub>2</sub> and MXene layers, which promote localized electron rearrangement, enhancing hydrogen dissociation and recombination. Kim et al. removed -Cl

groups from the MXene surface, enabling it to act as a charge-transfer mediator, which was evidenced by Ti L-edge near edge X-ray absorption fine structure (NEXAFS), ultimately facilitating charge transfer between Mg and MXene. The t<sub>2g</sub> peaks become intense at both L<sub>2</sub> and L<sub>3</sub> edges, accompanied by a shift of the pre-edge toward the lower energy, indicating a lower oxidation state of Ti (Figure 4c). Figure 4d displays the Bader charge difference in Mg and H atoms before and after forming the MgH<sub>2</sub>@Ti<sub>2</sub>CCl<sub>x</sub> interface. The Cl-removed MXene promotes charge transfer at the interface, leading to additional electron gain for Mg and electron loss for H<sup>-</sup>, which elongates the Mg-H bond and facilitates hydrogen release, with a reduced activation energy of 57.2 kJ mol<sup>-1</sup>.<sup>[42]</sup> This demonstrates that controlling anion-anion interactions represents another effective approach to regulating the bonding strength between early transition metals and hydrogen.<sup>[43]</sup> By optimizing the concentration of surface anion defects, the hydrogen affinity of MXene-T<sub>x</sub> can be precisely tuned, effectively modulating the bonding strength between catalytic metal centers in MXene and hydrogen atoms, thus reducing hydrogen diffusion barriers.<sup>[44]</sup> The F-functional groups on the MXene also provide additional catalytic enhancement for Li/Mg-based borohydrides.<sup>[45]</sup> Fan et al. reported that LiBH<sub>4</sub>-Ti<sub>3</sub>C<sub>2</sub> composite system exhibits a dehydrogenation activation energy of only 70.3 kJ mol<sup>-1</sup>, and is capable of rapidly releasing 5.4 wt% H<sub>2</sub> at 350 °C.<sup>[46]</sup> During dehydrogenation, the formation of partially substituted LiBH<sub>3</sub>F weakens the B-H bonds and facilitates hydrogen release at lower temperatures. As the temperature increases, TiB<sub>2</sub> is gradually formed, further driving rapid dehydrogenation of LiBH<sub>4</sub>.

Among various metal additives, transition metal compounds, especially Ti-, V-, Nb-, and Ni-based compounds, demonstrate

superior catalytic effects in enhancing the hydrogen release and uptake performance of Li/Mg-based hydrogen storage materials. What is more, the catalytic activity is significantly influenced by both the macrostructure (such as particle size and morphology) and the microstructure (including crystal structure, electronic structure, defect structure, etc.). Consequently, further investigation into the structure–performance relationship and the rational design of catalysts with advantageous structures would contribute to optimizing the operating conditions of hydrogen storage materials.

### 2.1.3. Composite Materials

Researches have demonstrated that reducing the size of catalysts to the nanoscale could increase the number of exposed catalytic sites, leading to an exponential rise in catalytic activity.<sup>[47]</sup> Combining carbon materials with metal catalysts has been emerging as the most effective way to prepare nano-scaled catalysts.<sup>[48]</sup> The high surface area of carbon materials allows for high dispersion of metal/metal precursor particles, preventing agglomeration. For instance, Chen et al. designed a composite catalyst of highly dispersed ZrO<sub>2</sub> nanoparticles on a carbon matrix through sol–gel and thermal pyrolysis methods.<sup>[49]</sup> The ZrO<sub>2</sub> nanoparticles, with a size range of 5–10 nm, significantly increase contact area with hydrides, improving catalytic efficiency (Figure 5a). Compared to ZrO<sub>2</sub> without supports, ZrO<sub>2</sub>@C reduces the dehydrogenation activation energy of MgH<sub>2</sub> by 13 kJ mol<sup>-1</sup>, lowers the dehydrogenation temperature by 40 °C, and enables rapid dehydrogenation below 240 °C (Figure 5c). On the other hand, carbon materials serve as electron transport carriers, facilitating hydrogen dissociation and recombination while maintaining the stability of ZrO<sub>2</sub> nanoparticles during cycling (Figure 5b), thus retaining a reversible hydrogen capacity of 6.5 wt% H<sub>2</sub> at 260 °C. Huang et al. employed a quasi-solid template method to achieve atomic-scale loading of various metals on N-doped carbon, where single-atom catalysts exhibited superior activity than nanoscale catalysts.<sup>[50]</sup>

Catalysts for borohydrides have also been advancing toward nanoscale composite materials. Xu et al. prepared the uniform loading of highly dispersed Ni nanoparticles on graphene via hydrogen thermal reduction.<sup>[51]</sup> With a doping amount of 20%, LiBH<sub>4</sub> dehydrogenates at ~180 °C and can be rehydrogenated under the condition of 3 MPa at 400 °C. Even after 30 cycles, the hydrogen capacity remains ~9.8 wt% H<sub>2</sub>. Xia et al. introduced Ni/C and CoNi/NC into the LiBH<sub>4</sub> system, where Ni and CoNi nanoparticles were supported on a hollow porous carbon framework structure (Figure 5d), with the in situ generated Ni<sub>2</sub>B acting as the primary catalytic center, weakening the B–H bonds.<sup>[52]</sup> This reduces the hydrogen dissociation energy from 4.22 to 1.00 eV, achieving a hydrogen storage capacity of 8.86 wt% H<sub>2</sub> after ten cycles at 320 °C. As shown in Figure 5e, the alloying of CoNi further exploited the advantages of Co, reducing the hydrogen dissociation energy to as low as 0.1 eV, with an initial dehydrogenation temperature of only 130 °C and the reversible hydrogen capacity reached 9.4 wt% H<sub>2</sub> after ten cycles (Figure 5f). This series of studies reveals that the carbon matrix not only disperses the metal catalysts but also spatially confines LiBH<sub>4</sub>.

To combine nanoscale catalysis with nanoscale confinement increases the contact area between metal and hydride particles, intensifying their interaction while effectively preventing agglomeration of hydride and catalyst particles. This methodology ensures sustained high catalytic activity and improves cycling stability.

Unfortunately, carbon matrixes alone have minimal catalytic effects on hydrides and even reduce the hydrogen storage capacity. Therefore, maintaining the stability of the micro-/nanostructure of composite without carbon matrix or imparting intrinsic catalytic activity to the carbon matrix would be more beneficial for enhancing the hydrogen storage performance of hydrides. For instance, Zhu et al. synthesized ultrafine Mg–Nb@C composite hydrogen storage materials using hydrogen plasma metal reaction.<sup>[53]</sup> This composite material features 5 nm Nb particles tightly embedded in 20 nm Mg particles, encapsulated by a 2 nm amorphous carbon coating. This core–shell structure stabilizes the internal Mg–Nb structure during cycling, resulting in reduced hydrogen absorption and desorption activation energies of 58.2 and 59.7 kJ mol<sup>-1</sup>, respectively. Jia et al. introduced defect N heteroatoms into porous carbon scaffolds, transforming microporous into mesoporous materials for use in Mg(BH<sub>4</sub>)<sub>2</sub> systems as displayed in Figure 5g.<sup>[54]</sup> N-doped carbon helps weaken B–H bonds, facilitating not only the decomposition of [BH<sub>4</sub>]<sup>-</sup> but also the dissociation of the irreversible [B<sub>12</sub>H<sub>12</sub>]<sup>2-</sup> intermediate, resulting in a low initial dehydrogenation temperature of only 81.5 °C (Figure 5h,i). Benefiting from the extra spatial confinement provided by the N-doped carbon, the Mg(BH<sub>4</sub>)<sub>2</sub> system retains over 8.5 wt% H<sub>2</sub> after 20 cycles at a moderate temperature of 250 °C (Figure 5j).

### 2.1.4. Summary and Outlook

Catalytic modification is trending toward multi-component and nanosizing. First, single-component catalysts have evolved into multi-component and even high-entropy materials. This evolution significantly enriches catalyst composition and leverages synergistic effects among components, thus enhancing hydrogen storage performance. The effect of entropy increase caused by multiple components on hydrogen storage performance has gained wide attention, and further investigation is needed to reveal the underlying mechanisms. Second, nanosizing of catalysts is another effective approach to improve catalytic efficiency and atomic utilization. Nano-sized catalysts possess larger specific surface areas and more active sites compared to micron-sized counterparts, achieving simultaneous gains in both hydrogen storage performance and hydrogen capacity.

However, generalizing the mechanisms of catalytic effects still poses a massive challenge, as their microstructure and binding forms with hydrides vary significantly due to the diversity in preparation methods and experimental conditions. Therefore, it is essential to establish standardized testing protocols and employ systematic experimental designs to identify and optimize key indicators that link structure to performance. Furthermore, building a comprehensive database for these structure–performance relationships is crucial in developing universally applicable theories. This, in turn, provides a scientific basis and

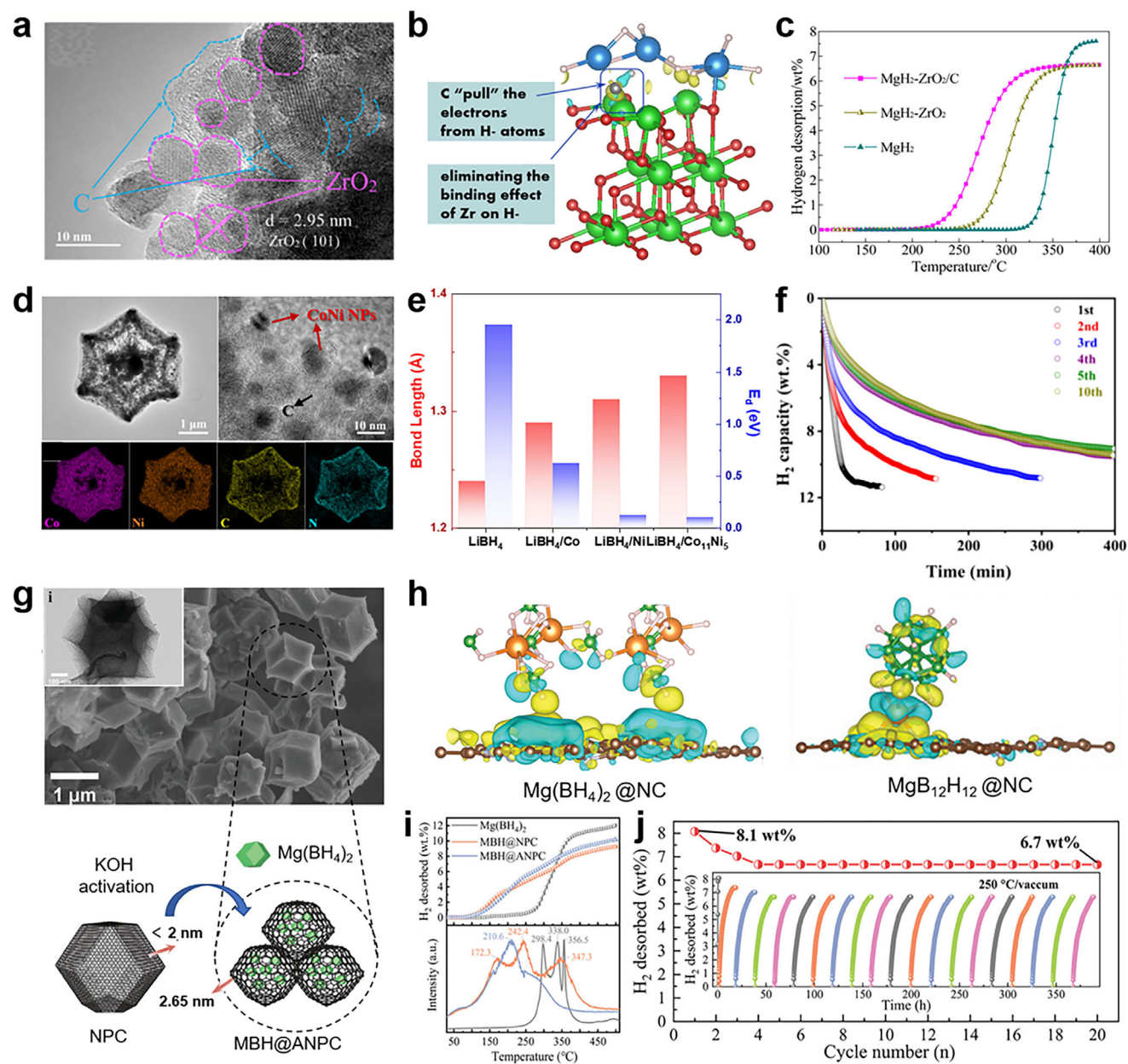


**Figure 5.** a) TEM images of ultra-fine  $\text{ZrO}_2/\text{C}$ . b) Charge density difference of  $(\text{MgH}_2)_3$  clusters interacting with  $\text{ZrO}_2/\text{C}$ . c) TPD curves of  $\text{MgH}_2$  catalyzed by  $\text{ZrO}_2/\text{C}$ ,  $\text{ZrO}_2$ , and undoped  $\text{MgH}_2$ . Reproduced with permission.<sup>[49]</sup> Copyright 2020, Elsevier. d) TEM and EDS images of  $\text{CoNi}/\text{NiC}$ . e) The average bond length of the B—H bond and  $E_d$  for  $\text{LiBH}_4$  catalyzed by Co, Ni, and  $\text{Co}_{11}\text{Ni}_5$ . f) Reversible dehydrogenation curves of  $60\text{LiBH}_4\text{—CoNi}/\text{NiC}$ . Reproduced with permission.<sup>[52a]</sup> Copyright 2024, American Chemical Society. g) Regular TEM image of ANPC and SEM image of MBH@ANPC. h) Set charge differences of  $\text{Mg}(\text{BH}_4)_2@NC$ , and  $\text{MgB}_{12}\text{H}_{12}@NC$ . i) TPD and MS curves of as-synthesized  $\text{Mg}(\text{BH}_4)_2$ , MBH@NPC, and MBH@ANPC. j) Cycling performance evaluated at  $250^\circ\text{C}$  under vacuum and 12 MPa  $\text{H}_2$ . Reproduced with permission.<sup>[228]</sup> Copyright 2024, Wiley-VCH.

theoretical guidance for catalyst design, advancing technology and innovation in hydrogen storage materials.

## 2.2. Composite Destabilization System

Constructing destabilized systems is another promising approach to improving thermodynamic properties of Li/Mg-based hydrogen storage materials. To further reduce the dehydrogena-

tion temperature, greater emphasis should be placed on thermodynamic regulation, as the intrinsic thermodynamic properties of hydrides, such as enthalpy ( $\Delta H$ ) and entropy ( $\Delta S$ ), play a critical role in determining the minimum theoretical dehydrogenation temperature.<sup>[2a]</sup>

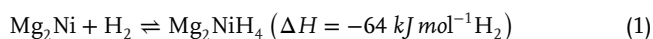
Typically, two approaches are employed to destabilize Li/Mg-based hydrides: reducing the stability of reactants and/or enhancing the stability of products, thereby decreasing the enthalpy change of the hydrogen storage reaction.<sup>[55]</sup> In this section, we

present detailed thermodynamic modification strategies for three typical types of hydride materials, magnesium-based alloys, borohydrides, and amides/imides.

### 2.2.1. Mg-Based Alloying

MgH<sub>2</sub> exhibits highly stable thermodynamic properties, with an enthalpy change as high as −74 kJ mol<sup>−1</sup>. Alloying Mg with other elements is an effective strategy to modify its thermodynamics and lower the reaction enthalpy by forming substances with reduced formation enthalpy. These substances can be broadly categorized into intermetallic compounds and multi-element alloys.<sup>[56]</sup> Specifically, intermetallic compounds alter the enthalpy change by forming phases with distinct properties, such as atomic arrangement and lattice structure, that differ significantly from those of Mg.<sup>[57]</sup> In contrast, in multi-element alloys, the alloying elements integrate into the Mg lattice as a solid solution, causing lattice distortion that disrupts the Mg lattice and indirectly reduces the enthalpy change.<sup>[58]</sup>

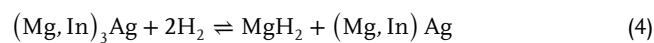
Reilly and Wiswall pioneered the use of alloying to create intermetallic compounds, enhancing the hydrogen absorption and desorption performance of Mg in the Mg–Ni system, as shown in Equation (1).<sup>[59]</sup> The reaction enthalpy change decreased from 74 to 64 kJ·mol<sup>−1</sup>, theoretically lowering the dehydrogenation temperature to 253 °C at 0.1 MPa H<sub>2</sub> pressure (Figure 6c). Due to the formation of the ternary hydride Mg<sub>2</sub>NiH<sub>4</sub> during hydrogenation, Mg–Ni system exhibits reduced thermodynamic stability and enhanced H<sub>2</sub> absorption/desorption kinetics compared to MgH<sub>2</sub>. Upon heating, in situ transmission electron microscopy (TEM) and in situ synchrotron X-ray diffraction (XRD) patterns revealed that Mg<sub>2</sub>NiH<sub>4</sub> undergoes a low-temperature (LT-) to high-temperature (HT-) phase transition in the range of 240–360 °C, which induces stress and strain, leading to partial hydrogen release (Figure 6b,e).<sup>[60]</sup> Subsequently, additional alloying elements were introduced into the Mg–Ni system to form pseudo-binary intermetallic compound, further reducing the enthalpy change.<sup>[61]</sup> For example, Liu et al. partially substituted Ni with Cr and Mn via ball milling to obtain Mg<sub>2</sub>Ni<sub>x</sub>Cr<sub>1−x</sub> and Mg<sub>2</sub>Ni<sub>x</sub>Mn<sub>1−x</sub>.<sup>[62]</sup> As the substitution levels of Cr and Mn increased, the formation enthalpy of the hydride decreased, the equilibrium pressure for dehydrogenation increased, resulting in a lower dehydrogenation temperature (Figure 6f).



Vajo and his coauthors proposed an innovative reactive hydride destabilization system by introducing Si into MgH<sub>2</sub> (i.e., MgH<sub>2</sub>–Si system).<sup>[63]</sup> MgH<sub>2</sub> reacts with Si to form Mg<sub>2</sub>Si and release H<sub>2</sub> simultaneously, which significantly reduces the dehydrogenation enthalpy to 36 kJ mol<sup>−1</sup>, as demonstrated in Equation (2). As a result, MgH<sub>2</sub>–Si system enables H<sub>2</sub> release at 200 °C with a high capacity of 5.3 wt% H<sub>2</sub>. Similarly, the element Ge, with a comparable electronic configuration, can effectively lower the dehydrogenation temperature to 130 °C.<sup>[64]</sup> However, the reversible capacity of both systems remains limited, posing challenges to their practical application.



In the strategy of forming multi-element alloys, alloying elements integrate into Mg as solid solutions, creating Mg-based solid solution alloys. Some studies have achieved improvements in dehydrogenation thermodynamics while also demonstrating promising reversible hydrogen absorption performance.<sup>[65]</sup> Notably, the Mg(In) solid solution achieves thermodynamics instability by reversibly transforming between MgH<sub>2</sub> and the disordered β-phase MgIn during the reaction process due to the similar crystal structures of MgH<sub>2</sub> and MgIn (Figure 6g).<sup>[66]</sup> It is convinced by the EDS mapping results that after dehydrogenation, the material consists of a single-phase MgIn, while after hydrogen absorption, the system consists of a dual-phase structure of MgH<sub>2</sub> and Mg<sub>3</sub>In (Figure 6h). Specifically, the Mg<sub>0.95</sub>In<sub>0.05</sub> alloy reduces the dehydrogenation enthalpy to 68 kJ mol<sup>−1</sup>, with further reductions achieved by increasing the In solubility ratio, reaching 65.2 kJ mol<sup>−1</sup> for the Mg<sub>0.9</sub>In<sub>0.1</sub> alloy (Figure 6i).<sup>[67]</sup> Similarly, elements, such as Ag and Y, have also exhibited comparable in promoting destabilization. Zhu et al. incorporated the MgIn solid solution into the Mg<sub>3</sub>Ag alloy system, demonstrating the synergistic benefits of a multi-element alloying strategy.<sup>[68]</sup> During this process, In atoms from the MgIn solid solution migrated into the Mg<sub>3</sub>Ag alloy, resulting in the formation of a Mg<sub>5.7</sub>In<sub>0.3</sub>Ag. Upon dehydrogenation, this alloy decomposes into Mg and (Mg,In)<sub>3</sub>Ag phases, further lowering the dehydrogenation enthalpy to 62.6 kJ mol<sup>−1</sup>.



Although the strategy of alloying could improve the thermodynamics of Mg-based hydrides, the resulting reaction enthalpy typically stays within the range of 60–120 kJ mol<sup>−1</sup>, making it difficult to reduce the theoretical hydrogen release temperature to below 250 °C using this approach alone.

Moreover, the introduction of higher proportions of heavier alloying elements would compromise the effective storage capacity, reducing it to below 6 wt% H<sub>2</sub>. Thus, combining alloying with other modification strategies, such as nanoengineering, holds promise for amplifying the thermodynamic destabilization effect of alloying at the nanoscale while minimizing capacity loss. For instance, Qin et al. constructed atomic-scale Mg–Zr superlattice films through semi-co-sputtering, where Zr catalysis and strain at coherent interfaces within Mg(Zr)H solid solution reduced the onset dehydrogenation temperature to ~81 °C.<sup>[69]</sup> Zhang and colleagues fabricated an Mg@Ti@Ni core-shell structured material, enabling rapid dehydrogenation at a low temperature of 220 °C.<sup>[70]</sup> Xia et al. developed a nano MgH<sub>2</sub>–Ni@Gr composite via an in situ chemical method, effectively reducing the reversible hydrogen storage temperature to around 200 °C.<sup>[71]</sup>

### 2.2.2. Destabilization of Borohydrides

Borohydrides, as typical complex metal hydrides, exhibit high thermodynamic stability due to their strong B–H covalent bonds and M<sup>n+</sup>–[BH<sub>4</sub>]<sup>−</sup> ionic bonds, resulting in dehydrogenation temperatures exceeding 400 °C.<sup>[72]</sup> To address this issue, anion/cation substitution and destabilization system construction have been developed to modulate the thermodynamic

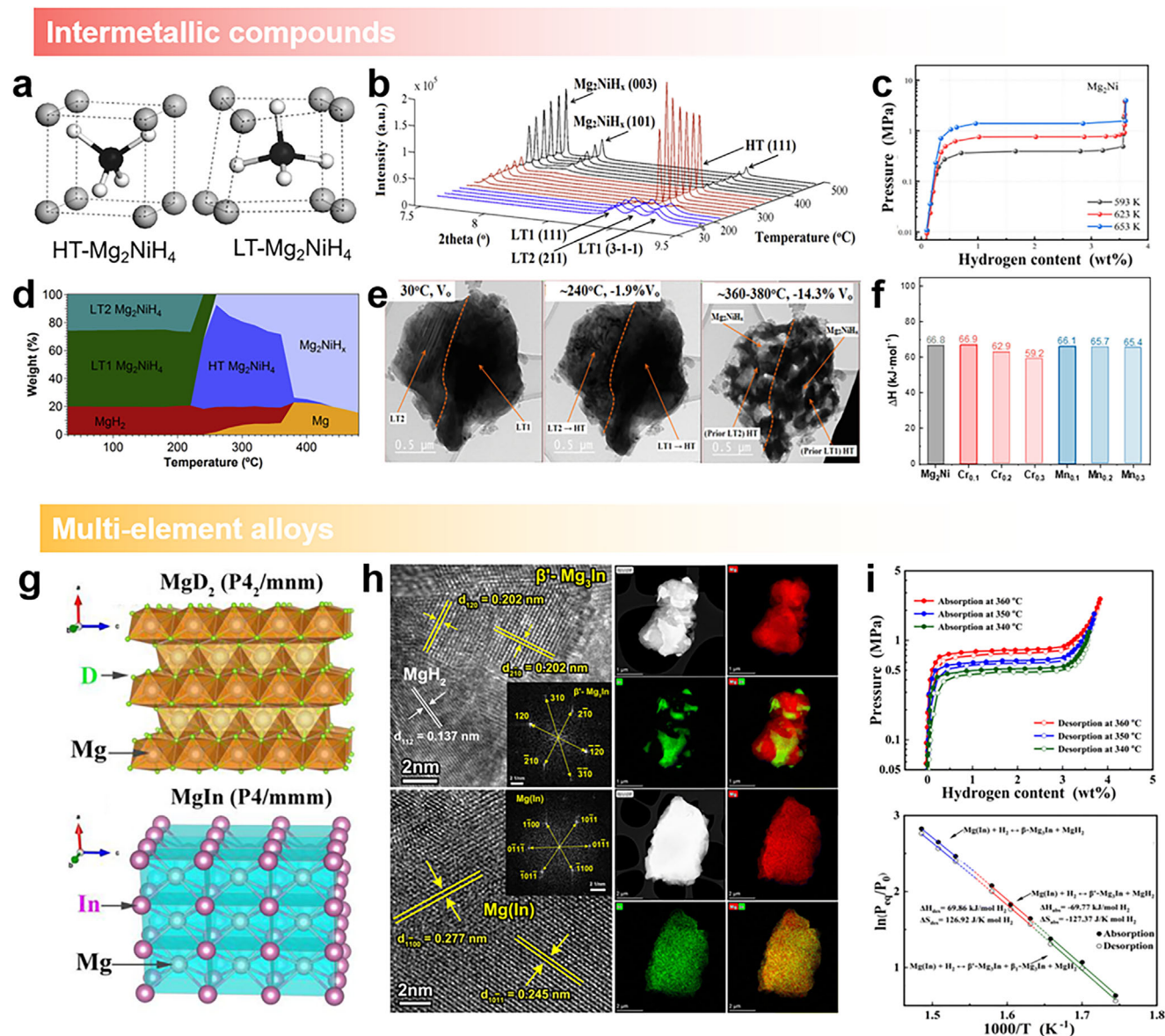


**Figure 6.** a) Local atomic structures of HT- and LT- $\text{Mg}_2\text{NiH}_4$ . Reproduced with permission.<sup>[229]</sup> Copyright 2009, Elsevier. b) In situ synchrotron XRPD 3D patterns of  $\text{Mg}_2\text{NiH}_4$  upon heating. c) PCT isotherms of  $\text{Mg}_2\text{Ni}$  alloys. d) Detailed constituent phase evolution based on XRPD analysis. e) In situ TEM images of a  $\text{Mg}_2\text{NiH}_4$  at several temperatures. Reproduced with permission.<sup>[60]</sup> Copyright 2017, Elsevier. f) Dehydrogenation activation energy ( $E_a$ ) of the partially substituted  $\text{Mg}_2\text{Ni}$  alloys. Reproduced with permission.<sup>[62]</sup> Copyright 2023, Elsevier. g) The crystal structures of  $\text{MgD}_2$  and intermetallic  $\text{MgIn}$ . Reproduced with permission.<sup>[65b]</sup> Copyright 2023, Elsevier. h) HRTEM images, HAADF-STEM images, and the corresponding EDX elemental mappings of the  $\text{Mg}_{0.9}\text{In}_{0.1}$  hydrogenated and dehydrogenated. i) PCT isotherms and Van't Hoff plots for the plateaus of  $\text{Mg}_{0.9}\text{In}_{0.1}$ . Reproduced with permission.<sup>[67]</sup> Copyright 2024, Royal Society of Chemistry.

properties.<sup>[73]</sup> Specifically, anion/cation substitution weakens ionic or covalent bonds, reducing the stability of ground-state borohydrides. While in destabilized composite systems, introducing other hydrides can trigger new reaction pathways that lead to formation of thermodynamically stable products, thereby effectively reducing the reaction enthalpy.

In terms of cation substitution, the partial replacement of Li/Mg by greater electronegativity metal elements (e.g., Zn, Cu, and Zr) can inhibit electron transfer from  $[\text{BH}_4]^-$  to Li/Mg, indicating weakened ionic bonding, which in turn, reduces the

formation enthalpy of  $\text{M}(\text{BH}_4)_n$ .<sup>[74]</sup> For example, Coudhury et al. prepared  $\text{LiMn}(\text{BH}_4)_3$  by ball milling  $\text{LiBH}_4$  with  $\text{MnCl}_2$ , releasing nearly 8.0 wt%  $\text{H}_2$  at 150 °C.<sup>[75]</sup> Other similar bimetallic cation borohydrides include  $\text{ZrLi}(\text{BH}_4)_5$ ,  $\text{LiK}(\text{BH}_4)_2$ , and  $\text{Mg}_{1-x}\text{Zn}_x(\text{BH}_4)_2$ , as listed in Table 2. As for anion substitution, halogen elements can selectively replace  $[\text{BH}_4]^-$  or  $\text{H}^-$  according to the size proximity. Specifically,  $\text{F}^-$  tends to replace  $\text{H}^-$ , whereas  $\text{Cl}^-$  prefers to substitute  $[\text{BH}_4]^-$ .<sup>[76]</sup> Density functional theory (DFT) studies suggest that, with 7%  $\text{F}^-$  substitution in  $\text{LiBH}_4$  ( $\text{LiBH}_{3.75}\text{F}_{0.25}$ ), the enthalpy change can decrease from 60.9 to

**Table 2.** Summary of reaction pathways, H<sub>2</sub> capacity, activation energy, and operating temperature of various destabilization system.

Destabilization system		Reaction pathways	H <sub>2</sub> capacity (wt%)	$\Delta H$ (kJ mol <sup>-1</sup> H <sub>2</sub> )	Operating temperature (°C)	Refs.
Mg/MgH <sub>2</sub>	Mg	Mg + H <sub>2</sub> ↔ MgH <sub>2</sub>	7.6	T75	287	[249]
	Mg <sub>2</sub> Ni	Mg <sub>2</sub> Ni + 2H <sub>2</sub> → Mg <sub>2</sub> NiH <sub>4</sub>	3.6	E65	253	[17]
	Mg <sub>2</sub> Cu	Mg <sub>2</sub> Cu + H <sub>2</sub> → MgH <sub>2</sub> + MgCu <sub>2</sub>	2.7	E72	239	[250]
	Mg <sub>2</sub> Co	Mg + Co + H <sub>2</sub> → Mg <sub>2</sub> CoH <sub>5</sub>	4.5	E86	280	[251]
	MgAl	Mg <sub>17</sub> Al <sub>12</sub> + 18H <sub>2</sub> → 4Mg <sub>2</sub> Al <sub>3</sub> + 9MgH <sub>2</sub> → 12Al + 17MgH <sub>2</sub>	4.7	T73/68	255	[252]
	Mg <sub>2</sub> Si	2MgH <sub>2</sub> + Si → Mg <sub>2</sub> Si + 2H <sub>2</sub>	5.5	T36.4	23	[63]
	Mg <sub>2</sub> Ge	MgH <sub>2</sub> + Ge → Mg <sub>2</sub> Ge + H <sub>2</sub>	3.2	E23	206	[64]
	Mg(In)	Mg(In) + H <sub>2</sub> → MgH <sub>2</sub> + β(MgIn)	5	E65	270	[66]
	Mg <sub>3</sub> La	Mg <sub>3</sub> La + H <sub>2</sub> → LaH <sub>x</sub> + MgH <sub>2</sub>	2.9	T81	296	[253]
	Mg <sub>3</sub> Nd	Mg <sub>3</sub> Nd + H <sub>2</sub> → NdH <sub>x</sub> + MgH <sub>2</sub>	2	T68	290	[254]
Borohydrides	LiMn(BH <sub>4</sub> ) <sub>3</sub>	/	11.4	/	125–160	[75]
	LiK(BH <sub>4</sub> ) <sub>2</sub>	/	10.6	/	380	[255]
	LiZn <sub>2</sub> (BH <sub>4</sub> ) <sub>5</sub>	/	9.5	/	–35–150	[74b]
	LiZr(BH <sub>4</sub> ) <sub>5</sub>	/	11.7	/	167–557	[74a]
	LiBH <sub>4</sub> –2MgH <sub>2</sub>	MgH <sub>2</sub> + 2LiBH <sub>4</sub> → Mg + 2LiBH <sub>4</sub> + H <sub>2</sub> → MgB <sub>2</sub> + 2LiH + 4H <sub>2</sub>	11.4	T50.4	186	[81]
	LiBH <sub>4</sub> –2CaH <sub>2</sub>	6LiBH <sub>4</sub> + CaH <sub>2</sub> → CaB <sub>6</sub> + 6LiH + 10H <sub>2</sub>	11.7	T45.4	146	[88a]
	LiBH <sub>4</sub> –Al	LiBH <sub>4</sub> + 1/2Al → LiH + 1/2AlB <sub>2</sub> + 3/2H <sub>2</sub>	8.6	T58	277	[256]
	LiBH <sub>4</sub> –Cr	2LiBH <sub>4</sub> + Cr → CrB <sub>2</sub> + 2LiH + 3H <sub>2</sub>	6.3	T31.7	25	[256a]
	LiBH <sub>4</sub> –LiAlH <sub>4</sub>	LiBH <sub>4</sub> + 1/2LiAlH <sub>4</sub> → 3/2LiH + 1/2AlB <sub>2</sub> + 9/4H <sub>2</sub>	11.1	E60.4	118	[257]
	LiBH <sub>4</sub> –LiNH <sub>2</sub>	LiBH <sub>4</sub> + 2LiNH <sub>2</sub> → Li <sub>3</sub> BN <sub>2</sub> + 4H <sub>2</sub>	11.9	T23	E250	[258]
Mg(BH <sub>4</sub> ) <sub>2</sub> –AlH <sub>3</sub>	2Mg(BH <sub>4</sub> ) <sub>2</sub> + 3AlH <sub>3</sub> → Mg <sub>2</sub> Al <sub>3</sub> + 4B + 25/2H <sub>2</sub>	11.9	E38	E130.8	[88b]	
Mg(BH <sub>4</sub> ) <sub>2</sub> –LiBH <sub>4</sub>	Mg(BH <sub>4</sub> ) <sub>2</sub> + 2LiBH <sub>4</sub> → MgB <sub>2</sub> + 2B + 2LiH + 7H <sub>2</sub>	14.5	T51/58/63/82	T235/315/365/460	[55b, 259]	
M–N–H	LiNH <sub>2</sub> –MgH <sub>2</sub>	2LiNH <sub>2</sub> + MgH <sub>2</sub> → Li <sub>2</sub> MgN <sub>2</sub> H <sub>2</sub> + 2H <sub>2</sub> → Mg(NH <sub>2</sub> ) <sub>2</sub> + 2LiH	5.6	T39–42	T75–85	[97]
	Mg(NH <sub>2</sub> ) <sub>2</sub> –LiH	/				[95]
	LiNH <sub>2</sub> –CaH <sub>2</sub>	2LiNH <sub>2</sub> + CaH <sub>2</sub> → Li <sub>2</sub> CaN <sub>2</sub> H <sub>2</sub> + 2H <sub>2</sub> → Ca(NH <sub>2</sub> ) <sub>2</sub> + 2LiH	4.5	T78	T100	[260]
	LiNH <sub>2</sub> –LiAlH <sub>4</sub>	2LiNH <sub>2</sub> + LiAlH <sub>4</sub> → Li <sub>3</sub> AlN <sub>2</sub> + 4H <sub>2</sub> → LiNH <sub>2</sub> + 2LiH + AlN + 2H <sub>2</sub>	9.5	T25.8/50.1	E50	[261]
	Mg(NH <sub>2</sub> ) <sub>2</sub> –KH	Mg(NH <sub>2</sub> ) <sub>2</sub> + KH → KMg(NH)(NH <sub>2</sub> ) + H <sub>2</sub>	1.4	E56	T157	[96]
	Mg(NH <sub>2</sub> ) <sub>2</sub> –CaH <sub>2</sub>	Mg(NH <sub>2</sub> ) <sub>2</sub> + CaH <sub>2</sub> → MgCa(NH <sub>2</sub> ) <sub>2</sub> + 2H <sub>2</sub>	3.9	T28.2		[262]
	LiNH <sub>2</sub> –MgH <sub>2</sub> –LiBH <sub>4</sub>	6LiNH <sub>2</sub> + 3MgH <sub>2</sub> + 2LiBH <sub>4</sub> → Li <sub>3</sub> BN <sub>2</sub> + Mg <sub>3</sub> N <sub>2</sub> + 2LiH + 6H <sub>2</sub>	8.6	E36.5	T70	[263]

T: theoretical results; E: Experimental results

36.5 kJ mol<sup>-1</sup>, corresponding to a theoretical dehydrogenation temperature of just 100 °C under 0.1 MPa H<sub>2</sub> pressure.<sup>[77]</sup> Fang et al. indicated that, in LiBH<sub>4</sub> systems, MnF<sub>2</sub> disrupts reactant stability more effectively than MnCl<sub>2</sub>. While Cl<sup>-</sup> weakens ionic bonds to some extent, F<sup>-</sup> can break the crucial B–H covalent bond, forming LiBH<sub>4-x</sub>F<sub>x</sub> that enables LiBH<sub>4</sub> to release hydrogen at 120 °C.<sup>[78]</sup>

Currently, researchers are actively exploring the synergistic effects of anion/cation co-substitution to enhance the hydrogen storage of borohydrides.<sup>[79]</sup> However, anion/cation substitution often leads to multi-phase mixtures, complicating the reaction environment and making it challenging to identify specific H<sub>2</sub> ab-/desorption pathways. Additionally, the stability of ion-

substituted structures during hydrogen absorption/desorption cycles remains uncertain, and the cyclic stability requires further experimental validation.

Constructing destabilized composite system is another effective way to lower the reaction enthalpy by introducing reactive destabilizing agents to form thermodynamically stable products before their intrinsic dehydrogenation temperature. As one of the most typical composite systems, the LiBH<sub>4</sub>–MgH<sub>2</sub> system with high theoretical capacity of 11 wt% H<sub>2</sub> was first proposed by Vajo et al. in 2005,<sup>[80]</sup> demonstrating that MgH<sub>2</sub> can participate in the hydrogen release and uptake process of LiBH<sub>4</sub>, modifying the original reaction pathway as follows:

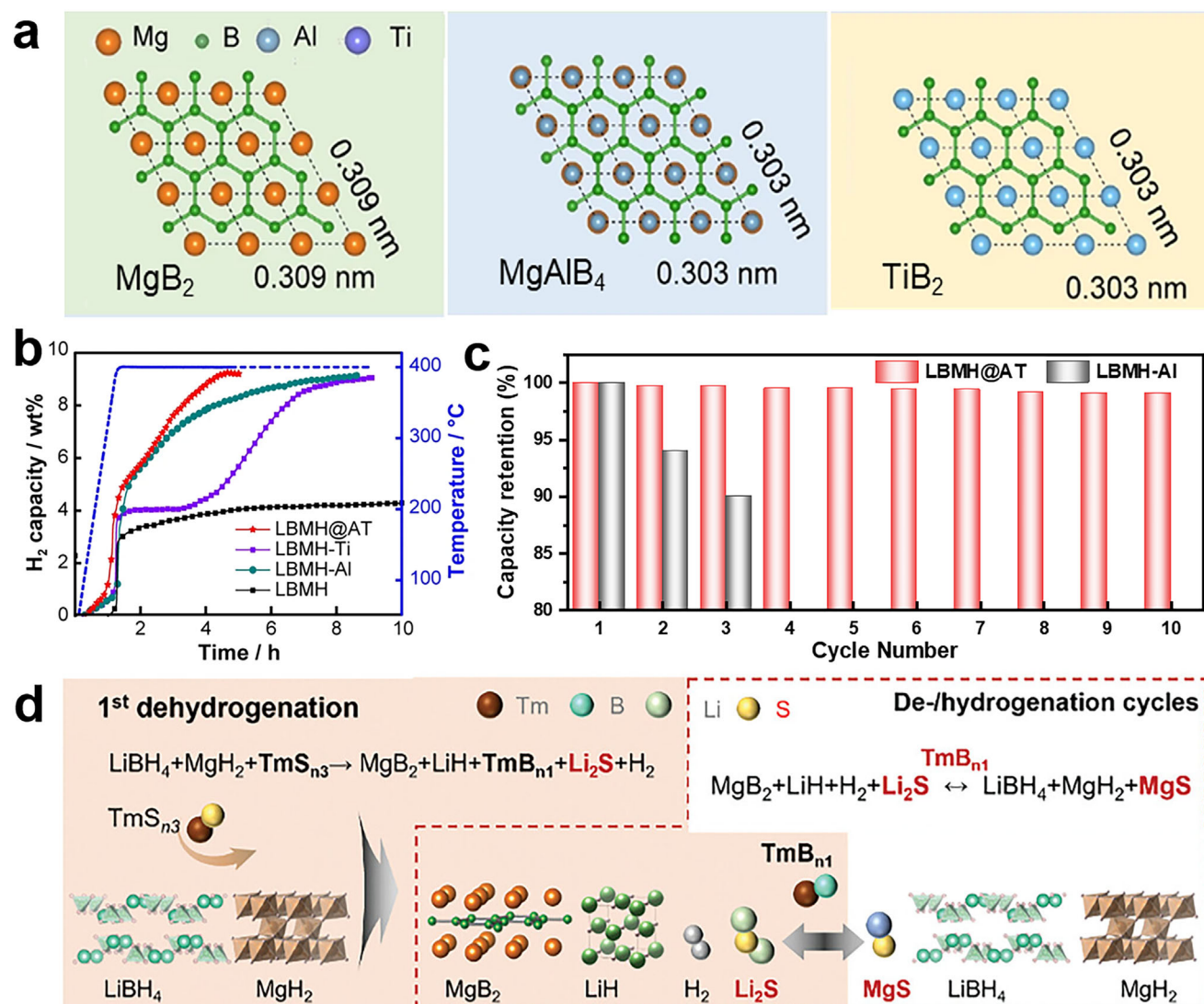
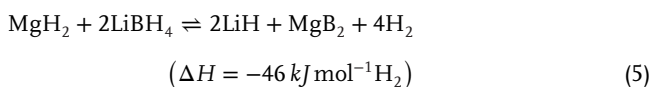


**Figure 7.** a) Close-packed-atoms arrangement of  $\text{MgB}_2$ ,  $\text{MgAlB}_4$ , and  $\text{TiB}_2$ . b) TPD hydrogen desorption curves of LBMH@AT under 0.4 MPa hydrogen pressure, with LBMH, LBMH-Al, and LBMH-Ti for comparison. c) Capacity retention of LBMH@AT at 400  $^\circ\text{C}$  for ten cycles with LBMH-Al for comparison. Reproduced with permission.<sup>[83]</sup> Copyright 2024, Springer Nature. d) Tuning anion to modulate the reversible reaction pathway of Li-RHC-catalyst composites. Reproduced with permission.<sup>[87]</sup> Copyright 2024, Wiley-VCH.



The thermodynamically stable  $\text{MgB}_2$  has a much lower formation enthalpy than B, reducing the dehydrogenation enthalpy of the system by 25  $\text{kJ mol}^{-1}$  to just 46  $\text{kJ mol}^{-1}$ . This allows the  $\text{LiBH}_4$ – $\text{MgH}_2$  system to dehydrogenate at 240  $^\circ\text{C}$  under 0.1 MPa  $\text{H}_2$  pressure.<sup>[81]</sup> Moreover, the formation of  $\text{MgB}_2$  rather than B reduces the activation energy barrier for the  $[\text{BH}_4]^-$  cluster formation and further improves the reversible hydrogen absorption performance of the system by applying a hydrogen pressure of 0.3–0.5 MPa, allowing it to maintain a reversible hydrogen capacity above 8 wt%  $\text{H}_2$  even after multiple ab-/desorption cycles.<sup>[82]</sup> During dehydrogenation, however, the system encounters chal-

lenges like a prolonged nucleation period for  $\text{MgB}_2$  and limited destabilization efficiency. Chen et al. addressed this by introducing a reactive  $\text{Al}_3\text{Ti}$  alloy, which forms  $\text{TiB}_2$  and  $\text{MgAlB}_4$  catalysts in situ during ball milling process (Figure 7a).<sup>[83]</sup> These catalysts, with lattice structures similar to  $\text{MgB}_2$ , serve as nucleation agents to induce rapid nucleation of  $\text{MgB}_2$ , allowing complete dehydrogenation within 2 h (Figure 7b). After ten cycles, the reversible hydrogen capacity remained as high as 9.2 wt%  $\text{H}_2$ , providing a crucial guidance for overcoming the high nucleation energy barrier of  $\text{MgB}_2$  and enhancing the destabilization efficiency (Figure 7c).<sup>[84]</sup> Similarly, Liu et al. reported that the amorphous  $\text{VB}_2$  exhibits a lattice mismatch of only 2.28% with  $\text{MgB}_2$ , providing effective nucleation sites for the formation of  $\text{MgB}_2$ .<sup>[85]</sup> Lu et al. demonstrated that the addition of 5 wt% layered  $\text{Nb}_2\text{C}$  MXene enables the  $\text{LiBH}_4$ – $\text{MgH}_2$  system to release 9.0 wt% of  $\text{H}_2$

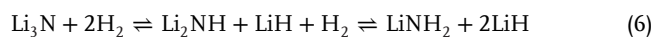
within 30 min at 400 °C, with negligible loss in reversible hydrogen storage capacity after 20 cycles.<sup>[86]</sup> Ma et al. incorporated the transition metal sulfide TiS<sub>2</sub> into the LiBH<sub>4</sub>–MgH<sub>2</sub> system, forming TiB<sub>2</sub> and Li<sub>2</sub>S, thereby fully leveraging the dual functionality of cations and anions.<sup>[87]</sup> In particular, S<sup>2-</sup> ions participates in ab-/desorption reactions in the forms of MgS and Li<sub>2</sub>S, enabling rapid Li<sup>+</sup> ions migration across the solid–solid interface (Figure 7d). This reversible transformation enhances ion mobility, resulting in a high capacity retention of 90% after 50 cycles and further boosting the destabilization efficiency.

In addition, metals or metal hydrides, like Al and CaH<sub>2</sub>, effectively destabilize the Li/Mg-based borohydrides by forming stable AlB<sub>2</sub> and CaB<sub>6</sub>, thereby reducing the reaction enthalpy change.<sup>[88]</sup> Conversely, some metals, such as Ti, V, Ce, and Sc, do not contribute to thermodynamic improvements and remain unreacted as elemental or hydride phases.<sup>[39,89]</sup> A summary of detailed information on destabilized composite systems is presented in Table 2.

Inspired by the LiBH<sub>4</sub>–MgH<sub>2</sub> systems, the issue of phase separation severely impacts the composite efficiency of the system. By promoting solid-state ion transport, however, phase separation could be minimized, which in turn, accelerates reaction kinetics, leading to a reduced dehydrogenation temperature and an enhanced cycling reversibility. Introducing nucleating agents as sites for ion migration and/or combining with nanoscale modulation to shorten diffusion paths are promising strategies to boost composite efficiency, and these approaches are expected to be central research directions.

### 2.2.3. Amide/Imides Composite System

Metal amides like LiNH<sub>2</sub> and Mg(NH<sub>2</sub>)<sub>2</sub> release NH<sub>3</sub> upon thermal decomposition, limiting their application in hydrogen storage. In 2002, Chen et al. first proposed using metal nitrides and amides/imides as hydrogen storage materials, uncovering the hydrogen storage mechanism in Li<sub>3</sub>N through a two-step reversible reaction.<sup>[90]</sup> The first hydrogenation step forms Li<sub>2</sub>NH and LiH, followed by further hydrogenation to produce LiNH<sub>2</sub> and LiH (Figure 8a).



The theoretical enthalpy changes for the two steps are –148 and –44.5 kJ mol<sup>-1</sup> H<sub>2</sub>, respectively, indicating that complete dehydrogenation from imides to Li<sub>3</sub>N requires temperatures exceeding 430 °C (Figure 8b). In comparison, the second hydrogenation step with lower enthalpy change and high hydrogen capacity of 6.5 wt% H<sub>2</sub>, is more promising for further research. Therefore, a new direction of hydrogen storage research in metal–N–H system has been created, among which LiNH<sub>2</sub>–2LiH system has been investigated first.<sup>[91]</sup>

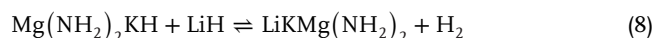
In the LiNH<sub>2</sub>–2LiH composite system, the addition of LiH mitigates NH<sub>3</sub> release from LiNH<sub>2</sub>, though the exact mechanism remains debated. Two primary theories exist: the molecularly cooperative solid-state reaction mechanism and NH<sub>3</sub>-mediated mechanism.<sup>[92]</sup> The molecularly cooperative solid-state reaction involves direct interaction between H<sup>δ+</sup> in amides and H<sup>δ-</sup> in metal hydrides, leading to dehydrogenation with lower binding

energy. In contrast, the NH<sub>3</sub>-mediated mechanism proposed by Ichikawa et al. suggests that NH<sub>3</sub> generated from LiNH<sub>2</sub> decomposition reacts with LiH, enabling N<sub>2</sub> fixation and H<sub>2</sub> release.



Although a unified dehydrogenation mechanism has yet to be established, both theories emphasize that weakening the N–H bond is critical for reducing thermodynamic stability and improving H<sub>2</sub> purity. Some researchers have attempted to substitute Li with more electronegative elements, such as Mg and Ca, extending the study to binary and ternary combinations, which strengthens interactions with N and weakens the N–H bonds, thereby in turn lowering activation energy and enthalpy for dehydrogenation.<sup>[93]</sup> The Li–Mg–N–H system is particularly promising for vehicle hydrogen storage, with a moderate enthalpy of –39 kJ mol<sup>-1</sup> H<sub>2</sub>, high hydrogen capacity of 5.6 wt% H<sub>2</sub>, and a low theoretical dehydrogenation temperature of 75 °C. In the 2LiH–Mg(NH<sub>2</sub>)<sub>2</sub> system, the hydrogen storage pathway involves the reaction of imide Li<sub>2</sub>Mg(NH)<sub>2</sub> with H<sub>2</sub>, regenerating Mg(NH<sub>2</sub>)<sub>2</sub> and LiH, thus enabling an efficient reversible cycle (Figure 8c).<sup>[94]</sup> It has been proved that in the Mg(NH<sub>2</sub>)<sub>2</sub>–LiH composite system, LiH not only effectively suppresses the release of NH<sub>3</sub> by-products but also significantly enhances the theoretical hydrogen capacity (Figure 8d).

However, slow ion migration across solid–solid interfaces leads to high diffusion energy barriers, and requires actual temperatures of 180 °C for dehydrogenation. Introducing a small amount of KH can lower dehydrogenation temperature to 107 °C (Figure 8f).<sup>[95]</sup> Wang et al. demonstrated that KH preferentially reacts with Mg(NH<sub>2</sub>)<sub>2</sub> to form K<sub>2</sub>Mg(NH<sub>2</sub>)<sub>4</sub>, which bonds with N atoms, weakening the N–H bonds and facilitating the subsequent interaction with LiH (Figure 8e).<sup>[96]</sup> Notably, during this process, KH is regenerated and continues to release hydrogen, thereby facilitating a more advantageous energy transition pathway. Functioning as a carrier for both N and H, KH accelerates atomic migration at solid–solid interfaces, achieving kinetic and thermodynamic dual regulation, thereby altering the dehydrogenation pathway as follows:



Studies have confirmed that K<sup>+</sup> cations play a vital role in the improvement. Similarly, Li et al. found that halide anions, like Br<sup>-</sup>, also engage in the reaction. In the LiNH<sub>2</sub>–MgH<sub>2</sub>–0.05LiBr composite system, LiBr undergoes an exothermic reaction with LiNH<sub>2</sub> during hydrogen release, resulting in the formation of Li<sub>7</sub>(NH<sub>2</sub>)<sub>6</sub>Br.<sup>[97]</sup> This reaction weakens the N–H bonds and facilitate Li<sup>+</sup> ion migration, just like the effect of KH, thereby lowering the initial dehydrogenation temperature to 120 °C.

Current findings suggest that enhancing amide reactivity and speeding up small-sized ion diffusion at solid–solid interfaces are essential for improving hydrogen storage performance in metal–N–H systems.<sup>[98]</sup> These can be achieved through composition adjustment (e.g., adding active catalysts and/or reactivity destabilizers), nanoengineering modulation, and microstructure construction.<sup>[99]</sup> However, considerable debate remains regarding the specific hydrogen storage mechanism. A thorough understanding of structural changes during hydrogen absorption and

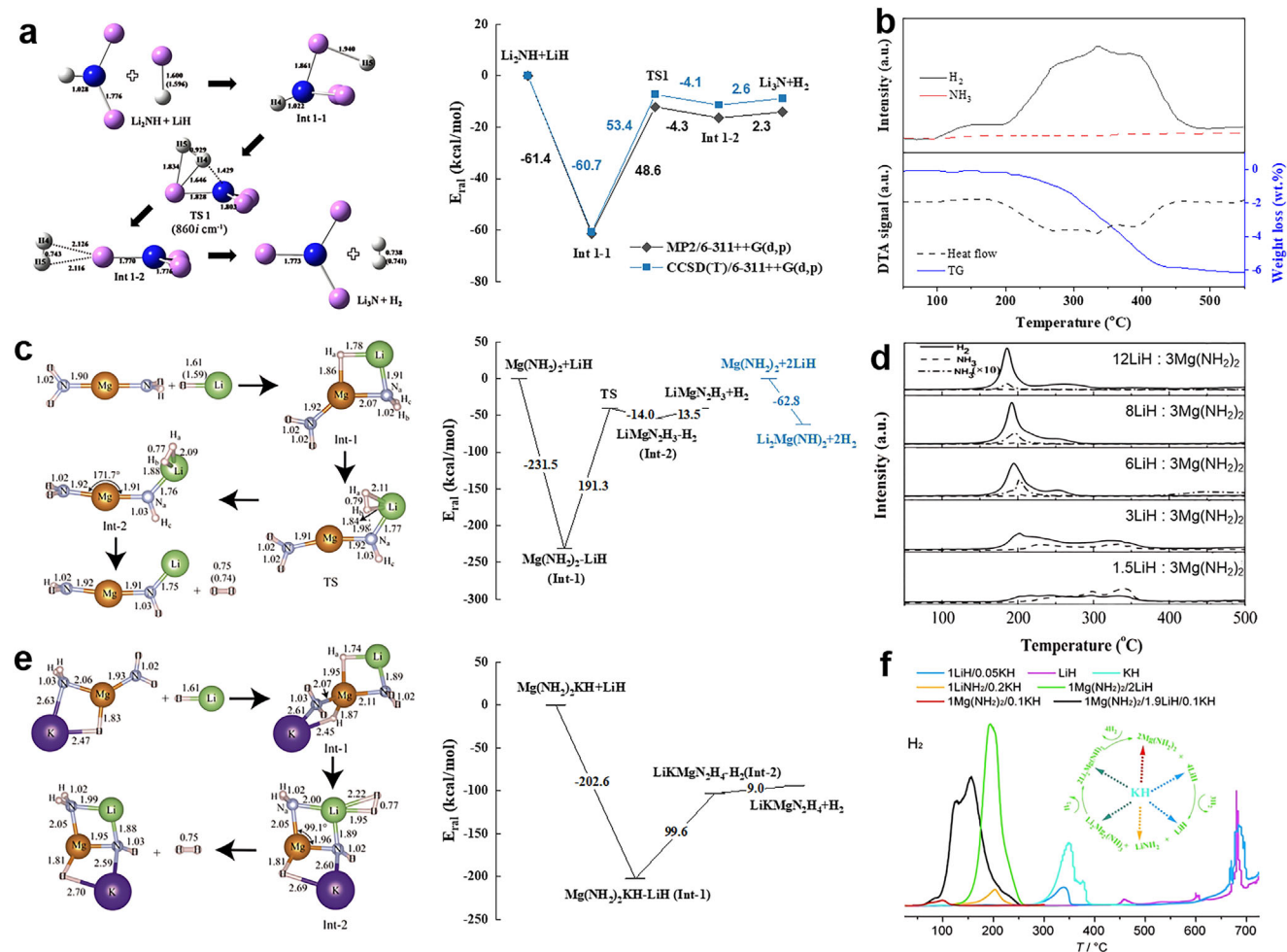


**Figure 8.** a) Optimized structures and corresponding energy diagram of the  $\text{Li}_2\text{NH} + \text{LiH} \rightarrow \text{Li}_3\text{N} + \text{H}_2$  reaction. Reproduced with permission.<sup>[91b]</sup> Copyright 2010, Elsevier. b) Thermal desorption profile and corresponding mass spectrum (TDMS) of the  $\text{LiNH}_2 + 1.2\text{LiH}$  mixture. Reproduced with permission.<sup>[230]</sup> Copyright 2011, Elsevier. c) Optimized structures of the reactants, the intermediate complexes (Int-1, 2), the transition state (TS), and the products of  $\text{Mg}(\text{NH}_2)_2 - \text{LiH}$  and e)  $\text{Mg}(\text{NH}_2)_2 - \text{LiH} - \text{KH}$  composite of releasing a hydrogen molecule and corresponding energy diagram. Reproduced with permission.<sup>[94]</sup> Copyright 2016, Elsevier. d) TDMS profiles of the  $\text{Mg}(\text{NH}_2)_2 - \text{LiH}$  composite with varying ratios. Reproduced with permission.<sup>[93b]</sup> Copyright 2006, American Chemical Society. f) Chemical interactions between KH and the reactants/intermediates of the  $\text{Mg}(\text{NH}_2)_2/2\text{LiH}$  system qualitatively evaluated by using TDMS. Reproduced with permission.<sup>[95]</sup> Copyright 2013, Wiley-VCH.

desorption is needed for fine-tuning the kinetics and thermodynamics of systems at the microscopic scale.

#### 2.2.4. Summary and Outlook

Various effective strategies have been developed for the thermodynamic regulation of Li/Mg-based hydrogen storage materials, including alloying, cation/anion substitution, and the construction of destabilized composite systems. These strategies aim to influence the thermodynamic stability of reactants/products by adjusting the composition, thereby optimizing reaction pathways and reducing enthalpy change of reaction to facilitate hydrogen absorption and desorption processes.

However, the incorporation of destabilizing components introduces greater complexity to the reaction mechanisms and frequently leads to unfavorable side reactions, resulting in cycling

capacity losses. Thus, a main challenge for future research lies in enhancing the kinetic dominance of the primary reaction pathway while suppressing the side reactions. Regarding catalyst design, valuable insights could be drawn from the more established research fields of ammonia synthesis/decomposition and organoboron chemistry to explore the application potential of novel metallic and non-metallic catalysts for boron and nitrogen fixation while maintaining their chemical reactivity. Considering the significant influence of component homogeneity on reaction pathways, advanced synthesis techniques (such as ultrasonic, photochemical, and microwave methods) could be further developed to construct uniformly distributed nanoscale multiphase composite systems that effectively suppress side reactions.

Additionally, advanced characterization techniques are needed to elucidate the mechanisms of thermodynamic destabilization at the atomic level, such as localized structures, and help establish structure–property relationships between destabilizing units and

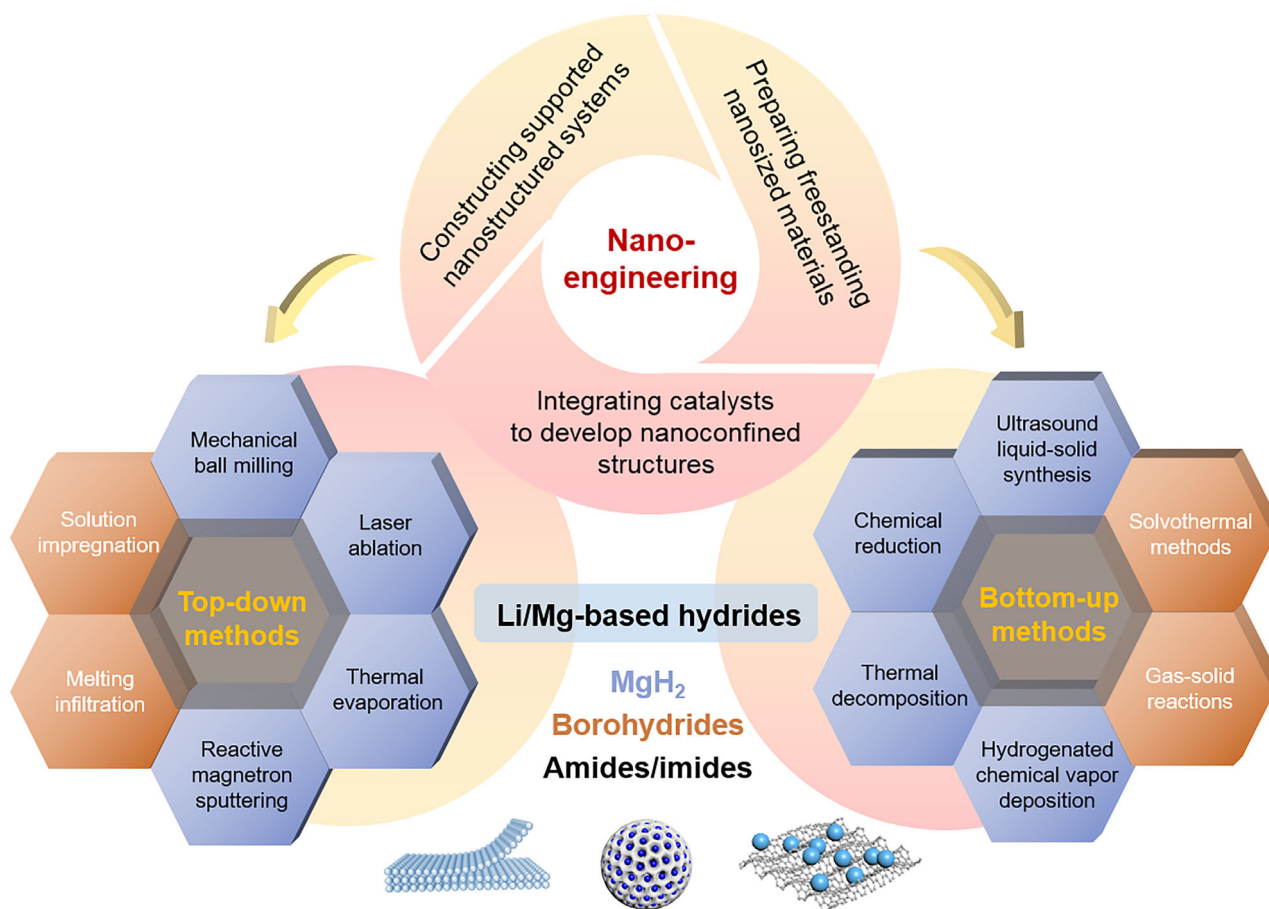


**Figure 9.** Summary of preparation strategies and synthesis methods for Li/Mg-Based hydrides nanoengineering.

thermodynamic properties. Given that the thermodynamic properties of materials are often influenced by intrinsic material characteristics, theoretical calculations, and AI technologies will serve as more efficient tools in guiding the design and development of novel destabilized composite systems.

### 2.3. Nanosizing and Nanostructuring

Light metal hydrides generally require elevated temperatures for hydrogen release and high pressures for hydrogen absorption, primarily due to their inherent thermodynamic stability and kinetic barriers, which limit their practical applications. Nanosizing has emerged as an effective strategy to enhance both the thermodynamic and kinetic properties of hydrogen storage materials.<sup>[13b,c,100]</sup> Three approaches—nanosizing, nanoconfinement, and nanostructuring—can all produce nanoscale particles, but they differ in their underlying principles and objectives. Nanosizing refers to reducing particle size to the nanometer scale. Nanoconfinement involves embedding materials within confined nanoscale spaces such as pores or hollow structures. Nanostructuring broadly refers to the intentional design of nanoscale architectures, including core-shell, layered, or hierarchical structures. At the nanoscale, the introduction of additional surface energy increases reactivity and destabilizes the materi-

als, thereby reducing their thermodynamic stability.<sup>[101]</sup> Additionally, nanosizing reduces particle size, shortens hydrogen diffusion pathways, and accelerates reaction kinetics, effectively lowering the energy barriers involved in multistep reactions.<sup>[102]</sup>

Recent research has been focused on developing various Li/Mg-based hydrogen storage systems, including  $MgH_2$ , borohydrides, and amides/imides, to improve the reversible hydrogen storage performance and practical viability of nanostructured materials. For each material type, research can be divided into three main design strategies: preparing freestanding nanosized materials, constructing supported nanostructured systems, and integrating catalysts to develop nanoconfined structures (**Figure 9**). This section provides an overview of the synthesis methods, hydrogen storage properties, and reaction mechanisms of nanosized and nanostructured hydrogen storage materials. The design and performance of nanoconfined hydrogen storage systems integrated with catalysts and destabilization have been partially discussed in Sections 2.1 and 2.2.

#### 2.3.1. Magnesium Hydride

The synthesis of nanosized  $MgH_2$  can be classified into two main approaches: top-down and bottom-up. Top-down techniques, such as mechanical ball milling and physical vapor deposition

(PVD), begin with bulk materials and break them down into nanoscale structures. On the other hand, bottom-up methods, including chemical vapor deposition (CVD) and solution-based chemical techniques like thermal decomposition, solution impregnation, electrochemical deposition, and nanoconfinement, involve assembling nanosized  $\text{MgH}_2$  from atomic or molecular precursors.

Mechanical ball milling is among the most widely used top-down strategies for synthesizing nanosized  $\text{MgH}_2$  and Mg, primarily due to its ability to simultaneously achieve material nanosizing and catalyst doping. During the milling process, mechanical energy disrupts the crystal lattice, breaking larger particles into smaller fragments. The resulting  $\text{MgH}_2$  particles have an increased specific surface area, which shortens hydrogen diffusion pathways, thereby enhancing hydrogen absorption and desorption rates. In 1999, Zaluska et al. first demonstrated improved hydrogen storage performance of  $\text{MgH}_2$  through ball milling.<sup>[103]</sup> Schulz et al. further showed that ball milling can reduce the dehydrogenation activation energy of  $\text{MgH}_2$  from 156 to 120 kJ mol<sup>-1</sup>, significantly boosting the dehydrogenation rate at 300 °C.<sup>[104]</sup> Moreover, the collision forces during ball milling can reach extremely high pressures, effectively refining particles and inducing chemical reactions that produce ultrafine nanoparticles.<sup>[105]</sup> For instance, Paskevicius et al. successfully synthesized  $\text{MgH}_2$  nanoparticles smaller than 7 nm by milling a mixture of LiH and  $\text{MgCl}_2$ .<sup>[106]</sup> However, despite the simplicity and efficiency of ball milling, achieving particle sizes below 100 nm remains challenging, as cold welding would cause particles to re-agglomerate.<sup>[107]</sup> Solvent-assisted ball milling can effectively alleviate agglomeration caused by cold welding during the milling process. The choice of organic solvent plays a crucial role, with commonly used options including tetrahydrofuran (THF), diethyl ether, cyclohexane, and acetone. Zou et al. demonstrated that the addition of 20 wt% acetone significantly reduced the particle size of Mg to below 100 nm, thereby enhancing the kinetic performance of the resulting Mg nanoparticles.<sup>[108]</sup> This improvement is attributed to the chemisorption of acetone onto defects or surfaces of Mg during milling, leading to the formation of a metastable magnesium complex. In contrast, solvents such as methanol, which contain highly reactive functional groups, tend to passivate the Mg surface and adversely affect its performance.

PVD is another top-down approach that uses high-energy beams, such as electron beams or lasers, to bombard or heat a target material, causing it to sublime or evaporate and subsequently deposit onto a substrate to form nanostructures. By controlling parameters like pressure and temperature during deposition, particle growth rate can be finely tuned, allowing precise control over size and morphology, making PVD particularly suitable for fabricating 1D and 2D nanostructures. In 2007, Li et al. used the vapor-transport method to synthesize Mg nanowires of different diameters, with the 30–50 nm nanowires absorbing 7.6 wt%  $\text{H}_2$  at 300 °C and releasing 3.28 wt%  $\text{H}_2$  within 30 min at 200 °C.<sup>[109]</sup> Leon et al. utilized thermal evaporation to fabricate 30  $\mu\text{m}$ -thick Mg films, which displayed remarkable hydrogenation and dehydrogenation properties along the [002] crystallographic direction.<sup>[110]</sup> Shimizu et al. employed reactive magnetron sputtering to achieve epitaxial growth of  $\text{MgH}_2$  films on MgO (100) substrates, highlighting the substantial influence

of substrate temperature and orientation on the resulting film performance.<sup>[111]</sup> Thermal evaporation allows for precise control over film thickness and dimensions, thus making it ideal for depositing multilayer metal coatings (e.g., Pd, Ti, Ni etc.) onto Mg films.<sup>[112]</sup> Higuchi et al. utilized radio frequency sputtering to deposit a 25 nm-thick Pd coating on a 200 nm-thick Mg film.<sup>[113]</sup> This composite absorbed 2.9–6.6 wt%  $\text{H}_2$  at 100 °C and desorbed at temperatures  $\sim$ 190 °C. The Pd coating not only protects Mg from oxidation but also acts as a catalyst for hydrogen absorption and desorption.<sup>[114]</sup> Zhu et al. developed a series of Mg-rare earth films (e.g., Mg–Mm–Ni) that demonstrated comparable hydrogen storage capabilities at low temperatures.<sup>[115]</sup> Mg/polymer composite films exhibited good air stability, though their hydrogen storage capacity was somewhat reduced.<sup>[116]</sup> Makridis et al. employed laser ablation method to generate Mg nanoparticles with diameters below 7 nm, subsequently stabilizing them in a polymer poly(methyl methacrylate) (PMMA) matrix. These nanoparticles absorbed 5.5 wt%  $\text{H}_2$  within 20 min at 250 °C under 2.5 MPa  $\text{H}_2$  pressure.<sup>[117]</sup>

Unlike PVD, hydrogenated chemical vapor deposition (HCVD) is a bottom-up synthesis technique that generates nanomaterials via vapor-phase chemical reactions. This approach enables the direct synthesis of high-purity nanosized  $\text{MgH}_2$  using high-pressure hydrogen gas and magnesium vapor, effectively removing the activation treatment and rate-limiting steps commonly associated with solid–gas reactions.<sup>[118]</sup> Zhu et al. used HCVD to synthesize  $\text{MgH}_2$  nanofibers and found that increasing hydrogen pressure improved the product's specific surface area and yield, while also exploring the effects of hydrogen pressure on product formation rate, composition, and morphology.<sup>[119]</sup> Additionally, waste magnesium can be utilized as a raw material to produce low-cost, high-purity  $\text{MgH}_2$ .<sup>[120]</sup>

Solution-based chemical technique is also a bottom-up synthesis strategy often employed to produce nanoparticles via chemical reduction or thermal decomposition in a liquid medium. By precisely controlling reaction condition—such as precursor concentration, reaction temperature, and type of reducing agents and solvents—nanoparticle morphology can be effectively tailored. To synthesize nanoscale magnesium-based materials, chemical reduction of magnesium precursors typically involves reducing agents in organic solutions (e.g., alkali or alkaline earth metals like Li, Na, K, Ca) along with electron carriers, such as naphthalene or phenanthrene. For example, Norberg et al. successfully synthesized Mg nanocrystals ranging from 25 to 38 nm using potassium and aromatic compounds, where the 25 nm particles exhibited a  $\text{H}_2$  absorption rate seven times faster than the 38 nm particles.<sup>[121]</sup> Liu et al. prepared 8 nm Mg nanoparticles through the reduction reaction of dibutylmagnesium ( $\text{MgBu}_2$ ) with lithium, which showed significant thermodynamic enhancement by absorbing  $\text{H}_2$  below 150 °C.<sup>[122]</sup> Thermal decomposition involves decomposing Grignard reagents (organomagnesium compounds) to produce nanoscale  $\text{MgH}_2$ , where adjusting reaction conditions (i.e., temperature and pressure) affects the growth kinetics, thereby controlling particle morphology and size. For instance, Setijadi et al. synthesized  $\text{MgH}_2$  nanoparticles of  $\sim$ 30 nm via thermal decomposition of  $\text{MgBu}_2$ , which released  $\text{H}_2$  at 250 °C without requiring a catalyst.<sup>[123]</sup> The choice of solvent can also affect particle surface energies and morphologies,

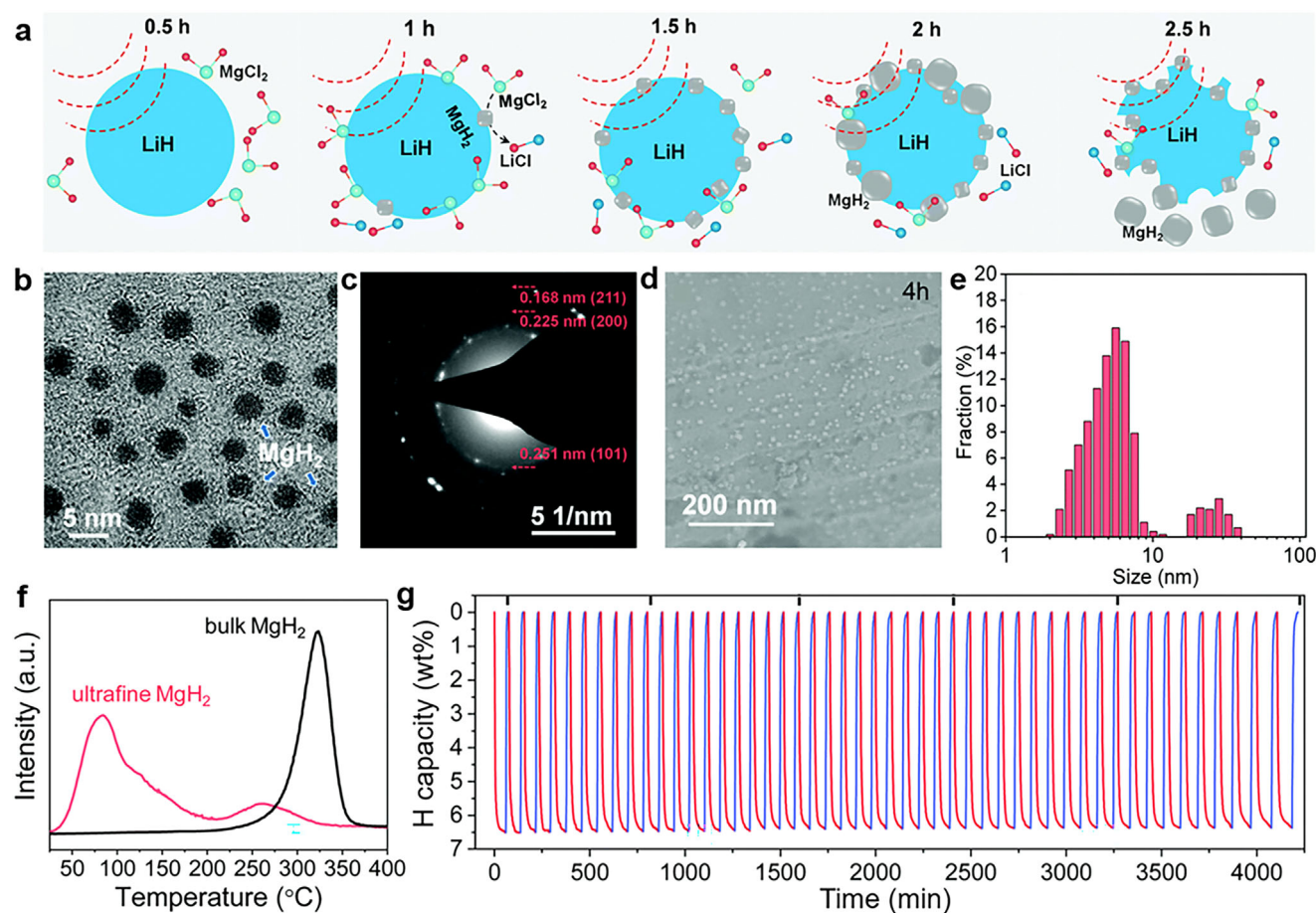


**Figure 10.** a) Schematic preparation illustration of the liquid–solid metathesis reaction for non-confined ultrafine  $\text{MgH}_2$ . b) SAED pattern, c) HRTEM image, d) SEM, and e) particle size distribution of non-confined ultrafine  $\text{MgH}_2$ . f) TPD-MS of bulk and non-confined ultrafine  $\text{MgH}_2$ . g) Cycling stability of non-confined ultrafine  $\text{MgH}_2$ . Reproduced with permission.<sup>[129]</sup> Copyright 2021, Royal Society of Chemistry.

as certain solvents can promote the growth of specific crystal facets.<sup>[124]</sup> Besides  $\text{MgBu}_2$ , common Grignard reagents also include dipropylmagnesium, di-isopropylmagnesium, di-*n*-butylmagnesium, di-*tert*-butylmagnesium, and dihexylmagnesium.

Additionally, solution-based chemical techniques are also widely used for synthesizing supported nanoconfined Mg-based hydrogen storage materials. By impregnating porous support materials with precursor solutions, in situ growth of nanoscale  $\text{MgH}_2$  particles can be achieved, maintaining high dispersion on the support and simultaneously improving kinetic and thermodynamic properties during  $\text{H}_2$  absorption and release.<sup>[125]</sup> This method also allows for the combination of nanoconfinement and catalytic strategies, leading to synergistic effects. Various porous materials, such as ordered mesoporous silica, metal–organic frameworks, and porous carbon materials, have been widely used to confine  $\text{MgH}_2$  nanoparticles within their pores.<sup>[126]</sup> One significant advantage of this approach is improving the air stability of nanosized  $\text{MgH}_2$ . Confining them within nanoporous carbon or encapsulating them in a PMMA matrix has been reported to effectively prevent oxidation.<sup>[127]</sup> A typical study combining nanoconfinement and catalysis is presented by Xia et al., who

synthesized  $\text{MgH}_2$  nanoparticles with an average size of 5.7 nm on a Ni–graphene support via thermal decomposition of  $\text{MgBu}_2$ , achieving 99.2% storage capacity retention after 100 cycles at 200 °C.<sup>[128]</sup> Similarly, Zhu et al. grew  $\text{MgH}_2$  nanoparticles on 3D  $\text{Ti}_3\text{C}_2$  nanosheets and utilized in situ generated  $\text{TiH}_2$  as a catalyst phase to significantly enhance the kinetics of  $\text{H}_2$  absorption and desorption, maintaining a reversible capacity of 4 wt%  $\text{H}_2$  after 60 cycles at 200 °C.<sup>[26]</sup>

Notably, in 2021, Zhang et al. developed an ultrasound-driven liquid–solid phase synthesis method to successfully produce free-standing ultrafine  $\text{MgH}_2$  nanoparticles with sizes ranging from 4 to 5 nm (Figure 10b–e).<sup>[129]</sup> Using THF as the reaction medium, soluble  $\text{MgCl}_2$  reacted with insoluble LiH under ultrasonic conditions to form  $\text{MgH}_2$  and LiCl. LiCl dissolved in THF, while  $\text{MgH}_2$ , which has a higher density than THF, was separated easily by centrifugation. The liquid vibrations generated by ultrasound enhanced the collision between reactants and simultaneously inhibited excessive crystal growth, which was the key points to obtain ultrafine  $\text{MgH}_2$  nanoparticles (Figure 10a). This system achieved a reversible hydrogen storage capacity of 6.7 wt%  $\text{H}_2$  at room temperature for the first time, and showed excellent cycling stability (Figure 10f,g). Despite the relatively slow kinetics,

this study highlighted the potential of ultrasound synthesis technology in nanoparticle preparation, pointing to a new direction for the development of ultrafine nanosizing  $\text{MgH}_2$ -based materials.

### 2.3.2. Borohydrides

Nanoborohydrides can be prepared using either top-down or bottom-up approaches. Top-down methods mainly consist of solid-phase techniques like ball milling and liquid-phase methods, including melting infiltration and solution impregnation. The latter two liquid-phase techniques are commonly used to create nanoconfined composite systems with a support matrix. Bottom-up approaches involve techniques like gas–solid reactions and solvothermal methods. Similar to the  $\text{MgH}_2$  system, the solid-phase method is the simplest way to introduce catalysts and produce borohydrides at the nanoscale (hundreds of nanometers), and thus, will not be discussed in detail here.

The melting infiltration method involves heating borohydrides under hydrogen pressure until they reach a molten state, utilizing the fluidity and dispersibility of the molten phase to achieve nanostructuring upon cooling. This technique is commonly applied to  $\text{LiBH}_4$ , which melts at 300 °C under 10 MPa of hydrogen pressure. In contrast,  $\text{Mg}(\text{BH}_4)_2$  requires an extreme high pressure of 100 MPa to prevent its decomposition during the melting process, making this approach rarely employed for its preparation.<sup>[130]</sup> Liu et al. used the melting infiltration method to confine  $\text{LiBH}_4$  within nanopores of varying sizes, finding that smaller pore sizes lowered both its hydrogen release temperature and the emission of toxic  $\text{B}_2\text{H}_6$ .<sup>[131]</sup> Guo et al. confined  $\text{LiBH}_4$  (~30 nm) within carbon nanocages, lowering its dehydrogenation peak temperature to 320 °C.<sup>[132]</sup> Similarly, Plerdsranoy et al. confined  $\text{LiBH}_4$  (~20 nm) within activated carbon nanofibers, achieving a reduced dehydrogenation peak temperature of 305 °C.<sup>[133]</sup> Wu et al. synthesized carbon hollow spheres and loaded them with 70–90%  $\text{LiBH}_4$  using the melting infiltration method.<sup>[134]</sup> As the infiltration time increased, the hollow spheres deformed into double-layered carbon nanobowls, with the  $\text{LiBH}_4$  particle size aligning with the diameter of the carbon spheres (~100 nm). This indicates that the high-pressure conditions during the melting process may impact the final morphology of template materials with limited structural stability.

Likewise, the solution impregnation method involves dissolving borohydrides in an organic solvent to form a precursor solution, which is then infused into the porous template material. Upon solvent removal, dispersed nanoborohydrides are formed. This method is well-suited for the preparation of supported nanoconfined composite systems of both  $\text{LiBH}_4$  and  $\text{Mg}(\text{BH}_4)_2$ , with THF being the most commonly utilized solvent. During the preparation process, ultrasonic treatment is typically employed to enhance the dispersion of the solution within the support material. As a result, the particle size obtained via the solution impregnation method can be smaller than that achieved with the melting method, often falling below 10 nm, whereas the latter typically produces particles in the range of several tens of nanometers. Fang et al. applied the solution impregnation method to embed  $\text{LiBH}_4$  into activated carbon frameworks with 3.2 nm pores, producing  $\text{LiBH}_4$  particles under 5 nm in size. These nanostruc-

tured  $\text{LiBH}_4$  particles exhibited a dehydrogenation temperature of 220 °C, 150 °C lower than that of bulk  $\text{LiBH}_4$ , with a ten-fold increase in the dehydrogenation rate.<sup>[135]</sup> Fichtner and his co-authors incorporated  $\text{Mg}(\text{BH}_4)_2$  into pretreated activated carbon with pores smaller than 2 nm, reducing its onset dehydrogenation temperature to 170 °C and lowering its onset dehydrogenation temperature to 170 °C and achieving a  $\text{H}_2$  release of 6 wt% in a composite containing 44%  $\text{Mg}(\text{BH}_4)_2$ .<sup>[136]</sup> Lai et al. compared the effects of melting infiltration and solution impregnation on hydrogen storage performance of borohydrides.<sup>[137]</sup> The experiments revealed that borohydrides confined within hollow carbon exhibited lower dehydrogenation temperatures when prepared via solution impregnation, likely attributed to the better wetting on the matrix, which in turn influences the dispersion of nanoborohydrides. These findings underscore the importance of considering the interaction between the support and solvent surfaces when selecting a top-down approach for synthesizing nanoborohydrides, as efficient infiltration enhances dispersion and optimizes system performance. Aligned with the advantages of nano- $\text{MgH}_2$  prepared by solution impregnation, the solution impregnation of borohydrides is often coupled with catalytic strategies, generating synergistic effects between nanoconfinement and catalysis to further enhance the thermodynamic and kinetic properties of borohydrides.<sup>[138]</sup>

The bottom-up synthesis strategy relies on in situ chemical reactions, with borohydrides produced primarily through gas–solid reactions and solvothermal methods. For example, Xia et al. employed an in situ gas–solid reaction between  $\text{C}_4\text{H}_9\text{Li}$  and  $\text{B}_2\text{H}_6$  under hydrogen pressure to fabricate 4 nm-thick  $\text{LiBH}_4$  nanolayers on graphene surfaces, which achieved a rapid  $\text{H}_2$  release of 9.7 wt% at 340 °C and maintained a reversible capacity of 7.5 wt%  $\text{H}_2$  after five cycles at 320 °C.<sup>[139]</sup> Zhang et al. synthesized  $\text{Mg}(\text{BH}_4)_2$  nanoparticles with an average size of 8 nm on graphene surfaces through an in situ gas–solid reaction between nano- $\text{MgH}_2$  and  $\text{B}_2\text{H}_6$ . The onset dehydrogenation temperature of  $\text{Mg}(\text{BH}_4)_2$ @Gr was reduced to 154 °C, with complete hydrogen release achieved at 225 °C.<sup>[140]</sup> Building on this, Wang et al. further employed this reaction to construct size-controlled  $\text{Mg}(\text{BH}_4)_2$ @ $\text{MgH}_2$  heterostructures, effectively reducing the kinetic barriers for the reversible hydrogen storage of  $\text{Mg}(\text{BH}_4)_2$  and  $\text{MgH}_2$  (Figure 11a–d).<sup>[141]</sup> In this system,  $\text{MgH}_2$  acts as a “hydrogen pump,” converting stable B–B bonds from endothermic to exothermic, thereby altering the enthalpy of B–H bond formation and significantly enhancing the reversibility of  $\text{Mg}(\text{BH}_4)_2$  (Figure 11e,f). As for the solvothermal synthesis strategy, Zhang et al. utilized a hydrogen-assisted solvothermal method with  $\text{C}_4\text{H}_9\text{Li}$  and  $\text{C}_6\text{H}_{15}\text{NBH}_3$  under 5 MPa hydrogen pressure and temperatures ranging from 40–100 °C. This approach yielded [100]-oriented  $\text{LiBH}_4$  nanorods with diameters of 500–800 nm, reducing the onset hydrogenation temperature to 180 °C.<sup>[142]</sup> Introducing few-layer graphene as a support provided additional nucleation sites, facilitating the transformation of  $\text{LiBH}_4$  from nanorods to nanoparticles with diameters of 20–50 nm.<sup>[143]</sup> Using a one-pot solvothermal approach, Zhang et al. introduced a Ni precursor to produce 5–10 nm  $\text{LiBH}_4$  nanoparticles grown on graphene, decorated with 2–4 nm Ni nanocrystals. This  $\text{LiBH}_4$  nanocomposite achieved reversible hydrogen storage with a capacity of ~9.2 wt%  $\text{H}_2$  at 300 °C, exhibiting stable performance over 100 cycles.<sup>[144]</sup>

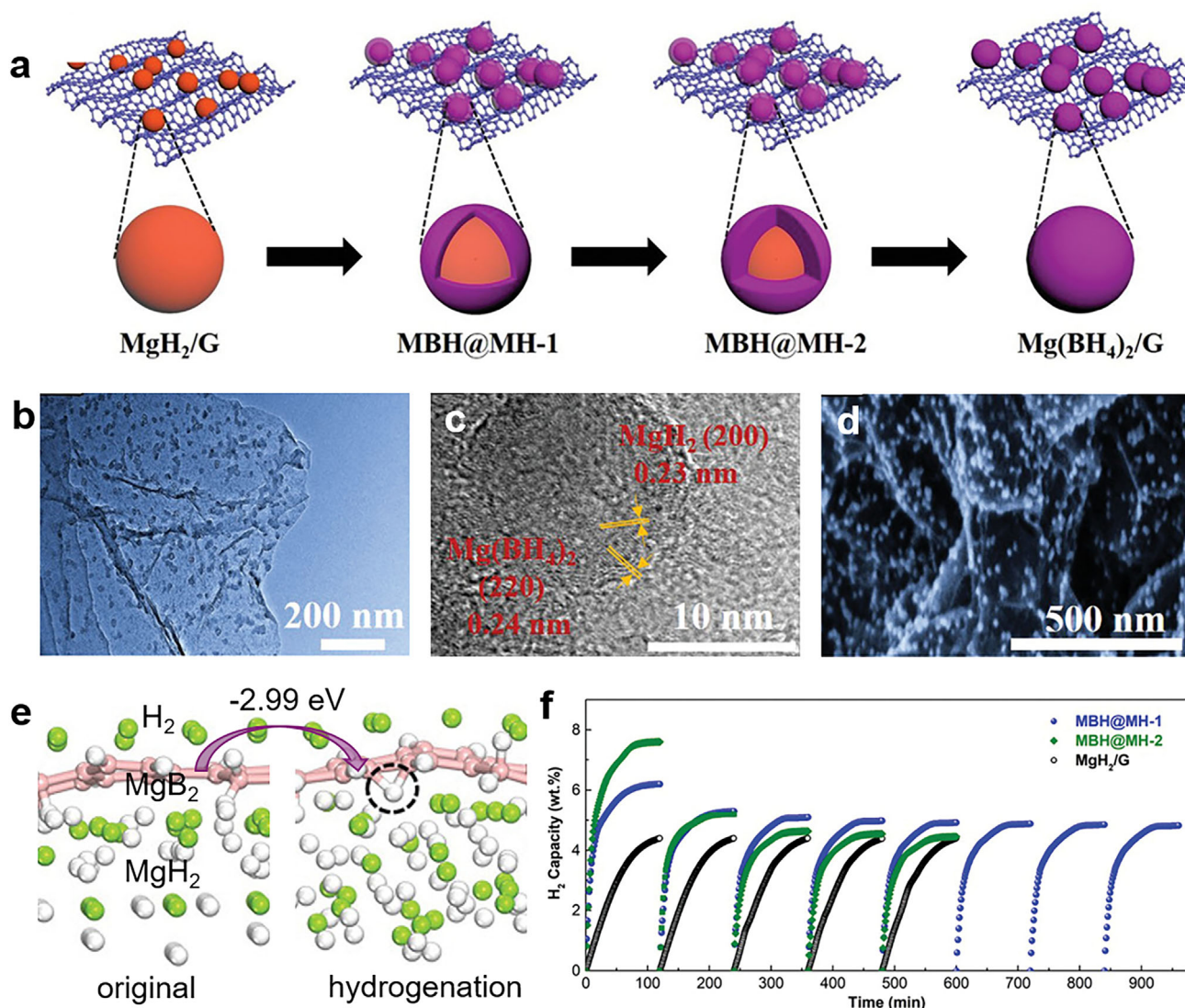


**Figure 11.** a) Schematic illustration of the synthesis of  $\text{Mg}(\text{BH}_4)_2@ \text{MgH}_2$  NPs on graphene. b) TEM, c) HRTEM, and d) SEM images of  $\text{Mg}(\text{BH}_4)_2/\text{G}$ . e) Calculated hydrogen absorption energy on  $\text{MgB}_2$  with the presence of  $\text{MgH}_2$  as the structural support. The Mg, B, and H atoms are shown in green, pink, and white spheres, respectively. f) Cycling performance of  $\text{Mg}(\text{BH}_4)_2@ \text{MgH}_2$  composites, with  $\text{MgH}_2/\text{G}$  included for comparison. Reproduced with permission.<sup>[141]</sup> Copyright 2020, Wiley-VCH.

In terms of the preparation of free-standing nanostructured borohydrides, Pang et al. used  $[\text{LiBH}_4(\text{MTBE})]_n$  as a precursor and successfully synthesized  $\text{LiBH}_4$  nanorods with the width of 10–40 nm via a mechanical-force-driven physical vapor deposition procedure.<sup>[145]</sup> Similarly, Wang et al. stabilized  $\text{LiBH}_4$  nanoparticles using surfactants through a solvent evaporation method. They reported that the growth and stability of the  $\text{LiBH}_4$  nanoparticles are influenced by the chain length, steric hindrance, and binding strength of surfactant.<sup>[146]</sup> Zhang et al. synthesized hierarchical nanostructured  $\text{LiBH}_4$ , composed of 50–60 nm primary nanoparticles, via a one-pot solvothermal method. The reduced particle size and porous aggregated structure promoted dehydrogenation prior to melting, effectively suppressing foaming and enabling 12 wt% reversible  $\text{H}_2$  storage at 400 °C.<sup>[147]</sup>

### 2.3.3. Amides and Imides

In the nanofabrication of amine/imine-based materials, in addition to high-energy ball milling, several distinctive methods have been reported, including metal reduction, wet impregnation, and electrospinning. These techniques are typically combined with thermal reduction processes to synthesize nanoscale amine/imine-based materials. For example, Yang et al. employed hydrogen plasma bombardment on metallic Li to produce 200–400 nm Li nanoparticles, followed by  $\text{NH}_3$  plasma treatment to obtain  $\text{Li}_2\text{NH}$  nanoparticles.<sup>[148]</sup> After combined with  $\text{Mg}(\text{BH}_4)_2$  to form a ternary system, a hydrogen desorption of 5.3 wt%  $\text{H}_2$  was achieved at 150 °C. Similarly, Wood et al. successfully synthesized  $\text{Li}_3\text{N}$  within porous carbon by reacting metallic lithium with  $\text{NH}_3$ .<sup>[149]</sup> The reaction process formed core-shell

$\text{Li}_3\text{N}/[\text{LiNH}_2 + 2\text{LiH}]$  nanostructures, which altered the hydrogenation and dehydrogenation pathways, suppressing the formation of harmful intermediates and significantly enhancing the kinetics and reversibility of the hydrogen storage reactions. Additionally, Xia et al. developed an electrospinning technique by incorporating  $\text{Li}_3\text{N}$  solution into spinning precursors containing polyvinylpyrrolidone.<sup>[150]</sup> After dehydration and high-temperature carbonization under  $\text{N}_2$  atmosphere, 3D porous carbon-coated  $\text{Li}_3\text{N}$  nanofibers are successfully produced, which demonstrated stable reversibility over ten cycles of  $\text{H}_2$  desorption/absorption at 250 °C. Furthermore, by incorporating  $\text{Mg}^{2+}$  salts to the spinning precursor and conducting in situ annealing with hydrogenation, they successfully obtained hierarchical porous  $\text{Li}_2\text{Mg}(\text{NH})_2@C$  nanowires with a lower dehydrogenation temperature, which exhibited outstanding cycling stability, retaining 94.6% of its capacity after 20 cycles at 130 °C.<sup>[151]</sup>

### 2.3.4. Summary and Outlook

In the synthesis of nanostructured Li/Mg-based hydrogen storage materials, various effective strategies have been developed, with significant performance enhancements achieved, particularly through the incorporation of supports or catalysts. However, the synthesis of free-standing ultrafine metal nanoparticles remains limited, posing a challenge for enhancing performance without sacrificing hydrogen storage capacity. Furthermore, the mechanisms driving thermodynamic improvements in nanomaterials remain a subject of debate, with experimental studies failing to establish consistent size-dependent trends necessary to support detailed mechanistic investigations.

Therefore, several key areas merit further exploration. First, a comprehensive investigation of the reaction mechanisms involved in nanostructuring is essential to elucidate how different synthesis methods influence material properties. Second, advancing the development of unsupported nanomaterials is vital to achieving higher reversible hydrogen storage capacities along with enhanced performance. Last, to meet the requirements of practical applications, efforts should be directed toward optimizing synthesis processes to ensure scalability and cost-efficiency for large-scale production of nanosized hydrogen storage materials.

## 2.4. External Field-Driven Techniques

Despite various modification strategies, the thermodynamic and kinetic properties of Li/Mg-based hydrides have improved to some extent, yet high temperatures remain essential for efficient hydrogen absorption and desorption. In practical applications, it relies on electric heating to supply sufficient external energy to drive hydrogen storage reactions. However, such complex heating systems reduce the energy density of hydrogen storage systems, and high operational costs remain a significant barrier to the large-scale deployment of hydrogen storage materials. To address this challenge, developing external field-driven methods distinct from non-conventional electric heating is particularly important.

Non-conventional electric heating external field-driven technologies reported to date encompass various forms, including

electromagnetic waves (e.g., light and microwaves), mechanical forces (e.g., fraction and ultrasonic techniques), as well as electrochemical methods, and electron beams technologies. Among these, electromagnetic wave-driven technologies, which utilize light or microwaves to promote the hydrogen absorption and desorption processes of hydrides, have advanced rapidly in recent years, becoming the most representative external field-driven method for driving hydrides. Since electromagnetic waves propagate without the need for a medium, this technology offers the distinct advantages of remote, non-contact heating, simplifying system design and improving operational flexibility.<sup>[152]</sup> On one hand, electromagnetic wave-driven techniques eliminate the complexities of traditional electric heating systems by employing focused wave sources for rapid, localized heating, thereby facilitating hydride reactions under milder conditions while simultaneously reducing external energy consumption and operational costs. On the other hand, investigating the interaction mechanisms between electromagnetic waves and hydrides can reveal unique modification pathways distinct from conventional thermal catalysis, offering valuable insights to develop more efficient field-driven hydrogen storage technologies.

Electromagnetic waves encompass microwaves, light (including infrared, visible, and ultraviolet), and radiations (such as X-rays and gamma rays), each characterized by distinct properties, frequency (wavelength) ranges, and energy levels.<sup>[153]</sup> This section reviews the latest advancements in electromagnetic wave-driven hydrogen storage technologies and provides a brief overview of the potential of other field-driven approaches.

### 2.4.1. Light-Driven Techniques

Harnessing solar energy for storage is widely recognized as a crucial strategy for mitigating global energy shortages and environmental pollution.<sup>[154]</sup> Light-driven hydrogen storage reactions, utilizing natural light across the ultraviolet–visible–near-infrared (UV–vis–NIR) spectrum, also hold great potential for advancing next-generation energy storage technologies.

In the 1980s, Dougherty et al. investigated the decomposition of hydrides, including  $\text{BaH}_2$ ,  $\text{CaH}_2$ ,  $\text{MgH}_2$ , etc., under UV light at room temperature.<sup>[155]</sup> Color changes were observed in these hydrides under UV light irradiation, accompanied by the release of small amounts of  $\text{H}_2$ . The dehydrogenation rate peaked rapidly at the onset of light exposure, followed by a gradual decline to a steady rate. They proposed that photodecomposition process involves multiple light-induced mechanisms, with the initial stage driven by interactions between photo-generated carriers (electrons and holes) and the solid hydrides, followed by the formation of a uniform reactant–product interface, demonstrating the interaction between hydrides and light. Recently, Chen et al. discovered that UV–vis irradiation can weaken, or even break, the highly stable Li–H chemical bonds in LiH, resulting in the release of  $\text{H}_2$  and the formation of hydrogen vacancies in hydrides (Figure 12b).<sup>[156]</sup> Through this unique photodecomposition pathway, LiH released over 0.0033 MPa of  $\text{H}_2$  at room temperature, which is ~16 orders of magnitude higher than the thermodynamic equilibrium hydrogen pressure of LiH at the same temperature (Figure 12c,d). More importantly, LiH demonstrated reversible hydrogenation under light irradiation, with the capacity

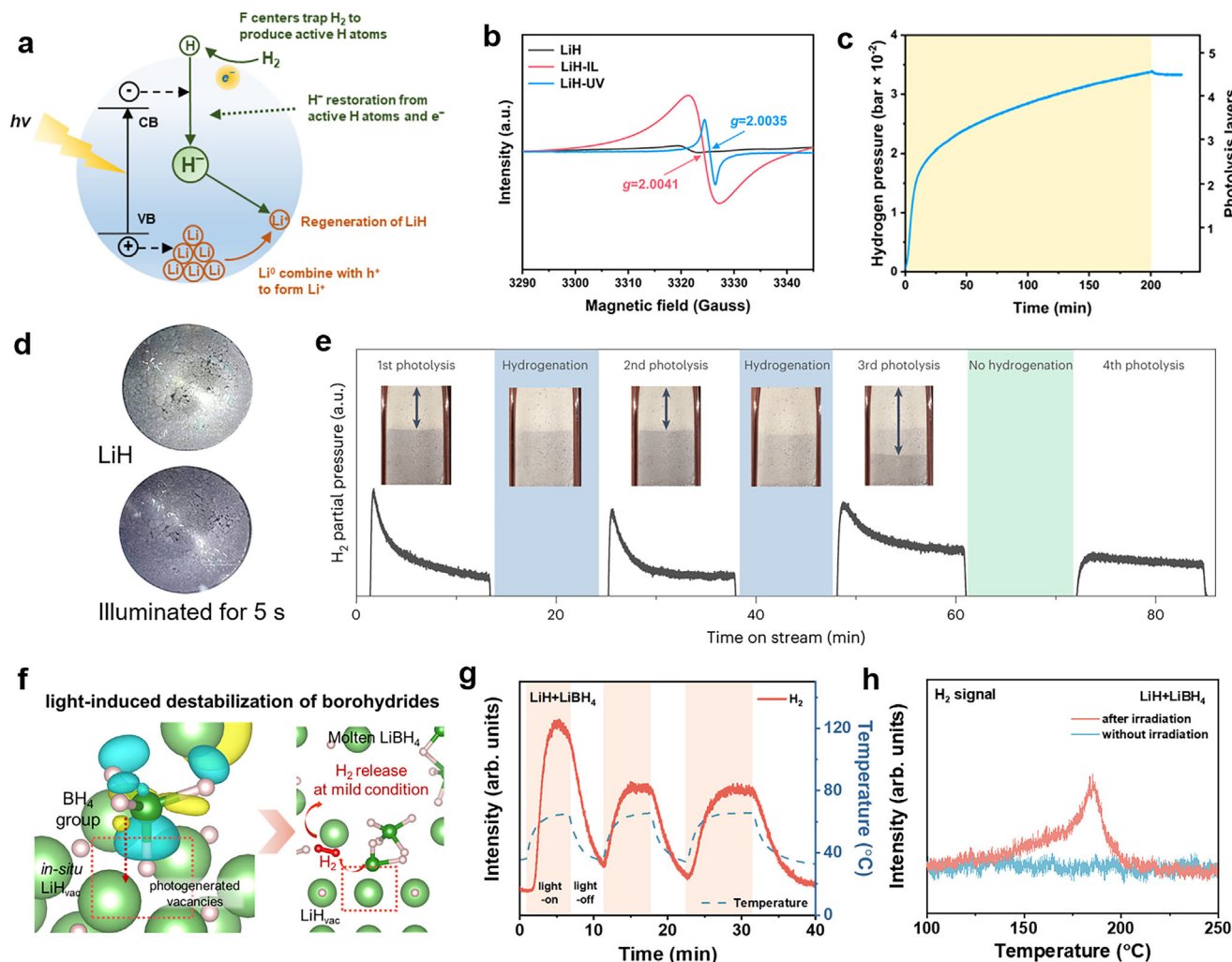


**Figure 12.** a) A proposed reaction mechanism for re-hydrogenation of LiH. b) EPR spectra of LiH before and after illumination. c) Volumetric dehydrogenation of LiH under UV-vis illumination. The yellow region represents the UV-vis illumination period from 0 to 200 min. The right axis represents the number of LiH lattice layers (assuming that H<sub>2</sub> has been fully released) corresponding to the amount of dehydrogenation. d) Digital photos of original LiH and illuminated LiH (LiH-IL hereafter). Reproduced with permission.<sup>[156]</sup> Copyright 2024, American Chemical Society. e) Cycles of the photon-assisted dehydrogenation and following dark hydrogenation of LiH. The inset photos show the color change of LiH during the experiment; the dark grey arrows represent the area covered with an opaque tape during illumination. Reproduced with permission.<sup>[158]</sup> Copyright 2024, Springer Nature. f) Schematic illustration of the destabilization mechanism of borohydrides induced by photogenerated vacancies in LiH. g) H<sub>2</sub> signal detected by mass spectrometry from a LiH and LiBH<sub>4</sub> mixture under light-on and light-off conditions. The sample temperature was continuously monitored in real time using a contact thermocouple. h) H<sub>2</sub> signal detected by mass spectrometry coupled with TGA for the illuminated LiH and LiBH<sub>4</sub> mixture during heating at a rate of 5 °C min<sup>-1</sup>. Reproduced with permission.<sup>[157]</sup> Copyright 2025, American Chemical Society.

to absorb 0.08 wt% of H<sub>2</sub> (Figure 12a,e). Very recently, Zhang et al. discovered that light-induced vacancies in LiH form electron-rich hydrogen vacancies, which spontaneously induce strong adsorption of [BH<sub>4</sub>]<sup>-</sup> groups on the LiH surface (Figure 12e).<sup>[157]</sup> This strong adsorption activates asymmetric electronic reconstruction of the [BH<sub>4</sub>]<sup>-</sup> group, significantly reducing the thermodynamic stability of the B-H bonds. As a result, the dehydrogenation temperature is lowered to 66 °C, which is ~300 °C lower than that of the conventional thermally driven process (Figure 12f,g). Interestingly, Chen et al. also leveraged the localized active electrons in the vacancies generated under light irradiation in hydrides to achieve nitrogen fixation and ammonia synthesis under mild conditions.<sup>[158]</sup> These findings highlight the

non-thermal effects of hydrides under light irradiation, facilitating bond breaking and formation through mechanisms distinct from conventional thermal processes. In particular, the excitation and migration of photogenerated electrons modify the reaction pathways, unveiling a new approach for light-driven hydrogen storage.

Although the non-thermal effects of light-driven hydrides hold promise for hydrogen storage, the amount of hydrogen released remains limited. This limitation is primarily attributed to the hydrides' insufficient light absorption and their inherently poor thermal conductivity, restricting the dehydrogenation reaction to the illuminated surface area. To improve the efficiency of light utilization, researchers have recently focused on photothermal

effects as a key strategy, leveraging the conversion of solar energy into heat to raise the temperature of hydrides, thereby enhancing both the extent and rate of hydrogen absorption and desorption processes. Sun et al. introduced Au metal nanoparticles with localized surface plasmon resonance (LSPR) effects into typical hydrogen storage systems, including  $\text{MgH}_2$ ,  $\text{LiH}$ , and  $\text{NaAlH}_4$ .<sup>[159]</sup> Through the LSPR effect, these nanoparticles efficiently converted light energy into heat. Notably, the Mg–Au composite exhibited significant hydrogen absorption and transformed into the  $\text{MgH}_2$  phase at an overall temperature of only 100 °C under full-spectrum xenon lamp irradiation, demonstrating the localized heating effect of the Au nanoparticles. Similar phenomena were observed during the dehydrogenation of  $\text{LiH}$  and  $\text{NaAlH}_4$ , showing hydrogen desorption at relatively low temperatures. However, the light-driven reactions were confined to areas within ~5 nm of the Au nanoparticles, limiting the overall hydrogen storage efficiency.

To improve the photothermal conversion efficiency of hydride systems, traditional modification strategies, such as catalyst doping and alloying, are essential to further lower the operating temperatures of hydrogen storage reactions. In this context, a research team from Fudan University has developed an advanced light-driven hydrogen storage technique that coupling photothermal and catalytic effects. In the  $\text{NaAlH}_4$  system, Sun et al. developed a  $\text{TiO}_2$ @C catalyst that combines the catalytic properties of  $\text{TiO}_2$  with the photothermal effects of carbon, which enabled complete  $\text{H}_2$  release within 7 min under 1  $\text{W cm}^{-2}$  with an 85% capacity retention rate after ten cycles.<sup>[160]</sup> Regarding  $\text{LiBH}_4$ , Feng et al. reported that  $\text{LiBH}_4$ – $\text{TiF}_3$ – $\text{TiO}_2$  composites can rapidly release ~2.84 wt% of  $\text{H}_2$  within 10 min and 3.12 wt% within 30 min under a light intensity of 0.76  $\text{W cm}^{-2}$ .<sup>[161]</sup> As for  $\text{MgH}_2$  system, Zhang et al. developed a  $\text{Cu@MXene}$  catalyst that couples the LSPR effect of Cu nanoparticles with the photothermal effect of MXene, generating localized high temperatures under illumination to drive the hydrogen absorption and desorption reactions of  $\text{MgH}_2$  (Figure 13a–c).<sup>[162]</sup> Additionally, the in situ formation of Ti and  $\text{TiH}_x$  on the MXene surface during ball milling acts as a “hydrogen pump,” weakening the Mg–H bonds and significantly lowering the activation energy for hydrogen desorption. The  $\text{Cu@MXene-MgH}_2$  system maintained a reversible hydrogen storage capacity of 5.9 wt%  $\text{H}_2$  after 30 cycles under a light intensity of 4  $\text{W cm}^{-2}$ . Hu et al. further constructed a coupled interface by doping  $\text{MgH}_2$  with  $\text{TiN@TiO}_2$ , integrating the photothermal effect of  $\text{TiN}$  with the catalytic activity of  $\text{TiH}_2$  (Figure 13d–f).<sup>[163]</sup> Under a light intensity of 2.7  $\text{W cm}^{-2}$ , the  $\text{TiN@TiO}_2$ – $\text{MgH}_2$  system reached 240 °C, achieved complete dehydrogenation within 10 min, and retained 6.05 wt%  $\text{H}_2$  after 15 cycles, effectively reducing the light intensity required for the light-driven reversible hydrogen storage.

Additionally, Zhang et al. proposed a strategy to endow magnesium-based alloys with broad-spectrum light absorption (250–2000 nm) through in situ atomic reconstruction (Figure 13g–i).<sup>[21b]</sup> This approach utilizes a single-phase photothermal catalyst,  $\text{Mg}_2\text{Ni}(\text{Cu})$ , formed via the in situ dehydrogenation of  $\text{CuNi}$  and  $\text{MgH}_2$ . The alloying reconstruction of  $\text{Mg}_2\text{Ni}(\text{Cu})$  and its hydride exhibited “flat-band” orbitals near the Fermi level, facilitating intra-/inter-band electron transitions and enabling the system to achieve a broad-spectrum light absorption rate exceeding 85%. Under a light intensity of 2.6  $\text{W cm}^{-2}$ , the

photothermal temperature of the system reached 62 °C, marking a 6.1% increase compared to the material prior to alloy reconstruction. The Cu solute not only enhances the “hydrogen pump” effect of  $\text{Mg}_2\text{Ni}(\text{Cu})$  but also generates hot electrons via the LSPR effect of Cu, which are transferred to Ni, further weakening the Mg–H bonds. This study offers valuable insights for developing magnesium-based hydrogen storage materials with inherent photothermal conversion capabilities.

#### 2.4.2. Microwave-Driven Techniques

The frequency range of microwaves is lower than that of light (UV–vis–NIR), resulting in reduced energy per photon. Nevertheless, microwaves exhibit significantly higher heating efficiency compared to conventional electric heating, with heating rates reaching up to 70 °C  $\text{s}^{-1}$ , enabling rapid material heating.<sup>[164]</sup> Similar to light-driven strategies, microwave-driven research primarily focuses on enhancing microwave-to-heat conversion efficiency and exploring non-thermal effects induced by microwaves. In 2006, Nakamori et al. conducted a systematic study on the behavior of various metal hydrides ( $\text{MgH}_2$ ,  $\text{TiH}_2$ , and  $\text{LiBH}_4$ ) and alkaline earth metal hydrides ( $\text{NaBH}_4$  and  $\text{KBH}_4$ ) under single-mode microwave irradiation.<sup>[165]</sup> Conduction losses and microwave penetration depth were identified as key factors influencing microwave heating efficiency. The study demonstrated that  $\text{LiBH}_4$  released 13 wt% of  $\text{H}_2$  at 107 °C, significantly outperforming other hydrides due to enhanced conduction losses during its structural transitions. To further improve microwave responsiveness, Matsuo et al. proposed incorporating microwave absorbers (such as  $\text{TiH}_2$ , B, or C) into the  $\text{LiBH}_4$  system.<sup>[166]</sup> Experimental results showed that the composites containing these absorbers exhibited much faster heating rates than pure  $\text{LiBH}_4$ , releasing 6 wt%  $\text{H}_2$  within just 5 min. Notably, absorbers of C outperformed  $\text{TiH}_2$  and B, likely due to its superior thermal conductivity.

Similar to light-driven strategies, merely enhancing electromagnetic-to-thermal conversion efficiency is insufficient, meaning that an ideal dopant should possess both microwave absorption and catalytic properties. Therefore, some studies have also explored the non-thermal effects induced by microwave irradiation. In 2022, Zou et al. demonstrated that defect-rich titanium oxide ( $\text{TiO}_{2-x}$ ), formed through ball milling, acts as a “hotspot” under microwave irradiation, efficiently absorbing microwave energy and facilitating the reduction of  $\text{Ti}^{4+}$  to  $\text{Ti}^{2+}$  (Figure 14a–c).<sup>[167]</sup> This reduction process further promotes electron transfer between  $\text{Mg}^{2+}$  and  $\text{H}^-$ , enabling rapid dehydrogenation of  $\text{MgH}_2$  at 220 °C and significantly enhancing its hydrogen absorption performance. Although this study focused on the interaction between microwaves and catalysts, it offers new insights into developing more efficient microwave-assisted hydrogen storage catalysts.

Additionally, the design of microwave-responsive devices is also crucial for heating efficiency. Zhang et al. designed a honeycomb ceramic monolith coated with 0.54 wt% Ni for microwave-driven hydride dehydrogenation (Figure 14d–f).<sup>[168]</sup> Studies have shown that the  $\text{H}_2$  release rate of hydrides is positively correlated with the power and duration of microwave radiation. The device, under 1000 W microwave irradiation, can heat from room

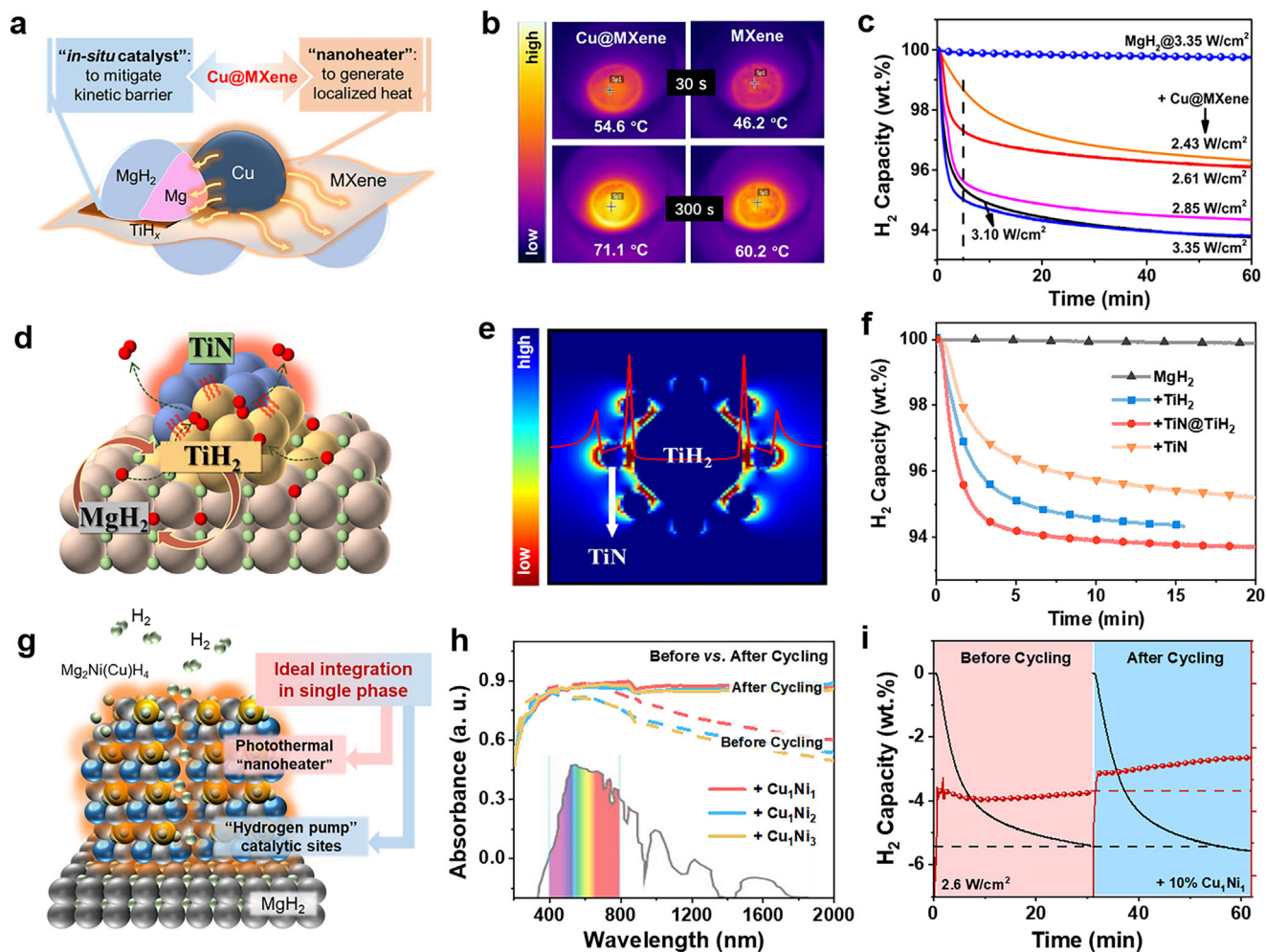


**Figure 13.** a) Schematic diagram of the solar-driven reversible hydrogen storage of  $\text{MgH}_2$  based on the photothermal and catalytic effect of  $\text{Cu@MXene}$ . b) In situ detection of surface temperature of  $\text{Cu@MXene}$  and  $\text{MXene}$  recorded by an infrared thermal imager under a light intensity of  $0.4 \text{ W cm}^{-2}$ . c)  $\text{H}_2$  desorption curves of  $\text{MgH}_2$  under the catalysis of  $\text{Cu@MXene}$  under different light intensities. Reproduced with permission.<sup>[162]</sup> Copyright 2022, Wiley-VCH. d) Schematic diagram of  $\text{TiN@TiH}_2@MgH_2$  coupled interface for solar-driven hydrogen storage. e) Theoretical FDTD simulated localized electric field enhancement profiles of  $\text{TiN@TiH}_2$ . f) Solar-driven  $\text{H}_2$  desorption of  $\text{MgH}_2$  under the catalysis of  $\text{TiH}_2$ ,  $\text{TiN@TiH}_2$ , and  $\text{TiN}$ , including ball-milled  $\text{MgH}_2$  for comparison under  $2.7 \text{ W cm}^{-2}$ . Reproduced with permission.<sup>[163]</sup> Copyright 2024, Wiley-VCH. g) Schematic diagram of the ideal integration of photothermal and catalytic effects via continuous in situ atomic reconstruction upon repeated dehydrogenation process. h) UV-vis-NIR absorption spectra of  $\text{MgH}_2$  under the catalysis of  $\text{Cu}_1\text{Ni}_1$ ,  $\text{Cu}_1\text{Ni}_2$ , and  $\text{Cu}_1\text{Ni}_3$  after cycling, in comparison with their pristine ball-milled states (before cycling). i) The response of temperature with corresponding  $\text{H}_2$  desorption curves of  $\text{MgH}_2$  under the catalysis of  $\text{Cu}_1\text{Ni}_1$  under  $2.6 \text{ W cm}^{-2}$  before and after cycling. Reproduced with permission.<sup>[21b]</sup> Copyright 2024, Springer Nature.

temperature to an incandescent state within 7 s, achieving a microwave-to-heat conversion efficiency of up to 90%. As a result, under 300 W microwave power, hydrides including  $\text{MgH}_2$ ,  $\text{NaAlH}_4$ ,  $\text{NaBH}_4$ , and  $\text{LiH}$  can complete dehydrogenation within 220 s, compared to over 720 s required by conventional electric heating.

#### 2.4.3. Other External Field-Driven Techniques

Other external field-driven sources include electrochemistry, electron beams, and fraction. Although research on enhancing hydrogen absorption and desorption through these methods remains limited, studies in related fields offer valuable insights into

the design and mechanistic understanding of hydrogen storage in hydrides. These technologies, utilizing non-conventional energy pathways, hold the potential to overcome the limitations of thermally driven process, enabling efficient hydrogen absorption and desorption under milder conditions.

Electrochemical-driven hydrogen absorption and desorption represent a key non-thermal method, extensively applied in the commercialization of nickel-metal hydride (Ni/MH) batteries.<sup>[4a,169]</sup> This technology relies on hydride alloys as anode materials to enable reversible electrochemical reactions through hydrogen uptake and release, with a more detailed summarized in Section 3.2. The advantage of electrochemical-driven hydrogen storage lies in their precise process control, allowing real-time regulation of hydrogen storage by adjusting the potential or

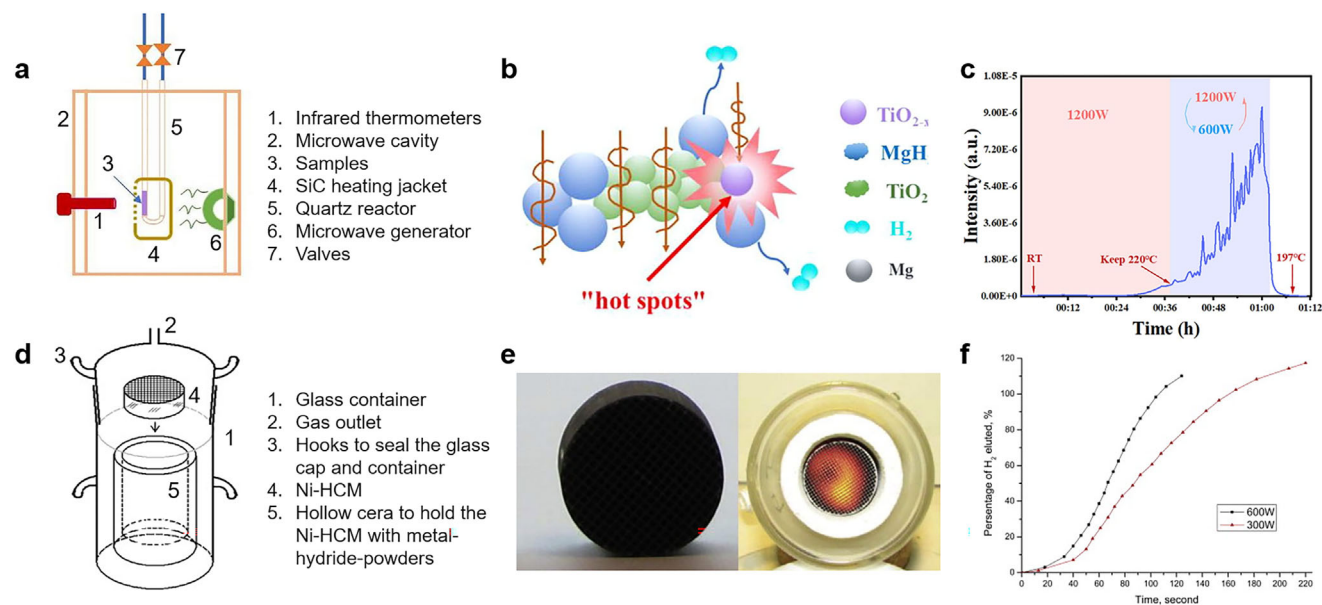


**Figure 14.** a) Schematic diagram of the microwave reactor system. b) Schematic diagram of the mechanism for microwave-induced vacancy formation in  $\text{TiO}_2$  and the generation of localized "hotspots." c) Mass spectrum of microwave-assisted isothermal dehydrogenation of +25 wt%  $\text{TiO}_2$ -microwave sample at 220 °C. Reproduced with permission.<sup>[167]</sup> Copyright 2022, Elsevier. d) Schematic home-made glass reactor for microwave-assisted dehydrogenation. e) HCM with Ni coating (Ni-HCM) and red-glowing Ni-HCM shortly after 1000 W microwave heating. f) Real time eluting-gas volume profiles obtained from 2.0 g of  $\text{MgH}_2$  under two different powers microwave heating: 300 W (red) and 600 W (black). Reproduced with permission.<sup>[168]</sup> Copyright 2011, Elsevier.

current. Furthermore, non-conventional hydrogen storage mechanisms induced by electrochemical processes, such as hydrogen diffusion pathways and the involvement of electron transfer and proton exchange, merit further exploration.

Electron beams, commonly used as illumination sources in TEM and scanning electron microscopy (SEM), are primarily employed to drive hydrogen absorption and desorption reactions, enabling in situ observation of the time-evolution of phase transitions in hydrides.<sup>[170]</sup> Regarding the interaction mechanisms between electron beams and hydrides, taking  $\text{MgH}_2$  as an example, Surrey et al. demonstrated that the dehydrogenation process is triggered by the inelastic scattering of incident electrons, which transferred to lattice vibrations and electronic transitions, leading to decomposition of  $\text{MgH}_2$ .<sup>[171]</sup> The high sensitivity of  $\text{MgH}_2$  to electron beams makes precise intensity control a major challenge in nanoscale hydrides. If employ electron beams are to be employed as an external field-driven technique for hydrogen storage, further studies are needed to link beam control with sample dimensions, and design of reaction apparatus remains a key obstacle.

Friction-driven methods convert external mechanical energy into the driving force for hydrogen reactions through mechanical friction stress-collision. Contrary to the conventional belief that local heating during ball milling triggers  $\text{H}_2$  desorption, Nevshupa et al. pointed out that the  $\text{H}_2$  release from  $\text{MgH}_2$  during friction may involve non-thermal mechanisms.<sup>[172]</sup> During deformation at the micro-/nano-scale, the temperature increase was  $<10$  °C, yet instantaneous ( $t < 1$  s) and substantial hydrogen release ( $3\text{--}50$  nmol  $\text{s}^{-1}$ ) was observed, with hydrogen nearly fully released within the affected microscopic region.<sup>[173]</sup> This findings indicate that friction-driven hydrogen release may involve

multiple microscopic mechanisms, including electronic and vibrational excitations, as well as dislocation movements. Future research should prioritize optimizing friction conditions and further investigating underlying mechanisms.

#### 2.4.4. Summary and Outlook

Research on external field-driven methods for driving hydrides, represented by electromagnetic wave-driven techniques, is still in its early stages. These methods promote hydrogen absorption and release through interactions with hydrides by exciting electrons, generating localized heating, or inducing chemical bond breakage within hydrides. Key challenges for future research include improving the conversion efficiency of electromagnetic waves to thermal energy for effective application to hydrides and delving deeper into the non-thermal effects between electromagnetic waves and hydrides (Figure 15).

On one hand, developing dopants with broader light spectrum responses or enhanced microwave absorption capabilities is crucial for achieving more efficient electromagnetic-to-thermal energy conversion. At the same time, optimizing interface structures and thermal conductivity will facilitate more effective heat transfer and utilization from the surface to the bulk of hydrides. On the other hand, understanding the unique non-thermal interaction mechanisms between electromagnetic waves and various hydrides, combined with optimizing the excitation and migration of photogenerated electrons, will offer theoretical guidance for achieving more efficient hydrogen storage under milder conditions. Additionally, at the macroscopic integration level, exploring effective strategies for assembling and scaling external

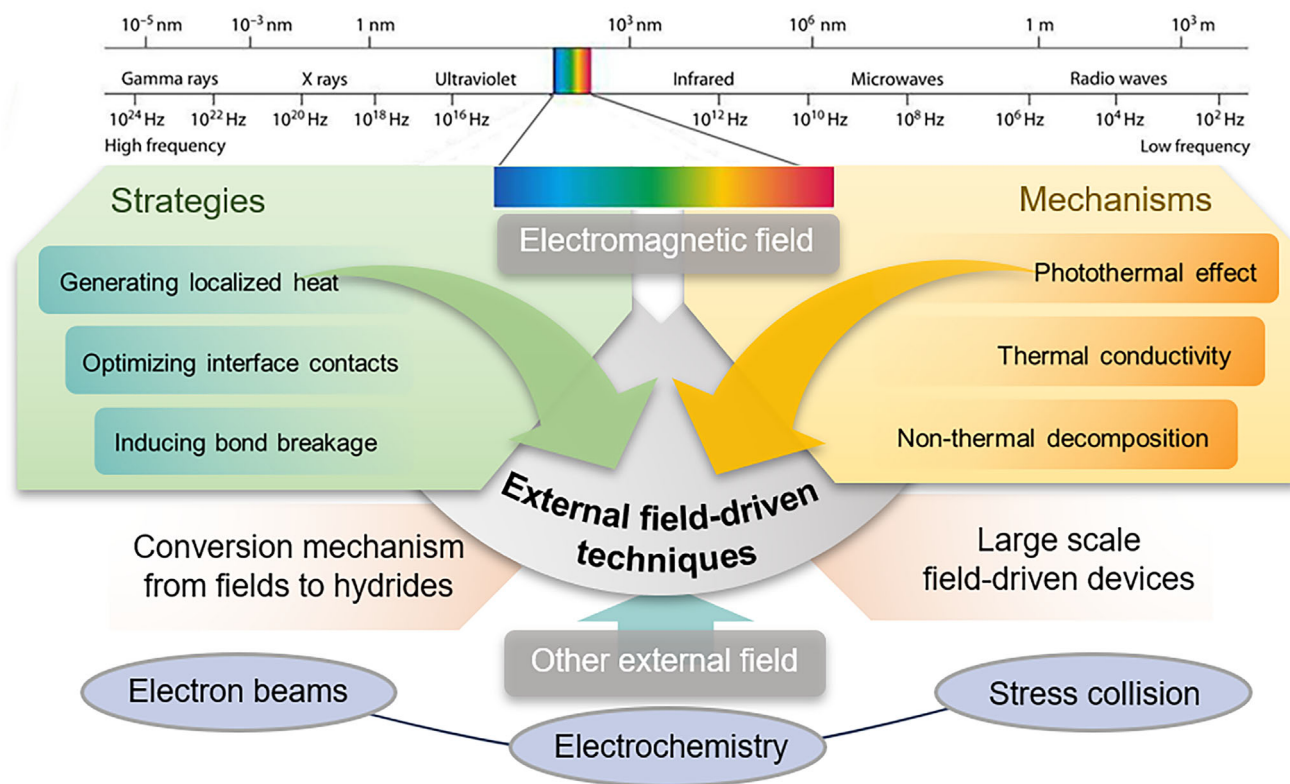


**Figure 15.** Summary diagram of external field types, strategies, and mechanisms for hydrogen storage using external field-driven technologies.

field-driven hydrogen storage devices will be crucial for practical applications in the future.

### 3. Lithium Storage Application

Although Li/Mg-based borohydrides exhibit favorable reduction stability and electrode compatibility, their high ionic conductivity is typically achieved only at elevated temperatures. Moreover, despite the high lithium storage capacity of Li/Mg-based hydrides, issues such as reaction irreversibility, interfacial side reactions, and volume expansion lead to a significant decline in capacity over cycling, severely limiting their practical applications.

To address these critical challenges, a series of modification strategies have been proposed. As illustrated in **Figure 16**, the recent advancements in hydride electrolytes and electrodes have further accelerated progress in this field, marking several significant milestones and achievements that underscore the effectiveness of these strategies. This section summarizes the typical modification methods for Li/Mg-based borohydrides as solid electrolytes, categorized into cation and/or anion substitution, nanoconfinement, and composition alteration. Additionally, the modification strategies for Li/Mg-based hydrides as electrode materials, including catalysis and nanostructuring, are also discussed.

#### 3.1. Hydride Electrolytes

Solid-state electrolytes based on Li/Mg hydrides have emerged as promising candidates in the realm of solid-state electrolytes,

offering several advantages over their oxide, polymer, and sulfide counterparts. These include low grain boundary resistance, high ionic selectivity, excellent reduction stability, mechanical flexibility, ease of integration into devices, and lower processing costs.<sup>[174]</sup> Such characteristics render hydrides particularly attractive for various applications. Although  $\text{Li}_2\text{NH}$  is the first hydride that demonstrates a high ionic conductivity of  $0.3 \text{ mS cm}^{-1}$  at room temperature, the intensive research in the field of solid-state electrolytes using hydrides is triggered by the discovery of high ionic conductivity  $\text{LiBH}_4$  in 2007.<sup>[175]</sup> Through impedance spectroscopy, Matsuo et al. observed a temperature-dependent increase in the ionic conductivity of  $\text{LiBH}_4$ , with a discontinuous jump occurring at  $\sim 115 \text{ }^\circ\text{C}$  (**Figure 17a**). At this point, the ionic conductivity reached  $10^{-3} \text{ S cm}^{-1}$ , comparable to that of high-performance lithium-ion conductors at ambient conditions. This drastic increase was attributed to a structural phase transition, wherein  $\text{LiBH}_4$  transformed from orthorhombic  $Pnma$  phase to hexagonal  $P6_3mc$  phase at elevated temperatures (**Figure 17b**), facilitating lithium ion transport. In this high-temperature hexagonal phase, atomic reorganization along the  $a$  and  $b$  axes likely promotes unimpeded  $\text{Li}^+$  migration in these directions. Besides, nuclear magnetic resonance spectroscopy (**Figure 17c**) further confirmed that the phase transition resulted in a narrowing of the  $\text{Li}^+$  peak and the emergence of satellite peaks, indicative of increased  $\text{Li}^+$  mobility. The reduced central peak linewidth highlights the accelerated ion dynamics in the high-temperature phase.

Recognizing the potential of  $\text{LiBH}_4$  as a solid-state lithium-ion electrolyte, researchers have since made concerted efforts to enhance its ionic conductivity at lower temperatures through

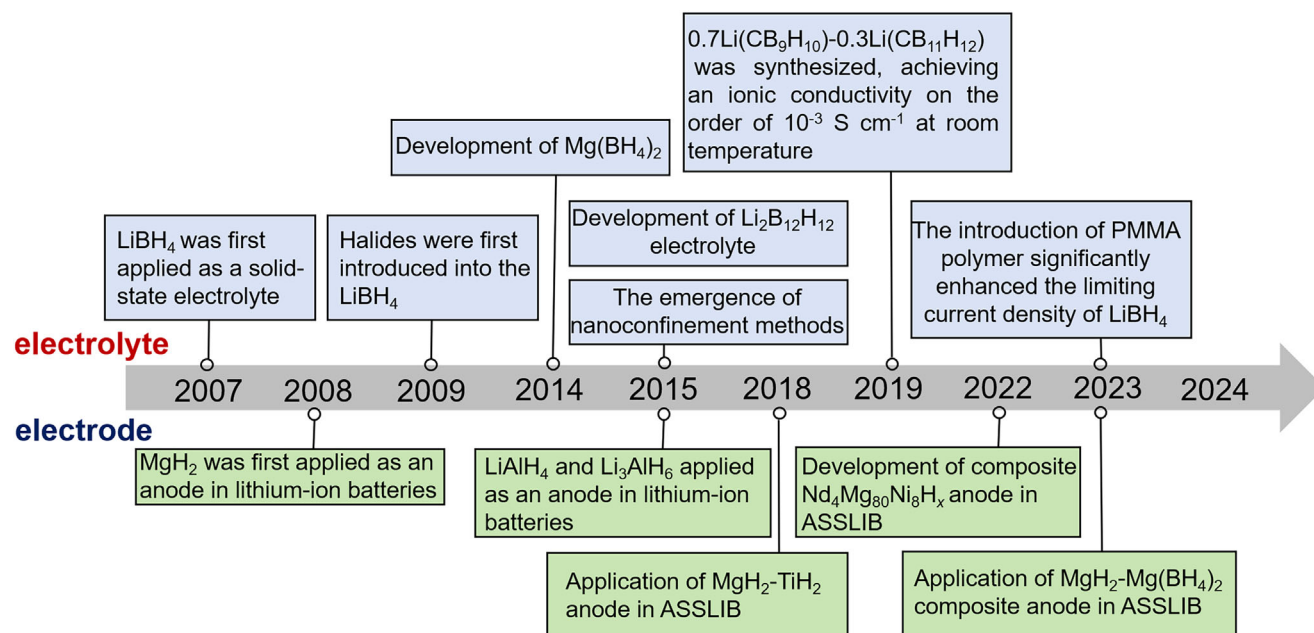


Figure 16. Timeline of developments in terms of typical Li/Mg-based hydride electrodes and solid-state electrolytes.<sup>[7a,177,182,187,197,202,203,209,217,218,231]</sup>

various modification strategies. Concurrently, borohydrides have gained significant attention due to their unique ability to form stable compounds with alkali and alkaline-earth cations, positioning them as strong candidates for fast-ion conductors. As shown in Figure 17d, recent studies have further explored the properties

of metal borohydrides (such as Na<sup>+</sup> and Mg<sup>2+</sup>) as potential solid-state ion electrolytes, and their feasibility has been demonstrated in these systems.<sup>[176]</sup> Various strategies have been developed to improve the electrochemical performance of Li/Mg-based hydrides as the ion conductors. This section reviews Li/Mg-based

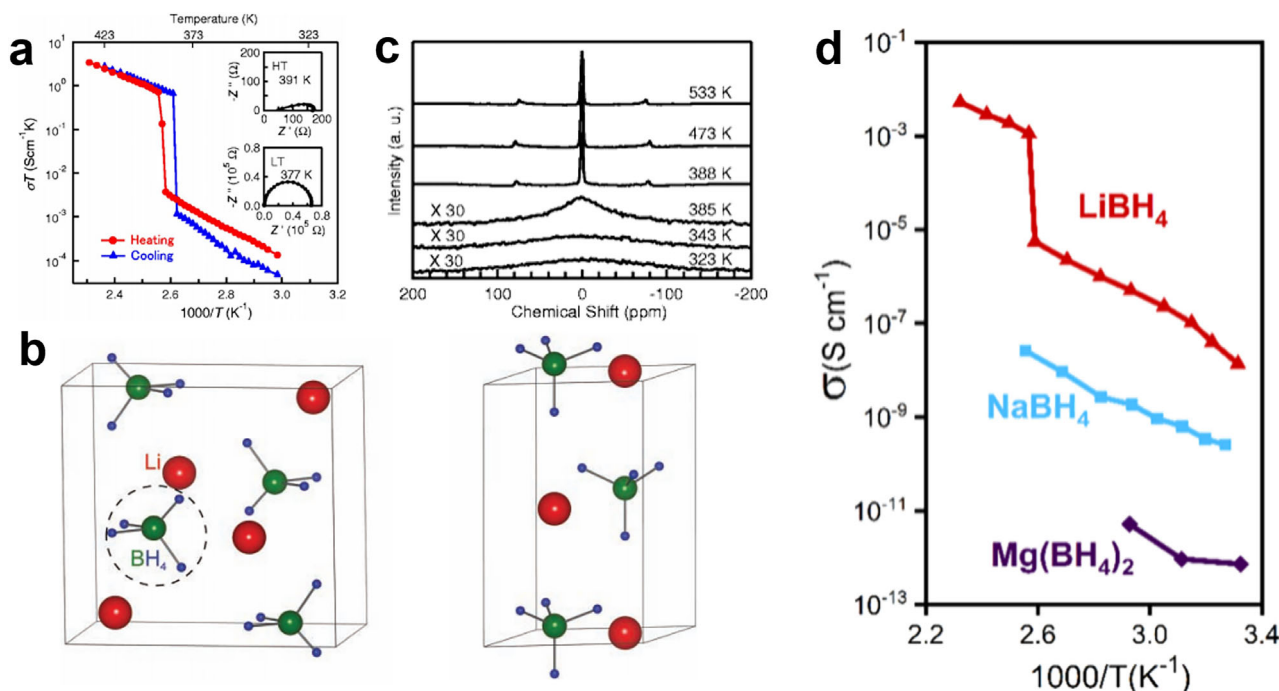


Figure 17. a) Temperature dependence of the electrical conductivity of LiBH<sub>4</sub>. Reproduced with permission.<sup>[175b]</sup> Copyright 2007, AIP. b) Crystal structures of the low-temperature and high-temperature phases of LiBH<sub>4</sub>. Reproduced with permission.<sup>[232]</sup> Copyright 2011, Wiley-VCH. c) <sup>7</sup>Li ( $I = 3/2$ ) NMR spectra of LiBH<sub>4</sub> at some selected temperatures. Reproduced with permission.<sup>[175b]</sup> Copyright 2007, AIP. d) Temperature-dependent conductivities of LiBH<sub>4</sub>, NaBH<sub>4</sub>, and Mg(BH<sub>4</sub>)<sub>2</sub>. Reproduced with permission.<sup>[207]</sup> Copyright 2022, Elsevier.

borohydrides and discusses the corresponding performance improvement strategies for solid-state batteries (SSBs), as summarized in **Table 3**.

### 3.1.1. Cation and/or Anion Substitution

The introduction of halides was one of the earliest strategies employed to enhance the ionic conductivity of  $\text{LiBH}_4$ . In 2009, Maekawa et al. reported that mixing and reheating pure  $\text{LiBH}_4$  with various  $\text{LiX}$  ( $X = \text{Cl}, \text{Br}, \text{I}$ ) led to significant improvement of electrochemical performance.<sup>[177]</sup> The substitution of the  $\text{BH}_4^-$  anions with larger halide anions ( $X^-$ ) caused lattice expansion, resulting in structural relaxation within the  $\text{LiBH}_4$  framework, which reduced the migration energy barrier for  $\text{Li}^+$  ions, thereby facilitating their transport through the solid electrolyte. This study revealed that the phase transition temperature of all  $\text{LiX}$ -doped samples decreased markedly, with the most significant reduction observed in the  $\text{LiI}$ -doped samples. Notably, the  $3\text{LiBH}_4 \cdot \text{LiI}$  compound exhibited the highest ionic conductivity at room temperature, reaching  $10^{-4} \text{ S cm}^{-1}$  (**Figure 18a**). XRD analysis indicated that the incorporation of  $\text{LiI}$  stabilized the high-temperature phase of  $\text{LiBH}_4$  even at lower temperatures (**Figure 18b**). Furthermore, NMR results further demonstrated that the peak corresponding to  $3\text{LiBH}_4 \cdot \text{LiI}$  was broader than that of  $\text{LiBH}_4 \cdot \text{LiI}$ , with the disappearance of the  $\text{LiI}$  peak, accompanied by the emergence of a peak corresponding to the high-temperature phase of  $\text{LiBH}_4$  (**Figure 18c**), suggesting that the substitution of  $\text{BH}_4^-$  with the highly polarizable  $\text{I}^-$  anion altered the electronic structure, resulting in changes in  $\text{Li}^+$  coordination. This modification leads to a lower activation energy (i.e., 0.56 eV) for ion migration in the composite sample. DFT calculations indicate that substituting the  $\text{BH}_4^-$  ion with halogen anions significantly reduces the energy difference between the low-temperature and high-temperature phases of  $\text{LiBH}_4$ , thereby promoting the stabilization of the high-temperature phase. Furthermore, the introduction of  $\text{LiI}$  results in the formation of lattice defects, such as vacancies and dislocations, which provides additional pathways and sites for  $\text{Li}^+$  migration, thereby enhancing ionic diffusion performance. Additionally, the ionic exchange between  $\text{I}^-$  and  $\text{BH}_4^-$  facilitates charge redistribution, further promoting  $\text{Li}^+$  migration. These findings provide important theoretical insights for optimizing the phase behavior and ionic conductivity of  $\text{LiBH}_4$ . Inspired by research demonstrating that anionic substitution can stabilize high-temperature phases and alter the coordination environment of  $\text{LiBH}_4$  at room temperature, a series of  $\text{LiBH}_4$ -related compositions based on cation and/or anion substitution have been developed recently.

Inspired by these results,  $\text{Li}^+$  conduction has also been discovered in other complex hydrides, which have been extensively studied as potential hydrogen storage materials. Yan et al. prepared  $\text{Li}(\text{BH}_4)_{1-x}(\text{NH}_2)_x$  solid solution samples ( $x = 3/4, 2/3$ ) by ball-milling and subsequent heat treatment of  $\text{LiBH}_4$  and  $\text{LiNH}_2$ .<sup>[178]</sup> The crystal structure of the  $\alpha$  phase, as shown in the **Figure 18d**,  $\text{Li}(\text{BH}_4)_{1/2}(\text{NH}_2)_{3/4}$  crystallizes in a cubic lattice (space group  $I2_13$ ), characterized by three distinct lithium coordination environments (**Figure 21a**). Each lithium ion is tetrahedrally coordinated by a mixture of  $\text{BH}_4^-$  and  $\text{NH}_2^-$  anions. Additionally, the structure contains an equivalent number of va-

cant tetrahedral sites to maintain charge neutrality. Compared to the previously discussed monoatomic anion doping (e.g.,  $\text{I}^-$ ), introducing the  $\text{NH}_2^-$  anionic group can facilitate reorientation of the anions, particularly the polar  $\text{NH}_2^-$ , thereby enhancing the ionic conductivity of the material.<sup>[179]</sup> In the same sublattice of the  $\alpha$ -phase lithium amidoborohydride, lithium ions experience lower hopping energy between tetrahedral sites sharing two edges. This significantly reduces the energy barrier and enables efficient lithium migration within the cubic  $\alpha$ -phase. When  $x = 2/3$ , the  $\text{NH}_2^-$  units in the solid solution are partially replaced by the larger  $\text{BH}_4^-$ , which increases the lattice spacing. Combined with the presence of a disordered phase with high conductivity, this further enhances the ionic conductivity of the electrolyte. Therefore, both samples exhibited high ionic conductivity at room temperature ( $0.2 \text{ mS cm}^{-1}$  for  $x = 3/4$  and  $6.4 \text{ mS cm}^{-1}$  for  $x = 2/3$  at  $40^\circ\text{C}$ ). Building on this work, this researcher added  $\text{LiOH}$  in the synthetic procedure and synthesized  $\text{LiBH}_4 \cdot 1/2\text{NH}_3$  solid electrolyte by ball-milling a mixture of  $\text{LiBH}_4$ ,  $\text{LiNH}_2$ , and  $\text{LiOH}$  according to the reaction:  $2\text{LiBH}_4 + \text{LiNH}_2 + \text{LiOH} \rightarrow 2\text{LiBH}_4 \cdot 1/2\text{NH}_3 + \text{Li}_2\text{O}$ .<sup>[180]</sup> Compared to the single  $2\text{LiBH}_4 \cdot 1/2\text{NH}_3$  electrolyte, the in situ formed nanocrystalline  $\text{Li}_2\text{O}$  effectively enhances the thermal and mechanical stability of the electrolyte, which may form better contact with the electrodes. In-depth studies the structure and lithium-ion coordination environment of this electrolyte reveal that this crystal structure of  $2\text{LiBH}_4 \cdot 1/2\text{NH}_3$  identified as an orthorhombic system with space group  $Pna2_1$ , featuring two distinct lithium coordination sites, both in tetrahedral environments. The researchers proposed that the presence of  $\text{NH}_3$  molecules alters the coordination between the framework and lithium ions during migration. Specifically,  $\text{NH}_3$  molecules stabilize the interstitial  $\text{Li}^+$ , promoting rapid lithium-ion migration within the  $a$ - $c$  plane. As a result, the material exhibited an ionic conductivity of  $0.7 \text{ mS cm}^{-1}$  at  $40^\circ\text{C}$ , showcasing its potential as a high-performance solid electrolyte. In addition, Zhang et al. moved beyond traditional elemental doping approaches by introducing gas molecules ( $\text{NH}_3$ ) into  $\text{LiBH}_4$ .<sup>[181]</sup> By controlling the crystal structure of the ammoniated compound through “solid-gas” dynamic equilibrium at different temperatures. The adsorption of  $\text{NH}_3$  induced the formation of defects and reduced the lithium ion volume density, resulting in enhanced conductivity. Based on this, they synthesized  $\text{Li}(\text{NH}_3)_n\text{BH}_4$ , which achieved an ionic conductivity of  $2.21 \text{ mS cm}^{-1}$  at  $40^\circ\text{C}$ .

More importantly, this approach could be applied to  $\text{Mg}(\text{BH}_4)_2$ . Higashi et al. first utilized mechanical ball milling to blend  $\text{Mg}(\text{BH}_4)_2$  with  $\text{Mg}(\text{NH}_2)_2$  in 2014, successfully incorporating the  $\text{NH}_2^-$  group into the  $\text{Mg}(\text{BH}_4)_2$  structure.<sup>[182]</sup> The incorporation of  $\text{NH}_2^-$  groups significantly altered the structure, reducing the magnesium atom spacing and enhancing  $\text{Mg}^{2+}$  diffusion. Besides, the  $\text{NH}_2^-$  groups interact with  $\text{Mg}$  and  $\text{H}$ , creating additional ion migration pathways, resulting in an ionic conductivity of  $10^{-6} \text{ S cm}^{-1}$  at  $150^\circ\text{C}$  and improved oxidative stability within a range of 3 V. In 2020, Jensen et al. reacted  $\text{NH}_3$  with  $\text{Mg}(\text{BH}_4)_2$  to synthesize  $\text{Mg}(\text{BH}_4)_2 \cdot \text{NH}_3$ , revealing that the interaction of  $\text{NH}_3$  with  $\text{Mg}^{2+}$  and  $\text{BH}_4^-$  enhanced the structural flexibility, further promoting  $\text{Mg}^{2+}$  ion conduction.<sup>[183]</sup> Furthermore, Zheng et al. synthesized amorphous  $\text{Mg}(\text{BH}_4)_2 \cdot 2\text{NH}_3$  with a 3D framework by reacting  $\text{NH}_3$  with  $\gamma\text{-Mg}(\text{BH}_4)_2$ .<sup>[183b]</sup> Compared to  $\gamma\text{-Mg}(\text{BH}_4)_2$  and  $\text{Mg}(\text{BH}_4)_2 \cdot \text{NH}_3$  (**Figure 18e**), this

**Table 3.** Performance comparison of hydride-based electrolytes.

Solid-state electrolytes	Conductivity [mS cm <sup>-1</sup> ]	Temperature [°C]	Refs.
Li <sub>2</sub> B <sub>12</sub> H <sub>12</sub>	3.1	RT	[231b]
LiCB <sub>11</sub> H <sub>12</sub>	150	130	[194]
LiCB <sub>9</sub> H <sub>10</sub>	100	110	[264]
0.7Li(CB <sub>9</sub> H <sub>10</sub> )/0.3Li(CB <sub>11</sub> H <sub>12</sub> )	6.7	25	[197]
LiBH <sub>4</sub> /γ-Al <sub>2</sub> O <sub>3</sub> /PEO	3	60	[265]
LiBH <sub>4</sub> /LiNH <sub>2</sub> /g-C <sub>3</sub> N <sub>4</sub>	1.5	30	[266]
Li <sub>4</sub> (BH <sub>4</sub> ) <sub>3</sub> I@SBA-15	0.25	35	[206]
LiBH <sub>4</sub> /BN	0.11	40	[267]
LiBH <sub>4</sub> /1/2NH <sub>3</sub>	0.7	40	[180a]
LiBH <sub>4</sub> @Al <sub>2</sub> O <sub>3</sub>	0.2	RT	[268]
LiBH <sub>4</sub> /LiNO <sub>3</sub>	0.19	70	[269]
Heated-400LiBH <sub>4</sub>	1.38	25	[270]
Li(NH <sub>3</sub> ) <sub>x</sub> BH <sub>4</sub> @SiO <sub>2</sub>	39.5	60	[217]
3LiBH <sub>4</sub> -LiI	~10 <sup>-4</sup>	RT	[177]
LiBH <sub>4</sub> @SiO <sub>2</sub> (MCM-41)	0.1	RT	[187]
LiBH <sub>4</sub> /MgO/MgI <sub>2</sub>	0.145	50	[174a]
LiBH <sub>4</sub> /LiNH <sub>2</sub> -Al@SBA-15	0.5	30	[271]
LiBH <sub>4</sub> /ZrO <sub>2</sub>	0.016	25	[272]
LiBH <sub>4</sub> ·AB	0.4	25	[174a]
LLZTO/4LiBH <sub>4</sub>	0.08	30	[200]
Heated-LiBH <sub>4</sub> /5PMMA	0.4	RT	[270]
LiBH <sub>4</sub> /oxide (SiO <sub>2</sub> , CaO, MgO, γ-Al <sub>2</sub> O <sub>3</sub> , TiO <sub>2</sub> and ZrO <sub>2</sub> )	0.26	40	[198]
(3LiBH <sub>4</sub> -LiI)-20P <sub>2</sub> S <sub>5</sub>	0.38	30	[200]
AOLIBHI-5PMMA	0.1	RT	[273]
Li(NH <sub>3</sub> ) <sub>n</sub> BH <sub>4</sub>	2.21	40	[181a]
Li <sub>2</sub> B <sub>12</sub> H <sub>12</sub> -5Li <sub>2</sub> B <sub>10</sub> H <sub>10</sub> -6LiBH <sub>4</sub>	0.1	RT	[174a]
Heated LiBH <sub>4</sub>	0.27	35	[274]
PEO/Li <sub>4</sub> (BH <sub>4</sub> ) <sub>3</sub> I	0.41	70	[200]
Li(BH <sub>4</sub> ) <sub>1/3</sub> (NH <sub>2</sub> ) <sub>2/3</sub>	6.4	40	[200,275]
LiCe(BH <sub>4</sub> ) <sub>3</sub> Cl	0.1	20	[184]
4LiBH <sub>4</sub> -NaCl	0.006	60	[185]
2LiBH <sub>4</sub> -NaI	0.015	60	[185]
Li <sub>2</sub> NH	0.3	25	[175a]
LiNH <sub>2</sub>	4 × 10 <sup>-4</sup>	RT	[232]
LiAlH <sub>4</sub>	0.005	120	[276]
Li <sub>3</sub> AlH <sub>6</sub>	0.02	120	[276]
Mg(BH <sub>4</sub> )(NH <sub>2</sub> )	0.001	150	[182]
Mg(en)(BH <sub>4</sub> ) <sub>2</sub>	0.06	70	[277]
Mg(BH <sub>4</sub> ) <sub>2</sub> (NH <sub>3</sub> BH <sub>3</sub> ) <sub>2</sub>	0.013	30	[278]
Mg(BH <sub>4</sub> ) <sub>2</sub> NH <sub>3</sub>	0.33	80	[180a]
Mg(BH <sub>4</sub> ) <sub>2</sub> ·2NH <sub>3</sub>	0.5	75	[183b]
Mg(BH <sub>4</sub> ) <sub>2</sub> ·1.47NH <sub>3</sub> @SBA-15	0.27	80	[279]
β-Mg(BH <sub>4</sub> ) <sub>2</sub> ·CH <sub>3</sub> NH <sub>2</sub>	0.15	25	[280]
Mg(BH <sub>4</sub> ) <sub>2</sub> ·1.6NH <sub>3</sub> /Al <sub>2</sub> O <sub>3</sub>	0.025	22	[281]
Mg(BH <sub>4</sub> ) <sub>2</sub> ·1.6(NH <sub>3</sub> )-MgO	0.01	RT	[180a]
Mg(BH <sub>4</sub> ) <sub>2</sub> ·1.5(NH <sub>3</sub> )- Y <sub>2</sub> O <sub>3</sub> -ZrO <sub>2</sub>	0.296	25	[176b]

electrolyte possesses a greater number of Mg vacancies and lower migration energy barriers, achieving an ionic conductivity of  $5 \times 10^{-4}$  S cm<sup>-1</sup> at 75 °C.

Similar to the anions incorporation, the introduction of metal cations could also increase the Li<sup>+</sup> transport pathways in LiBH<sub>4</sub>, thereby effectively enhancing its conductivity. In 2012, Ley et al. introduced Ce<sup>3+</sup> cations into LiBH<sub>4</sub> and synthesized LiCe(BH<sub>4</sub>)<sub>3</sub>Cl by mechanical ball milling of CeCl<sub>3</sub> and LiBH<sub>4</sub> with various molar ratios.<sup>[184]</sup> This compound crystallizes in the cubic structure composed of isolated tetranuclear anionic clusters [Ce<sub>4</sub>Cl<sub>4</sub>(BH<sub>4</sub>)<sub>12</sub>]<sup>4-</sup>. The core of the cluster is a distorted cubane Ce<sub>4</sub>Cl<sub>4</sub> structure, with Li<sup>+</sup> ions disordered throughout the lattice, acting as charge balancers. According to the structural model of LiCe(BH<sub>4</sub>)<sub>3</sub>Cl, only 2/3 of the Li<sup>+</sup> positions (12*d* Wyckoff site) are occupied in a disordered manner (Figure 18f). The disordered distribution of Li<sup>+</sup> ions and the presence of vacancies increase the pathways for Li<sup>+</sup> migration, thereby enhancing the ionic conductivity. As a result, LiCe(BH<sub>4</sub>)<sub>3</sub>Cl achieves an ionic conductivity of 10<sup>-4</sup> S cm<sup>-1</sup> at 20 °C. In 2018, Xiang et al. mixed LiBH<sub>4</sub> with NaCl or NaI using ball milling to prepare LiBH<sub>4</sub>-NaX (X = Cl, I) composites, introducing both Na<sup>+</sup> cations and X<sup>-</sup> anions.<sup>[185]</sup> During ball milling process, LiBH<sub>4</sub> would react with NaCl or NaI to form LiBH<sub>4</sub>-NaBH<sub>4</sub>-LiX compounds. These various solid solutions and eutectic structures facilitate lithium ion migration. Additionally, differential scanning calorimetry (DSC) results showed that the phase transition temperature of the LiBH<sub>4</sub>-NaX composites decreased by ~10 °C compared to pure LiBH<sub>4</sub> (Figure 18g), indicating that the incorporation of NaX helps stabilize the high-conductivity phase of LiBH<sub>4</sub> at elevated temperatures. Ultimately, the optimal compositions, 4LiBH<sub>4</sub>-NaCl and 2LiBH<sub>4</sub>-NaI, achieved ionic conductivities of 0.006 and 0.015 mS cm<sup>-1</sup> at 60 °C (Figure 18h), respectively. These values are nearly 100 times higher than those of pristine LiBH<sub>4</sub> at temperatures below 100 °C.

In short, the implementation of both anion and cation doping strategies significantly enhances the ionic conductivity of materials. Anion doping, by substituting larger anions, induces lattice expansion and structural relaxation, which in turn reduces the energy barrier for ion migration. This approach not only improves ion diffusion pathways but also adjusts the electronic structure of the material through changes in anion polarizability, thereby further optimizing ion transport channels. Cation doping, on the other hand, introduces new cations that create lattice defects such as vacancies and dislocations, providing additional migration pathways for ions. Moreover, the exchange between doped cations and the host ions promotes charge redistribution, which further facilitates ion migration. These doping mechanisms not only effectively increase the ionic conductivity but also significantly broaden the material's operational range across various temperatures, making them suitable for a wider range of applications.

### 3.1.2. Nanoconfinement

Inspired by the nanoconfinement effect in improving hydro- gen storage performance of LiBH<sub>4</sub>, in which high-temperature

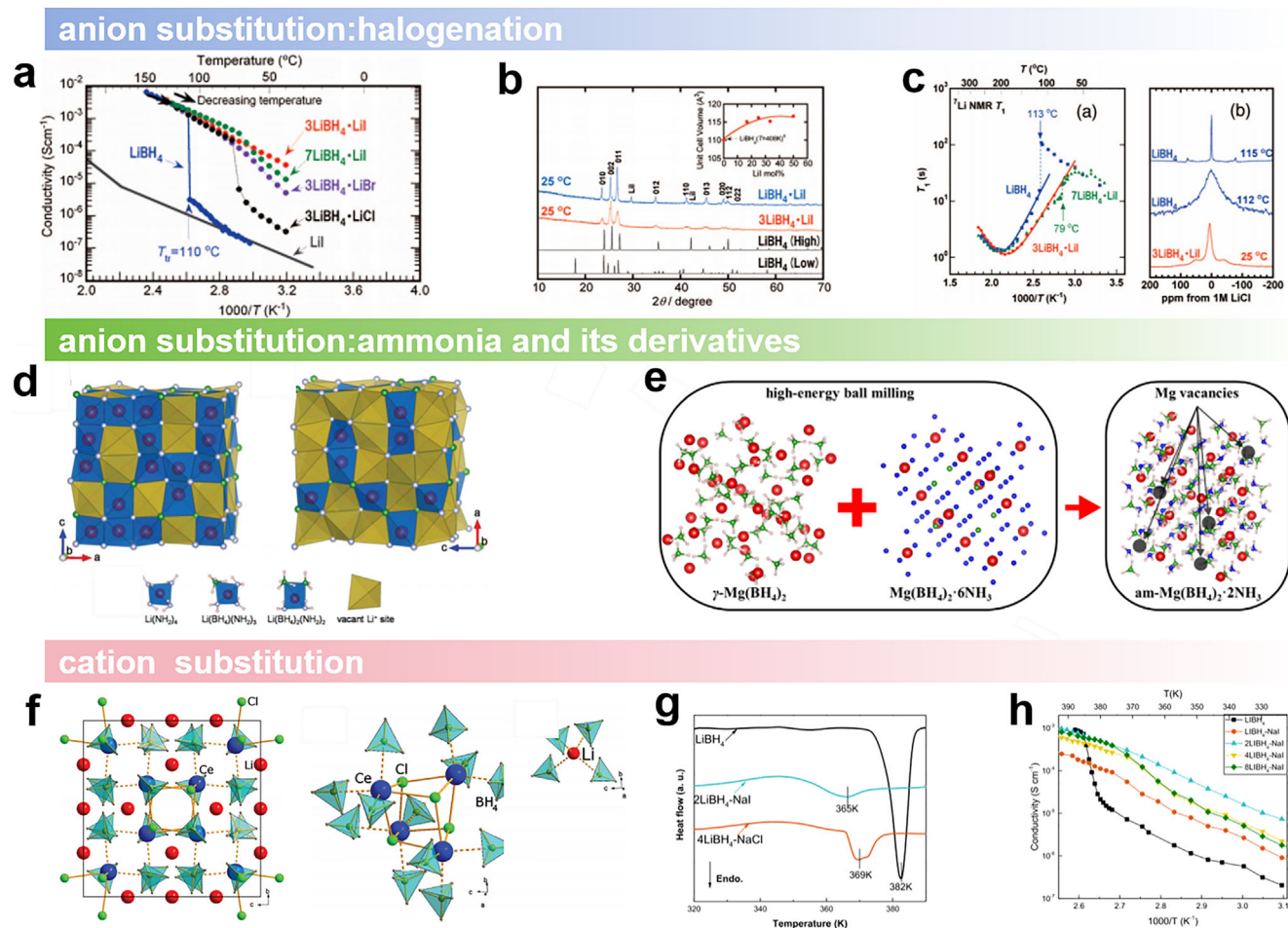


**Figure 18.** a) Temperature-dependent conductivities of  $\text{LiBH}_4\text{--LiX}$  ( $X = \text{Cl}, \text{Br}, \text{I}$ ). b) XRD pattern of  $\text{LiBH}_4\text{--LiI}$  at  $25^\circ\text{C}$  and calculated XRD patterns for low- and high-temperature forms of  $\text{LiBH}_4$ . c) Temperature dependence of  $^7\text{Li}$  NMR spectra for  $\text{LiBH}_4$  and  $3\text{LiBH}_4\text{--LiI}$ , respectively, and temperature variation of  $^7\text{Li}$  NMR spectra for  $\text{LiBH}_4$  and  $7\text{LiBH}_4\text{--LiI}$ . Reproduced with permission.<sup>[177]</sup> Copyright 2009, American Chemical Society. d) The crystal structure of the cubic  $\alpha$  phase for  $x = 3/4$  and its symmetry-related dual structure. Reproduced with permission.<sup>[178]</sup> Copyright 2017, Wiley-VCH. e) Schematic illustration of the design principle of  $\text{am-Mg(BH}_4)_2 \cdot 2\text{NH}_3$ . Reproduced with permission.<sup>[183b]</sup> Copyright 2023, Wiley-VCH. f)  $[\text{Ce}_4\text{Cl}_4(\text{BH}_4)_{12}]^{4-}$  tetranuclear anionic cluster with a distorted cubane  $\text{Ce}_4\text{Cl}_4$  core and tetrahedral coordination of  $\text{Li}$  to four  $\text{BH}_4$  groups. Reproduced with permission.<sup>[184]</sup> Copyright 2012, American Chemical Society. g) DSC curves of  $\text{LiBH}_4\text{--NaX}$  composites after ball milling. h) Temperature dependencies of ionic conductivity for  $\text{LiBH}_4$  and  $x\text{LiBH}_4\text{--NaI}$  composites. Reproduced with permission.<sup>[185]</sup> Copyright 2018, Elsevier.

phases of  $\text{LiBH}_4$  could be stabilized at room temperature, nanoconfinement is widely regarded as an effective strategy for enhancing the ionic conductivity of  $\text{LiBH}_4$ . In 2011, Ngene et al. pioneered the nanoconfinement of  $\text{LiBH}_4$  using nickel-doped nanoporous carbon as a substrate, revealing that the high surface area of the porous carbon significantly increases the reaction sites, thereby improving the overall hydrogen storage performance.<sup>[186]</sup> However, compared to carbon with high conductivity and uneven pore sizes,  $\text{SiO}_2$  exhibits lower electronic conductivity, highly uniform and tunable pore sizes, and a stable structure that performs better under high-pressure loads. In 2015, Blanchard et al. successfully infiltrated molten  $\text{LiBH}_4$  into mesoporous  $\text{SiO}_2$  (MCM-41) under high-pressure conditions for the first time.<sup>[187]</sup> By optimizing the pore size and loading rate, they achieved an ionic conductivity of  $0.1 \text{ mS cm}^{-1}$  at  $40^\circ\text{C}$  for the optimal sample (Figure 19a), confirming significant functional changes due to interfacial effects and size reduction in

solid materials. NMR analysis demonstrated that  $\text{LiBH}_4$  within the silica nanopores exhibited two distinct lithium ion ( $\text{Li}^+$ ) migration mechanisms, suggesting the presence of two different  $\text{LiBH}_4$  components after nanoconfinement (Figure 19b). The confined  $\text{LiBH}_4@ \text{SiO}_2$  electrolyte displayed slowly migrating  $\text{BH}_4^-$  anions in the bulk region, while a layer of rapidly migrating anions was observed near the scaffold walls and grain boundaries. This discovery indicates that nanoconfinement could provide rapid ionic migration pathways at the grain boundaries, significantly enhancing the ionic conductivity of  $\text{LiBH}_4$ . However, how these fractions with different  $\text{Li}^+$  mobilities influence the overall ionic conductivity of the nanocomposite is not yet understood. Building upon this foundation, Lambregts et al. conducted further investigations, studying the temperature behavior of  $\text{LiBH}_4$  in these two fractions, with a primary focus on the local environment and dynamics within these  $\text{LiBH}_4$  fractions.<sup>[188]</sup> They used NMR techniques to confirm that under nanoconfinement

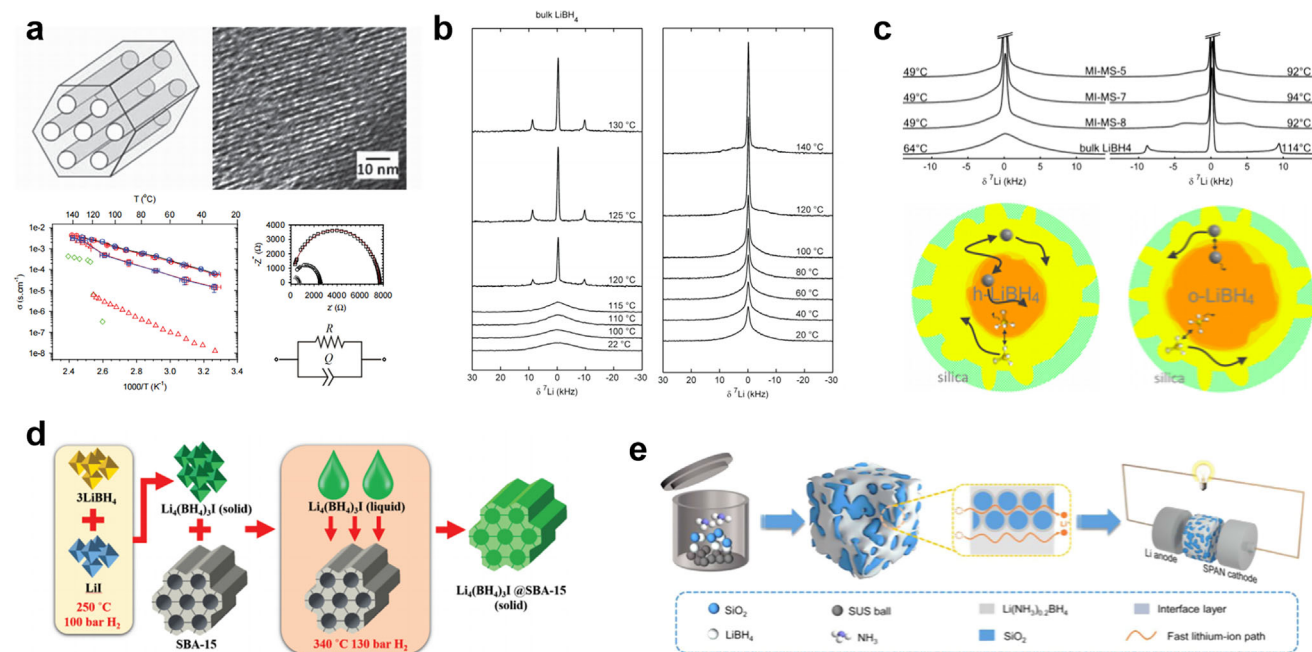


**Figure 19.** a) Schematic representation of the porosity in MCM-41 ordered mesoporous silica scaffolds, bright-field transmission electron micrograph of a  $\text{SiO}_2$  scaffold particle, and Arrhenius plots of the ionic conductivities of  $\text{SiO}_2$ - $\text{LiBH}_4$  nanocomposites and bulk  $\text{LiBH}_4$ . b) Static-solid state  $^7\text{Li}$  NMR measurements. Reproduced with permission.<sup>[187]</sup> Copyright 2014, Wiley-VCH. c)  $^7\text{Li}$  NMR spectra of bulk  $\text{LiBH}_4$  and  $\text{LiBH}_4$  confined in 5–8 nm silica pores, measured at temperatures below (left) and above (right) their respective structural phase transition temperatures. Model of nanoconfined  $\text{LiBH}_4$  showing the cross section of a single silica pore. Reproduced with permission.<sup>[188]</sup> Copyright 2019, American Chemical Society. d) A schematic diagram of the preparing process of  $\text{Li}_4(\text{BH}_4)_3\text{I}$  in SBA-15. Reproduced with permission.<sup>[206]</sup> Copyright 2019, Wiley-VCH. e) Schematic illustration of the electrolyte synthesis and an integrated all-solid-state battery of  $\text{Li}/\text{Li}(\text{NH}_3)_{0.2}\text{BH}_4@/\text{SiO}_2/\text{SPAN}$ . Reproduced with permission.<sup>[190]</sup> Copyright 2022, American Chemical Society.

conditions,  $\text{Li}^+$  and  $\text{BH}_4^-$  in  $\text{LiBH}_4$  could be distinguished into two components at all temperatures. One component of  $\text{LiBH}_4$  exhibited a faster ionic migration rate, allowing both  $\text{Li}^+$  and  $\text{BH}_4^-$  to diffuse rapidly within the material, while the other component, apart from differing in phase transition temperature, exhibited characteristics similar to bulk  $\text{LiBH}_4$ . DSC and NMR analyses demonstrated that the  $\text{LiBH}_4$  with high migration rates predominantly resides on the pore walls of SBA-15, and that the  $\text{LiBH}_4$  closer to the core region of the pores exhibits properties increasingly similar to the bulk material. Furthermore, a space charge model used to elucidate this phenomenon indicates ions may be attracted to or repelled by charges on the surface of the insulator, such as  $\text{SiO}_2$ , resulting in the formation of defects within the ionic lattice, with the density of these defects decreasing exponentially with distance from the insulator (Figure 19c). The formation of these defects enhances the ionic migration rate. However, the dynamic phase in this system is so active that it is not considered to have a clear lattice structure. Additionally, the complex undulating porosity of  $\text{SiO}_2$  may interfere with the crystallization of  $\text{LiBH}_4$  on its surface, thus affecting its conductivity, which is a phenomenon that requires further investigation. This method has strong general applicability, enhancing not only bulk  $\text{LiBH}_4$  but also the electrochemical performance of modified  $\text{LiBH}_4$ -based electrolyte derivatives. For instance, Lu et al. combined I ions doping with nanoconfinement strategy, successfully infiltrating molten  $\text{Li}_4(\text{BH}_4)_3\text{I}$  into the SBA-15 framework to synthesize  $\text{Li}_4(\text{BH}_4)_3\text{I}@/\text{SBA-15}$  (Figure 19d),

which exhibits an ionic conductivity of  $2.5 \times 10^{-4} \text{ S cm}^{-1}$  at  $35^\circ\text{C}$ .<sup>[189]</sup> The presence of a stable interfacial phase also allows  $\text{Li}_4(\text{BH}_4)_3\text{I}@/\text{SBA-15}$  to display a relatively wide electrochemical stability window (0–5 V vs  $\text{Li}/\text{Li}^+$ ) and excellent lithium dendrite suppression capability, along with superior electrochemical performance in full battery applications. In addition, Liu et al. prepared the  $\text{Li}(\text{NH}_3)_x\text{BH}_4@/\text{SiO}_2$  composite by introducing ammonia into  $\text{LiBH}_4@/\text{SiO}_2$  at room temperature, resulting in the formation of fast  $\text{Li}^+$  migration pathways (Figure 19e).<sup>[190]</sup> Both experimental results and DFT calculations reveal that the composite exhibits a low diffusion barrier and fast migration pathways, leading to superior conductivity.

### 3.1.3. Composition Alteration

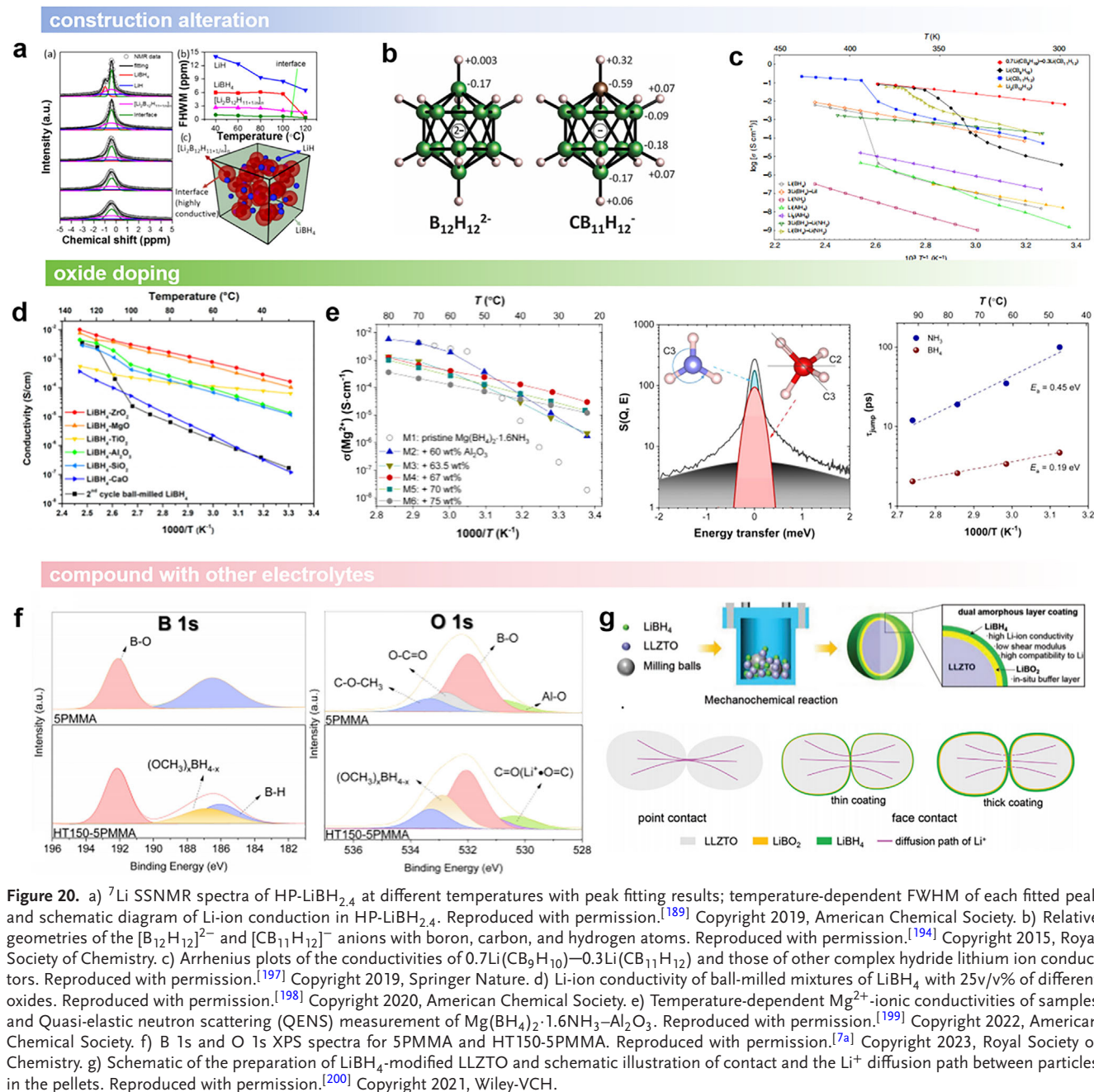
The structure of  $\text{Li}/\text{Mg}$ -based hydrides is a critical factor determining their ionic conductivity. Converting  $\text{LiBH}_4$  into a structure that facilitates  $\text{Li}^+$  migration through chemical reactions is an effective means of enhancing its conductivity. Previous studies have shown that alkali metal borane salts contain highly mobile alkali metal cations (i.e.,  $\text{Li}^+$ ,  $\text{Na}^+$ ) and complex anionic species (i.e.,  $\text{BH}_4^-$ ,  $\text{B}_{10}\text{H}_{10}^{2-}$ ,  $\text{B}_{12}\text{H}_{12}^{2-}$ ). Various structural phase transitions occur in these materials, increasing atomic disorder in the lattice at elevated temperatures and creating vacancies, which in turn enhance both cation and anion mobility.<sup>[191]</sup> For instance, in situ testing of  $\text{Li}_2\text{B}_{12}\text{H}_{12}$  revealed a first-order phase transition at  $355^\circ\text{C}$ , where thermally induced disorder in B, H, and Li

results in a disordered  $\text{Li}^+$  sublattice, indicating that this material could potentially serve as a superionic conductor.<sup>[192]</sup> Hence, Teprovich et al. synthesized  $\text{Li}_2\text{B}_{12}\text{H}_{12}$  by reacting  $\text{LiBH}_4$  with decaborane at high temperatures.<sup>[193]</sup> This material exhibits a  $\text{Li}^+$  conductivity of up to  $0.31 \text{ mS cm}^{-1}$  at room temperature, with an activation energy for ionic conduction of only  $0.34 \text{ eV}$ . This phenomenon could be attributed to the crystal structure of  $\text{Li}_2\text{B}_{12}\text{H}_{12}$ , which features a 3D framework where  $\text{Li}^+$  is surrounded by four  $[\text{B}_{12}\text{H}_{12}]^{2-}$  tetrahedra. During migration,  $\text{Li}^+$  shifts from the central position to a tetrahedral site at a distance of  $1.82 \text{ \AA}$ , where it is relatively weakly bound within the  $[\text{B}_{12}\text{H}_{12}]^{2-}$  ion cage. This weak binding allows  $\text{Li}^+$  to move relatively freely within the lattice, providing easy pathways for ionic conduction and facilitating rapid migration of  $\text{Li}^+$  through low-energy barriers within the structure. Inspired by this result, Zheng et al. successfully synthesized  $\text{Li}-\text{B}-\text{H}$  complexes through the partial dehydrogenation of  $\text{LiBH}_4$  under a pressure of  $0.3 \text{ MPa H}_2$ .<sup>[174a]</sup> This process resulted in in situ formation of the partially dehydrogenated products  $\text{LiBH}_4$ ,  $\text{LiH}$ , and  $[\text{Li}_2\text{B}_{12}\text{H}_{11+1/n}]_n$ . In addition to the formation of the highly conductive  $[\text{Li}_2\text{B}_{12}\text{H}_{11+1/n}]_n$ , the interfacial layer between  $[\text{Li}_2\text{B}_{12}\text{H}_{11+1/n}]_n$  and  $\text{LiBH}_4$  also exhibited superionic conductivity, providing interconnected pathways for rapid  $\text{Li}^+$  conduction and significantly enhancing conductivity (Figure 20a). Furthermore, due to improved contact, the in situ formed  $[\text{Li}_2\text{B}_{12}\text{H}_{11+1/n}]_n/\text{LiBH}_4$  interfacial layer after  $\text{LiBH}_4$  dehydrogenation demonstrated superior ionic conductivity compared to that achieved by ball milling. Ultimately, its ionic conductivity reached as high as  $2.7 \times 10^{-4} \text{ S cm}^{-1}$  at  $35 \text{ }^\circ\text{C}$ .

Although  $\text{Li}_2\text{B}_{12}\text{H}_{12}$  exhibits a higher intrinsic ionic conductivity than  $\text{LiBH}_4$ , its phase transition temperature reaches as high as  $350 \text{ }^\circ\text{C}$ , indicating that further improvements are necessary for practical applications. In 2015, Tang et al. first proposed substituting a  $[\text{B}-\text{H}]$  vertex with an isoelectronic  $[\text{C}-\text{H}]$  group, successfully synthesizing  $\text{Li}(\text{CB}_{11}\text{H}_{12})$ , which has a cage-like structure similar to  $\text{Li}_2\text{B}_{12}\text{H}_{12}$  (Figure 20b).<sup>[194]</sup> In comparison to  $\text{Li}_2\text{B}_{12}\text{H}_{12}$ , the 1:1 ratio of cations to anions in  $\text{Li}(\text{CB}_{11}\text{H}_{12})$  and  $\text{NaCB}_{11}\text{H}_{12}$  is halved, providing more available cation vacancies within each unit cell and reducing the obstruction to cation migration. Additionally, the  $(\text{CB}_{11}\text{H}_{12})^-$  anion exhibits stronger directional mobility. When cations attempt to pass through  $(\text{CB}_{11}\text{H}_{12})^-$ , the anion can further assist in ion transport, enhancing the overall ionic conductivity of the material.<sup>[195]</sup> Finally,  $\text{Li}(\text{CB}_{11}\text{H}_{12})$  has a larger lattice constant, providing more space for cation transport. In summary,  $\text{Li}(\text{CB}_{11}\text{H}_{12})$  exhibits a faster ion migration rate, with its ionic conductivity reaching  $0.15 \text{ S cm}^{-1}$  after the complete phase transition at  $130 \text{ }^\circ\text{C}$ . In 2016, this group synthesized  $\text{Li}(\text{CB}_9\text{H}_{10})$ , which, compared to  $\text{Li}(\text{CB}_{11}\text{H}_{12})$ , exhibits a lower phase transition temperature and ionic conductivity ( $0.03 \text{ S cm}^{-1}$  at  $80 \text{ }^\circ\text{C}$ ), as well as a lower activation energy barrier ( $0.29 \text{ eV}$ ).<sup>[196]</sup> This is due to the reduced anionic charge in  $\text{Li}(\text{CB}_9\text{H}_{10})$  compared to  $\text{Li}(\text{CB}_{11}\text{H}_{12})$ , resulting in weaker cation–anion Coulomb interactions and a lower cation diffusion barrier, ultimately leading to higher ionic conductivity. In 2019, Kim et al. conducted further studies by grinding and mixing  $\text{Li}(\text{CB}_9\text{H}_{10})$  and  $\text{Li}(\text{CB}_{11}\text{H}_{12})$ .<sup>[197]</sup> Using  $(\text{CB}_{11}\text{H}_{12})^-$  to partially substitute  $(\text{CB}_9\text{H}_{10})^-$ , they stabilized the disordered high-temperature phase of  $\text{Li}(\text{CB}_9\text{H}_{10})$  and successfully synthesized the composite superionic conductor

$0.7\text{Li}(\text{CB}_9\text{H}_{10})-0.3\text{Li}(\text{CB}_{11}\text{H}_{12})$ , which exhibited a ionic conductivity of up to  $6.7 \text{ mS cm}^{-1}$  at  $25 \text{ }^\circ\text{C}$  (Figure 20c). The disordered high-temperature phase of  $\text{Li}(\text{CB}_9\text{H}_{10})$  has a low phase transition temperature at  $90 \text{ }^\circ\text{C}$  and high ionic conductivity of  $10^{-1} \text{ S cm}^{-1}$ , making it the primary phase for synthesizing the composite  $\text{Li}^+$  conductor solid electrolyte. Due to the similar geometry, size, and valence of  $(\text{CB}_{11}\text{H}_{12})^-$  and  $(\text{CB}_9\text{H}_{10})^-$ , mechanical ball milling allowed partial substitution of  $(\text{CB}_9\text{H}_{10})^-$  by  $(\text{CB}_{11}\text{H}_{12})^-$  to stabilize the high-temperature phase. A molar fraction of  $0.3(\text{CB}_{11}\text{H}_{12})^-$  was selected to ensure sufficient stabilization without forming impurity phases. The all-solid-state lithium–sulfur battery using  $0.7\text{Li}(\text{CB}_9\text{H}_{10})-0.3\text{Li}(\text{CB}_{11}\text{H}_{12})$  as a solid electrolyte exhibited a high energy density of  $2500 \text{ Wh kg}^{-1}$  at a high current density of  $5016 \text{ mA g}^{-1}$ .

Additionally, previous studies have shown that different two-phase composites exhibit heterogeneous dynamics, reflecting the presence of both slow and fast-diffusing lithium ions, which aligns with the redistribution of carriers in space-charge regions near the two-phase interface. The presence of an insulator can form a defective and highly conductive interfacial layer between the conductive and insulating phases. As mentioned above, creating interfaces by mixing with oxides is an effective strategy to enhance the ion conductivity of hydride electrolyte at room temperature. Therefore, Gelino et al. employed ball milling to combine  $\text{LiBH}_4$  with various oxides such as  $\text{SiO}_2$ ,  $\text{CaO}$ ,  $\text{MgO}$ ,  $\gamma\text{-Al}_2\text{O}_3$ ,  $\text{TiO}_2$ , and  $\text{ZrO}_2$ , and proposed general guidelines for improving the conductivity of  $\text{LiBH}_4$  using oxides (Figure 20d).<sup>[198]</sup> Their study revealed that a defective, highly conductive interfacial layer formed between the oxide and  $\text{LiBH}_4$ , and the extent of enhancement is influenced by the oxide particle size and porosity. Among the samples, those containing  $25 \text{ v/v\% ZrO}_2$  and  $\text{MgO}$  exhibited the highest conductivities, achieving  $0.26$  and  $0.18 \text{ mS cm}^{-1}$  at  $40 \text{ }^\circ\text{C}$ , respectively. Furthermore, ball milling with oxides could also be applied to enhance the ionic conductivity of  $\text{Mg}(\text{BH}_4)_2$ . Jensen's group combined  $\text{Mg}(\text{BH}_4)_2 \cdot x\text{NH}_3$  with nanosized  $\text{MgO}$  and  $\text{Al}_2\text{O}_3$  particles, using the nanoparticles to increase the amorphization degree of  $\text{Mg}(\text{BH}_4)_2$ , which results in a highly dynamic state for  $\text{Mg}^{2+}$ . As a result,  $\text{Mg}(\text{BH}_4)_2 \cdot 1.6\text{NH}_3 @ \text{MgO}$  and  $\text{Mg}(\text{BH}_4)_2 \cdot 1.6\text{NH}_3 @ \text{Al}_2\text{O}_3$  achieved Mg-ion conductivities of  $10^{-5}$  and  $2.5 \times 10^{-5} \text{ S cm}^{-1}$  at room temperature, respectively.<sup>[199]</sup> Based on these findings, building composites of  $\text{Li}/\text{Mg}$ -based hydrides with non-hydride materials is a widely used method to enhance the ionic conductivity of  $\text{LiBH}_4$  (Figure 20e). Wei et al. mixed the PMMA with  $\text{LiBH}_4$ , leveraging the interaction between the  $-\text{OCH}_3$  groups in PMMA and the  $\text{BH}_4^-$  anions in  $\text{LiBH}_4$ .<sup>[7a]</sup> Through an in situ melting reaction, new B–O coordination bonds  $(\text{OCH}_3)_x\text{BH}_{4-x}$  were formed on the surface of the electrolyte particles (Figure 20f). The final product, HT150-5PMMA- $\text{LiBH}_4$ , achieved a conductivity of  $0.4 \text{ mS cm}^{-1}$  at room temperature. Theoretical calculations showed that after reacting with PMMA,  $\text{BH}_4^-$  is less likely to experience electron leakage, with high concentrations of covalent bonding electrons localized on the anions. This strong localization thermodynamically halts electron exchange during anion oxidation and kinetically prevents electron percolation on the surface of the electrolyte particles. As a result, the material exhibits very low electronic conductivity, effectively suppressing the formation and growth of lithium dendrites, with a critical current density of  $21.65 \text{ mA cm}^{-2}$  at  $25 \text{ }^\circ\text{C}$ . Moreover, compositing  $\text{LiBH}_4$



with other types of solid-state electrolytes are also explored for enhancing its ionic conductivity. Gao et al. used a ball-milling technique to synthesize a composite of LiBH<sub>4</sub> with garnet-type oxide electrolyte Li<sub>6.4</sub>La<sub>3</sub>Zr<sub>1.4</sub>Ta<sub>0.6</sub>O<sub>12</sub> (LLZTO), obtaining a bilayer-coated LLZTO electrolyte material with a LiBO<sub>2</sub> inner shell and a LiBH<sub>4</sub> outer shell (Figure 20g).<sup>[200]</sup> The amorphous coating of LiBH<sub>4</sub> significantly enhanced particle-to-particle contact, functioning as a filler, binder, and bridge and hence the open porosity of LiBH<sub>4</sub>-modified LLZTO was less than half of that of pristine LLZTO, delivering an ionic conductivity of 0.08 mS·cm<sup>-1</sup> at 30 °C. To further fill the gaps between LLZTO particles and effectively improve the density of composites, Lv et al. applied a liquid-

phase method, using a THF solution of Li<sub>4</sub>(BH<sub>4</sub>)<sub>3</sub>I to uniformly coat LLZTO with a composite hydride layer.<sup>[201]</sup> The conductivity at 30 °C reached 0.06 mS·cm<sup>-1</sup>. Simultaneously, the hydride coating significantly reduced the electronic conductivity of the composite electrolyte and formed a compatible interface with lithium metal, enhancing the electrochemical stability of the battery.

### 3.1.4. Summary and Outlook

Li/Mg-based borohydrides demonstrate significant potential in the field of SEs. The ionic conductivity and electrochemical

stability of  $\text{LiBH}_4$  and  $\text{Mg}(\text{BH}_4)_2$  have been notably enhanced through various modification strategies, including cation/anion substitution, composition alteration, and nanoconfinement techniques. These methods induce lattice expansion and structural relaxation, thereby lowering the energy barrier for ion migration and further optimizing ion transport pathways, which effectively improves the migration performance of Li and Mg ions. Additionally, composite strategies that incorporate hydride electrolytes with other compounds facilitate the creation of more flexible ion migration paths. Collectively, these approaches not only enhance ionic conductivity but also lay a solid foundation for the development of high-performance solid-state battery materials, thereby showcasing excellent performance across a wider range of applications.

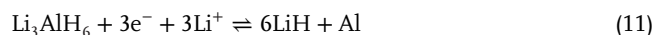
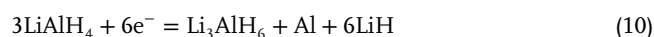
Looking ahead, the development of  $\text{BH}_4^-$ -based SEs is likely to focus on optimizing structural characteristics at both macro and nanoscale levels. This includes fine-tuning pore sizes in nanoconfined systems and designing new lattice frameworks to enable faster ion migration. Additionally, advancing composite strategies by further integrating hydride electrolytes with other SEs may improve interfacial stability and enhance compatibility with lithium metal anodes. Furthermore, exploring novel doping techniques, including the introduction of gas molecules, can promote defect formation and modify charge distribution, thereby enhancing ionic conductivity. These research advancements are expected to propel the application of  $\text{LiBH}_4$  and  $\text{Mg}(\text{BH}_4)_2$  based materials in high-performance SSBs, improving their safety, energy density, and cycle life, thus laying the foundation for the next generation of solid-state energy storage technologies.

### 3.2. Anode Materials of LIBs

In 2008, Oumellal first introduced  $\text{MgH}_2$  as a metal hydride electrode in LIBs.<sup>[202]</sup> The research showed that, relative to  $\text{Li}^+/\text{Li}^0$ ,  $\text{MgH}_2$  electrodes demonstrated a high reversible capacity of 1480  $\text{mAh g}^{-1}$  at an average voltage of  $\sim 0.5$  V, making it suitable for use as an anode material. Additionally, it exhibited minimal polarization of only 250 mV as a conversion electrode. The electrochemical reaction resulted in the formation of a Mg-containing composite material in the LiH matrix, which was reconverted to  $\text{MgH}_2$  during charging. This reaction is not exclusive to  $\text{MgH}_2$ , as other metals or intermetallic hydrides (e.g.,  $\text{NaAlH}_4$ ,  $\text{LiAlH}_4$ ,  $\text{Mg}_2\text{NiH}_4$  etc.) also exhibit similar reactivity with Li. Notably, the reaction produced nanoscale Mg and  $\text{MgH}_2$ , which displayed enhanced hydrogen absorption/desorption kinetics. However, due to the conversion reaction ( $\text{MgH}_2$  [ $61.59 \text{ \AA}^3$ ]  $\rightarrow$  Mg [ $46.46 \text{ \AA}^3$ ] +  $2\text{LiH}$  [ $2 \times 33.3 \text{ \AA}^3$ ]) shown in **Figure 21a**,  $\text{MgH}_2$  undergoes a significant volume expansion of  $\sim 85\%$  during lithium storage, leading to severe electron loss within the electrode. Furthermore, degradation of the electrode and particle agglomeration during the conversion process caused rapid capacity fading, leaving only 520  $\text{mAh g}^{-1}$  of reversible capacity after 50 cycles. Nevertheless, the study demonstrated the potential of  $\text{MgH}_2$  as an anode material for LIBs. In addition to  $\text{MgH}_2$ ,  $\text{LiAlH}_4$ , as a class of light-weight complex hydrides, also exhibit significant potential as conversion-type electrodes for lithium storage. For example, both  $\text{LiAlH}_4$  and  $\text{Li}_3\text{AlH}_6$  can exchange up to three electrons

when fully reduced to LiH and Al, with theoretical capacities of 2119 and 1493  $\text{mAh g}^{-1}$ , respectively, owing to their extremely low molecular weights. In 2015, Silvestri et al. systematically explored the potential of lithium alanates ( $\text{LiAlH}_4$  and  $\text{Li}_3\text{AlH}_6$ ) as negative electrodes in LIBs.<sup>[203]</sup> By using mechanical ball milling to process  $\text{LiAlH}_4$  and  $\text{Li}_3\text{AlH}_6$ , they investigated the effects of different milling times on their electrochemical performance. After nanostructuring by ball milling,  $\text{LiAlH}_4$  and  $\text{Li}_3\text{AlH}_6$  delivered discharge specific capacities of 1180 and 900  $\text{mAh g}^{-1}$ , respectively. The experimental work was further supported by theoretical calculations to study the structural changes during the electrochemical reactions.

Additionally, Teprovich and Zhang also investigated the conversion mechanisms of these hydrides with lithium (Figure 21c).<sup>[193]</sup> They summarized the lithium storage reaction of  $\text{LiAlH}_4$  into three stages:



It is important to note that the conversion of  $\text{LiAlH}_4$  to  $\text{Li}_3\text{AlH}_6$  is irreversible due to the thermodynamic instability of  $\text{LiAlH}_4$ .  $\text{Li}_3\text{AlH}_6$ , however, serves as an intermediate product in the lithiation process of  $\text{LiAlH}_4$  and can reversibly store three lithium ions via a conversion reaction. Despite their high initial capacity, these materials suffer from reaction irreversibility, interface reactions, and volume expansion. For example,  $\text{LiAlH}_4$  reacts strongly with carbonate-based electrolytes, forming a complex surface passivation layer that negatively impacts the electrochemical performance of the electrodes. As cycling progresses, the capacity of these materials decreases significantly. Therefore, various strategies have been developed to improve the electrochemical performance of Li/Mg-based hydrides. In this section, we describe the two main approaches, including catalysis and nanostructuring. This section focuses on two typical improvement strategies for  $\text{MgH}_2$  and  $\text{LiAlH}_4$  electrodes, including catalysis and nanostructuring. **Tables 4** and **5** summarize the electrochemical performance of the respective electrode in liquid batteries and all-solid-state batteries.

#### 3.2.1. Catalysis

Incorporating catalysts into  $\text{MgH}_2$  and  $\text{LiAlH}_4$  through mechanical mixing is a commonly used modification method to enhance their electrochemical performance of the material. Among them,  $\text{TiH}_2$ , with its high conductivity and rapid hydrogen transport properties, serves as an ideal catalyst choice.

In 2015, Huang et al. introduced  $\text{TiH}_2$  into  $\text{MgH}_2$  electrodes through mechanical ball milling.<sup>[204]</sup>  $\text{TiH}_2$  exhibits high electronic conductivity and rapid hydrogen diffusion, which significantly improved the electrochemical performance of the electrode. Compared to electrodes based on  $\text{MgH}_2$  or  $\text{TiH}_2$  alone, this composite material demonstrated superior performance in terms of reversible capacity and polarization stability. At a current density of 0.1C, the composite electrode achieved a reversible capacity of 1450  $\text{mAh g}^{-1}$ , and it retained higher capacity and lower

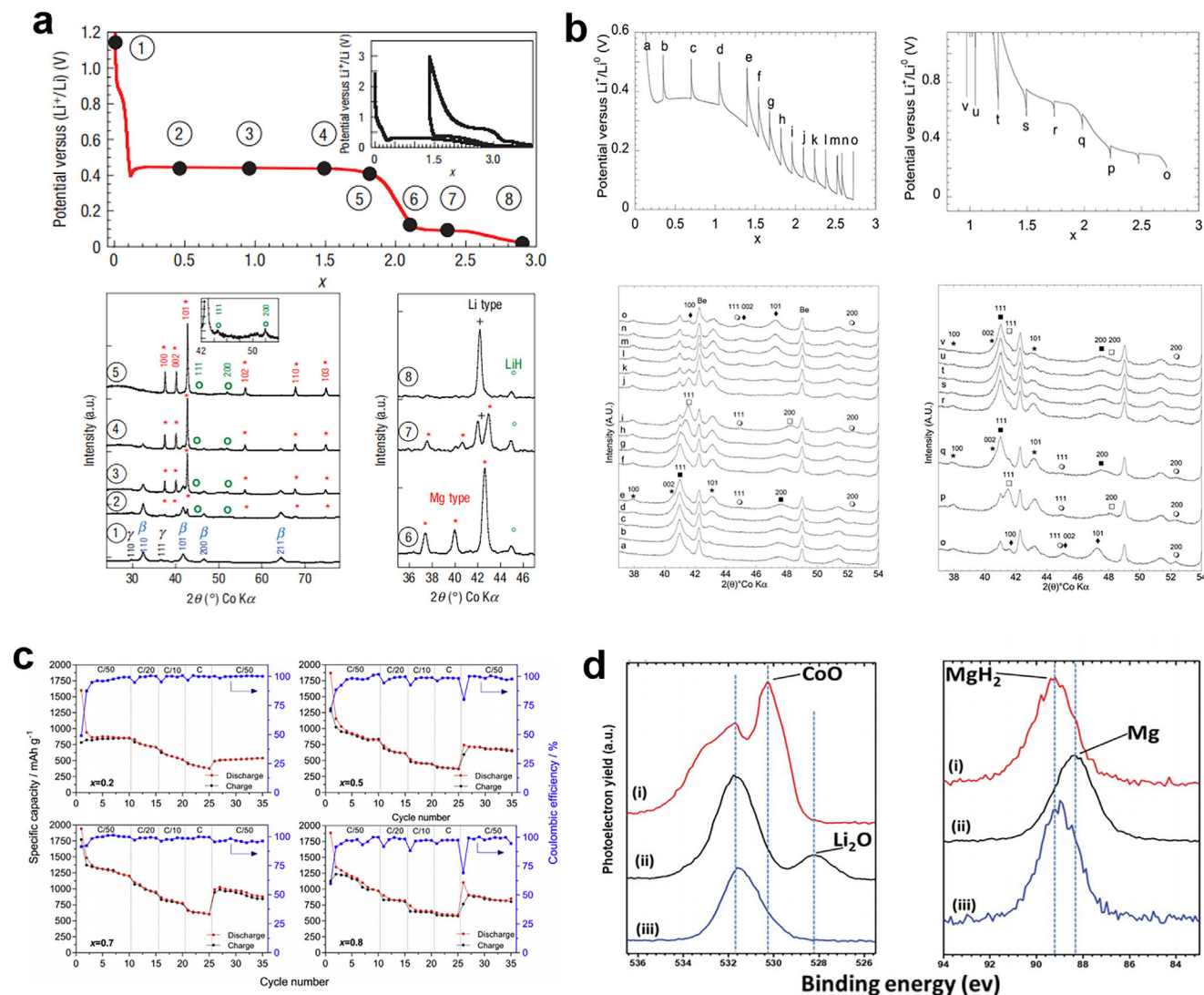
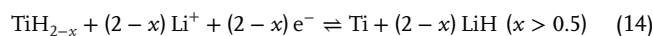
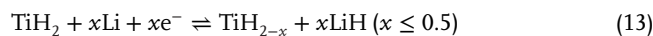


**Figure 21.** a) Voltage profile and XRD patterns of MgH<sub>2</sub> electrode at various stages of the conversion reaction. Reproduced with permission.<sup>[202]</sup> Copyright 2018, Elsevier. b) 7MgH<sub>2</sub>-0.3TiH<sub>2</sub>/Li cell GITT curves recorded during discharge and charge and corresponding in situ XRD patterns. Reproduced with permission.<sup>[204]</sup> Copyright 2015, Royal Society of Chemistry. c) Galvanostatic cycling performance of xMgH<sub>2</sub> + (1-x)TiH<sub>2</sub> composites at various kinetic regimes between 1C and C/50. Reproduced with permission.<sup>[209]</sup> Copyright 2018, Elsevier. d) O 1s and Mg 2s photoelectron spectra regions of i) the starting CoO/MgH<sub>2</sub> powders, ii) the 75MgH<sub>2</sub>-25CoO-based cell discharged at 0.3 V, and iii) charged at 1 V. Reproduced with permission.<sup>[211]</sup> Copyright 2018, Royal Society of Chemistry.

polarization at increasing current densities. This performance enhancement is attributed to the formation of a uniformly coupled nanostructure of Mg and Ti-containing hydrides during ball milling. Furthermore, the presence of TiH<sub>2</sub> provides rapid conduction pathways for Li<sup>+</sup> and H, effectively mitigating Mg particle coarsening during cycling and reducing volume changes in the MgH<sub>2</sub> electrode.<sup>[205]</sup>

Further analysis revealed that TiH<sub>2</sub> not only improves the kinetic performance of MgH<sub>2</sub>, but also facilitates the reversible lithium storage process of TiH<sub>2</sub>. Through in situ XRD analysis, researchers explored the lithium storage process in the composite electrode and identified three main stages: i) lithium storage transformation of MgH<sub>2</sub>, ii) conversion of TiH<sub>2</sub> to a TiH<sub>2-x</sub> solid solution, and iii) further transformation of TiH<sub>2-x</sub> into

Ti. This reversible behavior of TiH<sub>2</sub> provides additional lithium storage capacity for the composite electrode. The nanoscale synergistic effect between these two hydrides significantly enhances the overall electrochemical performance of the electrode (Figure 21b).



Nevertheless, the liquid organic electrolyte used in this study poses inherent flammability risks, potentially leading to safety

**Table 4.** Performance comparison of hydride-based electrodes in liquid battery.

Material	Current density [mA g <sup>-1</sup> ]	Cycle	Capacity [mAh g <sup>-1</sup> ]	Refs.
Nano MgH <sub>2</sub> -GR	100	100	946	[209]
Nanosized MgH <sub>2</sub> particles (BM50MgH <sub>2</sub> @HSAG-500)	2000	20	500	[213]
MH@HyC	2000	1000	554	[174a]
MgH <sub>2</sub> -TiO <sub>2</sub> -EG 20h	100	100	305.5	[275]
MgH <sub>2</sub> -Ti <sub>3</sub> C <sub>2</sub> MXene	2000	1000	1092.9	[282]
MgH <sub>2</sub>	/	1	1480	[202]
G/MgH <sub>2</sub> @PTh.	2000	500	866	[209]
Si-MgH <sub>2</sub>	500	200	3228	[267]
MHG@MBH	200	380	1651	[283]
Thin film MgH <sub>2</sub>	40	5	200	[181a]
LiAlH <sub>4</sub>	/	1	2119	[203]
Li <sub>3</sub> AlH <sub>6</sub>	/	1	1493	[203]

hazards from short circuits during operation.<sup>[206]</sup> Additionally, during the lithiation/delithiation process, side reactions may occur at the electrolyte–electrode interface in liquid systems, resulting in rapid capacity decay.<sup>[207]</sup> Therefore, future research focuses on developing SEs with enhanced safety and electrochemical stability to replace conventional liquid electrolytes.<sup>[208]</sup> Dao et al. investigated the application of MgH<sub>2</sub>-TiH<sub>2</sub> composites in all-solid-state lithium-ion batteries (ASSLIBs), selecting LiBH<sub>4</sub> as the solid electrolyte due to its excellent mechanical properties, strain-induced diffusion activation energy, and ability to form stable composites with MgH<sub>2</sub> anodes.<sup>[209]</sup> The research team conducted electrochemical testing on  $x\text{MgH}_2 + (1-x)\text{TiH}_2$  electrodes with various ratios and performed detailed analysis using cyclic voltammetry (CV), identifying distinct electrochemical behaviors across different lithiation and delithiation stages and associating each stage with corresponding reactions of TiH<sub>2</sub> and MgH<sub>2</sub>. Through electrochemical impedance spectroscopy, the researchers assessed the evolution of cell resistance across various electrochemical steps, further elucidating the causes of

**Table 5.** Performance comparison of hydride-based electrodes solid-state battery.

Material	Current density [mA g <sup>-1</sup> ]	Cycle	Capacity [mAh g <sup>-1</sup> ]	Refs.
MgH <sub>2</sub> @Nb <sub>2</sub> O <sub>5</sub>	200	50	140	[284]
0.7MgH <sub>2</sub> + 0.3TiH <sub>2</sub>	40	10	1050	[209]
MgH <sub>2</sub> -Nd <sub>2</sub> O <sub>5</sub>	800	50	924	[285]
MgH <sub>2</sub> (25 MPa stacking pressure)	836	200	1300	[266]
Nd <sub>4</sub> Mg <sub>80</sub> Ni <sub>8</sub> H <sub>x</sub>	2038	100	997	[217]
MgH <sub>2</sub> /Gr	400	200	597	[218]
75MgH <sub>2</sub> -25CoO	100	5	~800	[211]
MHG@MBH	2000	350	800	[218]
MgH <sub>2</sub> -TiH <sub>2</sub> -AB or MgH <sub>2</sub> -TiH <sub>2</sub> -VGCF	/	1	1100	[286]
LiAlH <sub>4</sub> -Al	1000	100	1429	[180a]

electrode degradation induced by the contact loss within the electrode intensified with continuous cycling, resulting in increased resistance. Compared with liquid electrolyte cells, the same electrode materials in solid-state cells exhibited higher reversibility and lower polarization, attributed primarily to the fact that the electrochemical performance of electrode materials depends not only on nanostructures but also on charge and mass transport. Furthermore, high-temperature of 120 °C used in SSBs promotes faster electron and ion transport, facilitating electrochemical reactions. Unlike lithium storage mechanisms in liquid-state cells, the formation of a solid electrolyte interphase during the first discharge process in solid-state cells reduces interfacial resistance between the electrode and electrolyte, thereby improving cycling stability. During charging, all samples exhibited a minor plateau at 0.7 V, suggesting a possible reversible reaction between MgH<sub>2</sub> and LiBH<sub>4</sub>, which further contributes to reversible capacity. Additionally, at a 1C rate, the capacity of all composites remained at ~45% (Figure 21c), indicating that  $x\text{MgH}_2 + (1-x)\text{TiH}_2$  composites with SEs demonstrate greater reversibility and that the solid electrolyte configuration significantly mitigates degradation observed during initial galvanostatic cycles. This is especially critical for TiH<sub>2</sub>-rich electrodes, as the excellent mechanical properties of LiBH<sub>4</sub> can accommodate volume changes, while the high operating temperature of solid-state cells enhances mass transport. In summary, SSBs offer significant advantages in terms of safety, energy density, and cycle stability, exhibiting low polarization and superior interfacial stability, making them a highly promising solution in future battery technology.

In addition to hydrides, the incorporation of oxides has been shown to effectively enhance the kinetic performance of MgH<sub>2</sub>. Similarly, using LiBH<sub>4</sub> as a solid electrolyte, Ichikawa and Kojima's group introduced 1 mol% Nd<sub>2</sub>O<sub>5</sub> into MgH<sub>2</sub>, facilitating rapid hydrogen diffusion, which improved reaction kinetics, reversibility, and initial coulombic efficiency, while also reducing reaction polarization.<sup>[210]</sup> Furthermore, Kharbachi et al. incorporated 25 mol% conversion-type anode material CoO with MgH<sub>2</sub>.<sup>[211]</sup> Electrochemical testing revealed that, in contrast to the single electrochemical plateau around 0.5 V for MgH<sub>2</sub> alone, the MgH<sub>2</sub>-CoO composite electrode exhibited electrochemical plateaus at both 0.89 and 0.5 V, representing the reversible lithium storage reactions of CoO and MgH<sub>2</sub>, respectively. As the cycle continues, the charge and discharge platform of CoO gradually weakens, which may be related to the nanocrystalline nature of the CoO, as the CoO can be reversibly cycled at a constant current density to form nanoscale particles in the 1–2 nm range.<sup>[212]</sup> Such nanoscale interactions make Li<sup>+</sup> and electrons readily available in close proximity at the MgH<sub>2</sub>/Mg surface via highly dispersed CoO/Co nanoparticles, thereby overcoming the issues of electronic conductivity and particle aggregation (Figure 21d). Additionally, the presence of CoO shortens diffusion pathways and reduces electrode polarization, which are believed to be key factors contributing to the enhanced electrochemical performance.

### 3.2.2. Nanostructuring

Nanosizing is a common method used to enhance the energy storage performance of materials. Nanostructured materials possess a larger specific surface area, which provides a greater

chemical reaction area that facilitates more complete reactions and accelerates Faradaic processes. The smaller distance between particles allows for faster Li<sup>+</sup> diffusion and charge transport, thereby improving the overall electrochemical performance of the material.

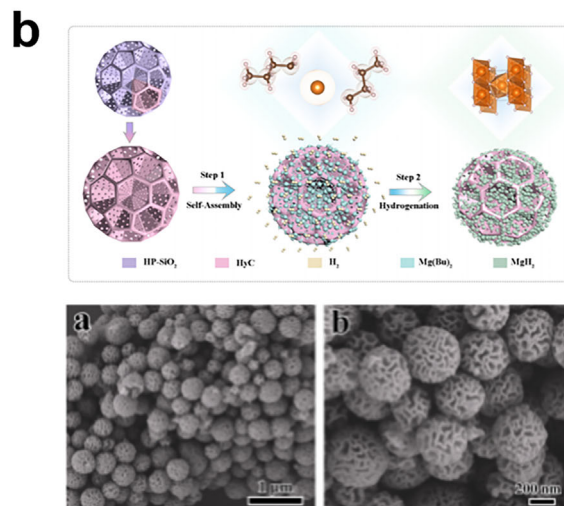
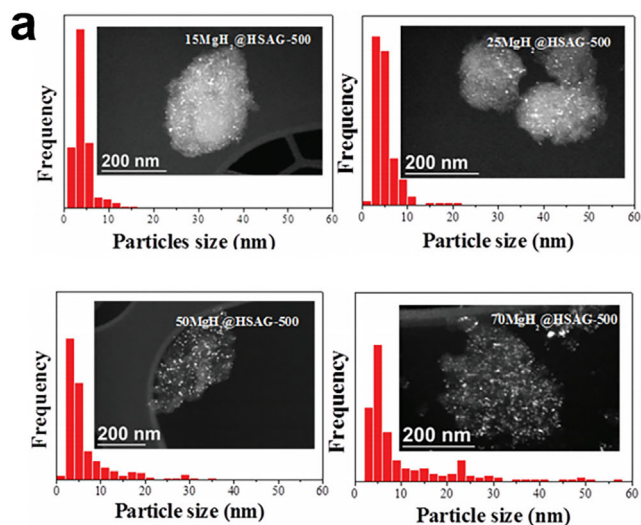
Oumellal et al. adopted a bottom-up preparation method, wherein a MgBu<sub>2</sub> solution was used to impregnate a porous carbon host, followed by heating under a hydrogen atmosphere.<sup>[213]</sup> In MgH<sub>2</sub> samples with varying loadings, the majority of nanoparticles have diameters below 10 nm, with an average particle size ranging from 4 to 5.5 nm (Figure 22a). The particle size of MgH<sub>2</sub> nanoparticle could be facilely adjusted by controlling the loading of Mg, reaching up to a maximum metal concentration of 50 wt%, at which MgH<sub>2</sub> nanoparticles fully occupy the available carbon scaffold pores. On one hand, the nanoscale size of MgH<sub>2</sub> particles and the high porosity of the carbon scaffold increase the electrode–electrolyte contact area and reduce internal diffusion paths (such as the MgH<sub>2</sub>/electrolyte interface during discharge and Mg/LiH interface during charge), enabling fast diffusion of hydrogen and lithium ions.<sup>[214]</sup> Additionally, the developed porous structure of the carbon scaffold could alleviate the MgH<sub>2</sub> volume expansion and, subsequently, hinder the loss of electronic percolation due to repeated volume changes during cycling. Furthermore, the researchers suggest that mechanical milling in an Ar atmosphere could enhance the contact between MgH<sub>2</sub> and the carbon host, thereby improving electrode cycle life. Consequently, the overall electrochemical performance of MgH<sub>2</sub> is significantly improved, retaining a capacity of ~500 mAh g<sup>-1</sup> after 20 cycles at a current density of 2 A g<sup>-1</sup>. However, using this method, the initial capacity decline remains rapid, particularly during the second cycle, where the capacity quickly decreases to 1000 mAh g<sup>-1</sup>. This decline could be attributed to the loss of conductivity and changes in surface morphology during cycling, as a small portion of unconfined pores persists within the composite, with some MgH<sub>2</sub> nanoparticles deposited on the outer surface of the carbon scaffold.<sup>[215]</sup>

Subsequently, Yu's group optimized this process by using hierarchical porous silica spheres as a template to synthesize hierarchical porous carbon (HyC) in a flower-like morphology (Figure 22b).<sup>[216]</sup> They then in situ loaded nano-MgH<sub>2</sub> onto this substrate using MgBu<sub>2</sub> as the precursor. Compared to conventional porous carbon, HyC exhibits a higher specific surface area and a distinct mesoporous structure. This 3D layered porous architecture not only provides sufficient electrochemical active sites but also enhances electronic conductivity and facilitates rapid electron/lithium ion transfer channels, alleviating aggregation and volume accommodation effects during cycling. As a result, the MgH<sub>2</sub>@HyC composite can deliver a high reversible capacity of 554 mAh g<sup>-1</sup> after 1000 cycles at a high current rate of 2 A g<sup>-1</sup>. Although the method described above could alleviate the issue of volume expansion of MgH<sub>2</sub> during cycling in liquid electrolytes to some extent, as mentioned in the previous section, the electrode exhibits inherent limitations when applied in liquid electrolyte-based batteries. Consequently, researchers have also applied the nanostructuring strategy to ASSLIBs, using LiBH<sub>4</sub> as the solid electrolyte. However, the nanostructured MgH<sub>2</sub> anode still struggles with volume expansion during cycling, while the confinement effect of porous carbon on MgH<sub>2</sub> particles remains limited, leading to unresolved capacity decay.

In order to solve this problem, Gao et al. report the fabrication of space-confined MgH<sub>2</sub> and Mg<sub>2</sub>NiH<sub>4</sub> by the uniformly distributed Nd<sub>2</sub>H<sub>5</sub> frameworks with high Li-ion and electronic conductivity through the facile hydrogenation of single-phase Nd<sub>4</sub>Mg<sub>80</sub>Ni<sub>8</sub> alloys.<sup>[217]</sup> TEM and XRD results indicated that, MgH<sub>2</sub> and Mg<sub>2</sub>NiH<sub>4</sub> serve as active materials that participate in reversible lithium storage reactions, providing capacity during cycling, while Nd<sub>2</sub>H<sub>5</sub> remains stable throughout the charge/discharge process without reacting. The in situ-formed nanocrystals of MgH<sub>2</sub> and Mg<sub>2</sub>NiH<sub>4</sub> not only provide shorter diffusion paths for electrons and lithium ions, thereby enhancing the lithium storage kinetics of the metal hydrides, but also alleviate the stress induced by volume changes of the metal hydrides. Moreover, the homogeneous distribution of inactive Nd<sub>2</sub>H<sub>5</sub> acts as a stable scaffold, effectively mitigating the volume expansion of MgH<sub>2</sub> and Mg<sub>2</sub>NiH<sub>4</sub>, preventing phase separation during cycling, and maintaining electrode structural integrity (Figure 22c). Notably, theoretical and experimental results indicate that Nd<sub>2</sub>H<sub>5</sub> is an electronic conductor with a Li<sup>+</sup> diffusion barrier much lower than that of MgH<sub>2</sub> and Mg<sub>2</sub>NiH<sub>4</sub>. Its uniform distribution effectively promotes electron and Li<sup>+</sup> transport within MgH<sub>2</sub> and Mg<sub>2</sub>NiH<sub>4</sub>. Additionally, both Nd<sub>2</sub>H<sub>5</sub> and Mg<sub>2</sub>NiH<sub>4</sub> can catalytically weaken the Mg–H bonds in MgH<sub>2</sub>, thereby kinetically facilitating the reversible lithiation and delithiation of MgH<sub>2</sub>. The results show that the hydrogenated Nd<sub>4</sub>Mg<sub>80</sub>Ni<sub>8</sub> electrode retains a high reversible capacity of up to 997 mAh g<sup>-1</sup> after 100 cycles, even at a high current density of 2038 mAh g<sup>-1</sup>.

In 2023, Huang et al. employed a gas–solid reaction to in situ generate a nanostructured MgH<sub>2</sub> material uniformly supported on graphene, encapsulated by a thin shell of Mg(BH<sub>4</sub>)<sub>2</sub> (Figure 22d).<sup>[218]</sup> This core–shell structure facilitated the uniform construction of an ion-conductive pathway connected by conductive graphene on individual MgH<sub>2</sub> nanoparticles, significantly enhancing the electrochemical activity and ultra-stable reversibility of MgH<sub>2</sub> in ASSLIBs, with ionic conductivity improved by two orders of magnitude compared to electrodes without the Mg(BH<sub>4</sub>)<sub>2</sub> shell. The researchers observed that during cycling, Mg(BH<sub>4</sub>)<sub>2</sub> decomposes in situ to form a composite of Li<sub>2</sub>B<sub>6</sub>, LiBH<sub>4</sub>, and the nanostructured MgH<sub>2</sub> particles. Theoretical calculations demonstrate that Li<sub>2</sub>B<sub>6</sub> exhibits a strong capability for the absorption of LiBH<sub>4</sub>, which not only stabilizes the uniform coverage of LiBH<sub>4</sub> on the surface of MgH<sub>2</sub> but also maintains a consistent distribution of LiBH<sub>4</sub> around MgH<sub>2</sub> during repeated charge and discharge cycles, facilitating the rapid movement of Li<sup>+</sup> to the surface of MgH<sub>2</sub>. Furthermore, Li<sub>2</sub>B<sub>6</sub>, as an inactive substance with high ionic conductivity, along with the uniform distribution of graphene, provides structural support that mitigates the volume changes of MgH<sub>2</sub> nanoparticles, alleviating phase separation issues during cycling. This stabilization enhances the close contact between LiBH<sub>4</sub> and individual MgH<sub>2</sub> nanoparticles, improving lithium ion diffusion kinetics. As a result, the electrode retains a capacity of 800 mAh g<sup>-1</sup> after 350 cycles at a current density of 2 A g<sup>-1</sup>. In summary, the in situ construction of an inactive scaffold on the surface of MgH<sub>2</sub> effectively limits its volume change while enhancing the kinetic performance of the electrode, representing a viable approach to improve the overall electrochemical performance of MgH<sub>2</sub> electrodes.

## liquid battery



## all-solid-state battery

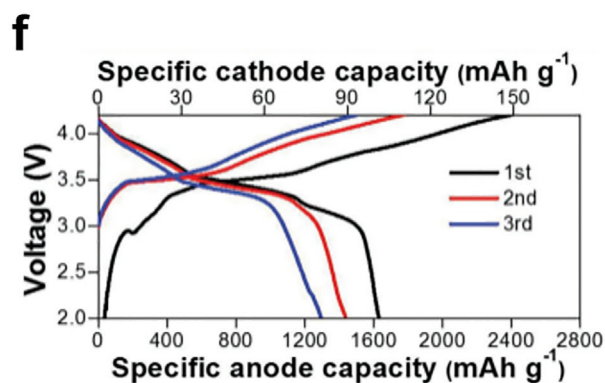
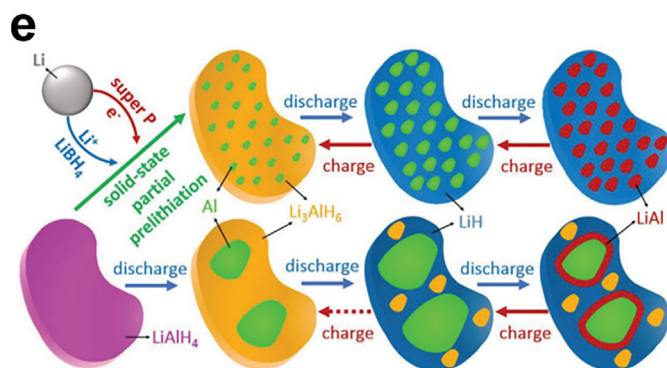
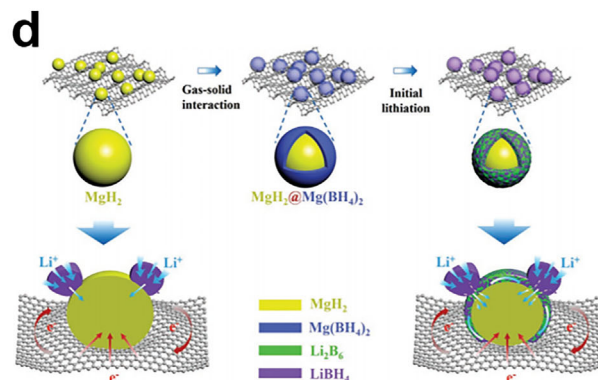
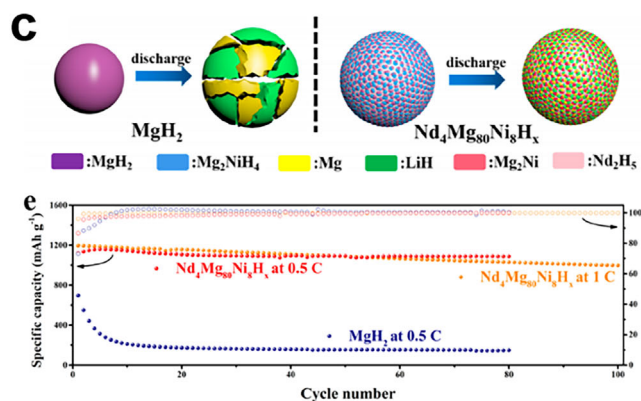


**Figure 22.** a) TEM images and the corresponding  $\text{MgH}_2$  nanoparticle size distribution histograms for the  $x\text{MgH}_2@$ HSAG-500 composites. Reproduced with permission.<sup>[213]</sup> Copyright 2014, Royal Society of Chemistry. b) Schematic illustration of the fabrication process of the MH@HyC framework. Reproduced with permission.<sup>[216]</sup> Copyright 2019, American Chemical Society. c) Schematic illustration of the charge and discharge process of  $\text{MgH}_2$  and  $\text{Nd}_4\text{Mg}_{80}\text{Ni}_8\text{H}_x$  electrodes and cycling performance of the  $\text{Nd}_4\text{Mg}_{80}\text{Ni}_8\text{H}_x$  electrode at 0.5 C and 1 C. Reproduced with permission.<sup>[217]</sup> Copyright 2022, American Chemical Society. d) Schematic diagram of the distribution and preparation process of MH@MBH nanoparticles on the surface of graphene. Reproduced with permission.<sup>[218]</sup> Copyright 2023, Wiley-VCH. e) Schematic illustration of the structural evolution of the SSPP Li-Al-H anode and  $\text{LiAlH}_4$  anode during cycling. f) The GCD profiles of the solid-state full cell. Reproduced with permission.<sup>[180a]</sup> Copyright 2020, Wiley-VCH.

In addition to  $\text{MgH}_2$ , the nanostructuring strategy also significantly enhances the performance of  $\text{LiAlH}_4$  electrodes, particularly in all-solid-state batteries. Pang et al. improved upon the issue of the irreversible conversion of  $\text{LiAlH}_4$  to  $\text{Li}_3\text{AlH}_6$ , caused by the thermodynamic instability of  $\text{LiAlH}_4$ , by proposing a solid-state pre-lithiation strategy to develop a novel coordinated hydride nanocomposite electrode material.<sup>[180a]</sup> By mixing  $\text{LiAlH}_4$ , Li,  $\text{LiBH}_4$ , and C, they enabled the in situ electrochemical reaction between  $\text{LiAlH}_4$  and Li in the solid phase, leveraging the ionic conductivity of  $\text{LiBH}_4$  and the electronic conductivity of carbon (Figure 22e). Through solid-state short-circuit pre-lithiation, nano-sized Al particles were generated and uniformly distributed in the amorphous  $\text{Li}_3\text{AlH}_6$  matrix, forming a  $\text{Li}_3\text{AlH}_6$ -Al composite material. This electrode, when combined with a  $\text{LiBH}_4$  solid electrolyte, was used to fabricate an all-solid-state battery, demonstrating excellent high capacity, high-rate capability, and cycling performance. The results showed that the  $\text{Li}_3\text{AlH}_6$ -Al composite material had nano-sized Al particles uniformly dispersed within the amorphous  $\text{Li}_3\text{AlH}_6$  matrix. In an all-solid-state half-cell, this material exhibited a reversible capacity of 2266  $\text{mAh g}^{-1}$  in the first cycle, with a coulombic efficiency of 88%. Moreover, when used as the anode in an all-solid-state battery with  $\text{LiCoO}_2$  as the cathode, the material demonstrated stable cycling performance (Figure 22f). This strategy can be applied not only to  $\text{Li}_3\text{AlH}_6$ -Al composite materials but also to other lithium-deficient electrode materials, effectively improving their overall performance.

### 3.2.3. Summary and Outlook

In conclusion,  $\text{MgH}_2$  and  $\text{LiAlH}_4$  exhibits significant potential as an anode material for LIBs, with various promising modification strategies identified for future research. The nanosizing of  $\text{MgH}_2$  represents a pivotal approach to enhance its electrochemical performance by increasing the specific surface area and improving Li ion diffusion rates. Furthermore, the incorporation of catalysts, such as  $\text{TiH}_2$  and  $\text{Nd}_2\text{O}_3$ , could enhance the reaction kinetics of  $\text{MgH}_2$  and improve cycling stability by promoting hydrogen transportation. Therefore, it is expected that the design of advanced structures, such as core-shell configurations composed of the encapsulation of  $\text{MgH}_2$  nanoparticles with functional shell materials with high Li ion and electronic conductivity could not only alleviate volume changes occurring during charge-discharge cycles but also enhance the kinetic performance, further promoting electron and ion transport. Unfortunately, owing to the high reactivity of Li/Mg-based hydrides, the techniques of producing their nanostructured anodes is limited to nanoconfinement, solvothermal, and ball milling, which limits the specific control over the nanostructures of Li/Mg-based hydrides.

Specifically, combining hydride anodes with SEs (e.g.,  $\text{LiBH}_4$ ) in all-solid-state batteries represents a promising avenue for increasing energy density and enhancing safety of ASSLIBs, particularly through techniques such as hot pressing to create stable interfaces. Finally, exploring novel doping techniques, such as the introduction of transition metals and the development of new metal hydrides, could significantly broaden their application scope. By focusing on these modification strategies, it is antici-

pated that  $\text{MgH}_2$  and  $\text{LiAlH}_4$  will play a crucial role in advancing next-generation battery technologies, thereby improving the performance and sustainability of high-capacity energy storage solutions.

## 4. Market Availability

### 4.1. Hydrogen Storage

$\text{MgH}_2$  is one of the most promising metal hydrides for large-scale hydrogen storage due to its high hydrogen capacity (7.6 wt%) and material abundance. Compared to other hydrogen storage approaches, such as liquid hydrogen, high-pressure gas, ammonia, and liquid organic hydrogen carriers,  $\text{MgH}_2$  offers a unique combination of low-pressure operation, high safety, and good recyclability. Here, we use  $\text{MgH}_2$  as a representative case to demonstrate the development from production and pilot demonstration to practical application, focusing on its market availability and cost.

The industrialization of  $\text{MgH}_2$  began with McPhy Energy, which previously produced up to ~27 tons per year of  $\text{MgH}_2$ -based pellets using self-developed facilities.<sup>[219]</sup> In 2023, JOMILEMAN SA publicly introduced a solid-state hydrogen storage system based on  $\text{MgH}_2$  (Figure 23a). The production process starts with commercial magnesium particles that undergo initial hydrogenation at 360 °C and 2–4 MPa  $\text{H}_2$  to form  $\text{MgH}_2$  powder. This is followed by high-energy ball milling with catalytic additives (e.g., Ti, V) for 5–10 h to reduce particle size and introduce lattice defects. Expanded graphite is then added to enhance thermal conductivity, and the mixture is pressed into dense discs (~1 kg each), which are assembled into modular hydrogen storage units.<sup>[220]</sup>

In terms of demonstration projects, Ding et al. in collaboration with Hydrexia have deployed the world's first ton-scale  $\text{MgH}_2$ -based solid-state hydrogen storage and transportation trailer. The 40-foot container holds 14.4 tons of Mg-based material and achieves a hydrogen storage capacity of 1.03 tons (Figure 23b). After 1000 hydrogenation/dehydrogenation cycles, the material retains 92% of its initial capacity, whose cycling stability can be further improved using nanoconfinement strategies.<sup>[221]</sup> An industrial-scale production line has also been established with a capacity of 100 tons per year, and the current ex-factory price of  $\text{MgH}_2$  pellets is ~16 USD  $\text{kg}^{-1}$ . With scale-up, the cost is expected to decrease by 20–50%. To address energy and cost challenges, three key strategies have been proposed: optimizing tank structure and heat exchanger topology, recovering heat released during hydrogenation for reuse in dehydrogenation, and coupling with industrial processes to utilize available waste heat. Figure 23c illustrates a geometric design scheme for enhancing thermal conductivity in  $\text{MgH}_2$ -based hydrogen storage tanks.<sup>[222]</sup>

In practical applications, the high energy consumption associated with dehydrogenation is a major contributor to the overall cost of  $\text{MgH}_2$ -based hydrogen storage systems. However, this cost varies by country due to differences in energy structures and pricing. As shown in Figure 23d, four heating scenarios for dehydrogenation were compared. Generally, direct electric heating is not economical and natural gas heating tends to be more expensive, especially in countries with higher gas prices or carbon taxes. In contrast, factory waste heat, though not entirely

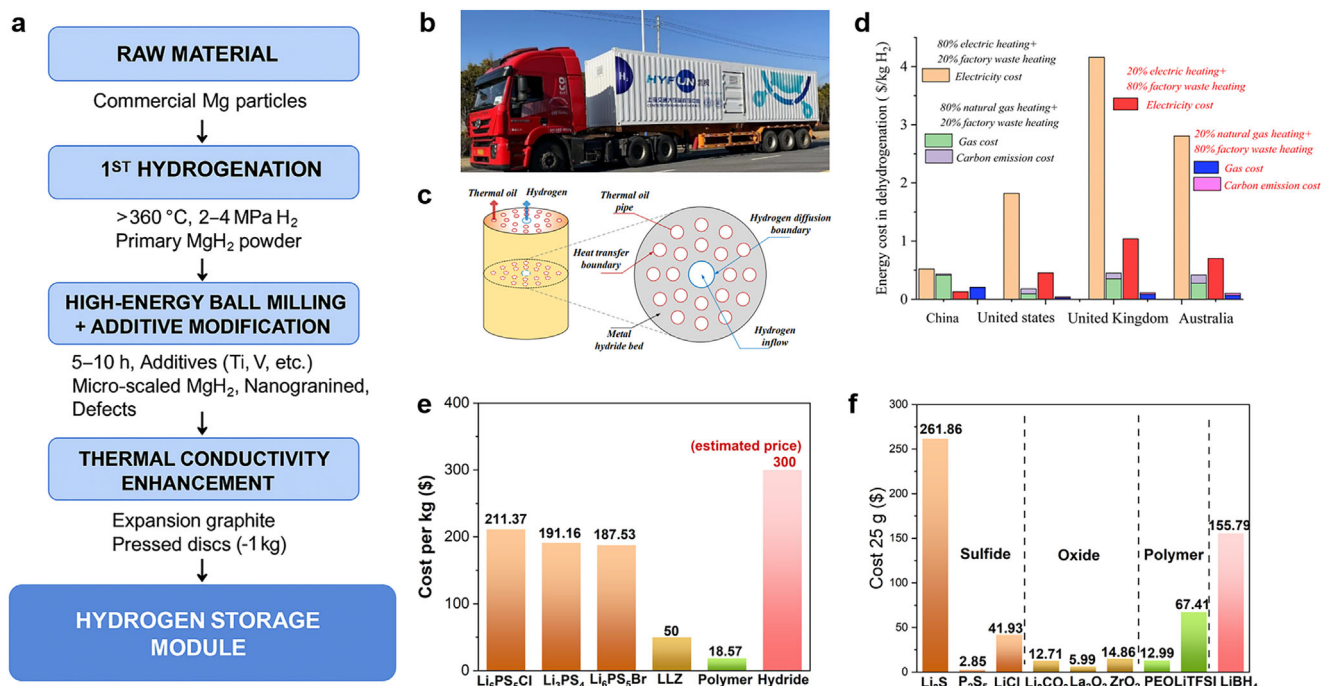


**Figure 23.** a) Schematic diagram of the production process for the MgH<sub>2</sub>-based solid-state hydrogen storage system. b) The first ton-scale Mg-based solid-state hydrogen storage and transportation trailer. c) Geometric design scheme of a magnesium hydride-based hydrogen storage tank to enhance thermal conductivity. d) Comparison of energy consumption costs for MgH<sub>2</sub> dehydrogenation under different heating strategies. Reproduced with permission.<sup>[222]</sup> Copyright 2024, Royal Society of Chemistry. e) Commercial cost comparison of solid-state electrolyte materials. f) Cost of precursor materials for various electrolytes based on data from Aladdin Reagent.

free, is available at very low cost and offers considerable potential for reducing energy expenses. Furthermore, as discussed in Section 2.4, researchers are exploring the use of renewable energy sources such as solar irradiation to drive MgH<sub>2</sub>-based hydrogen storage systems, though such technologies remain at a pre-commercial stage.

Additionally, Amica et al. evaluated the economic feasibility of using Mg(NH<sub>2</sub>)<sub>2</sub>-LiH-based hydride systems for mobile hydrogen storage in Argentina, where wind energy enables green hydrogen production at ~5 USD kg<sup>-1</sup>. Their analysis showed that competitive system costs (~5300–6700 USD for 4 kg H<sub>2</sub>) can be achieved only if the hydrides are synthesized from elemental Mg and Li. Nonetheless, the total cost remains more than twice that of high-pressure hydrogen storage systems.<sup>[223]</sup>

#### 4.2. Lithium Storage

In the field of energy storage, hydride materials are gaining significant attention due to their high energy density and lightweight characteristics. Typical examples include MgH<sub>2</sub> anodes and LiBH<sub>4</sub> electrolytes, which not only exhibit high theoretical capacity and good ionic conductivity but also offer potential advantages in terms of resource abundance and recyclability. However, these potential benefits have not yet been effectively translated into commercial applications, primarily due to inherent technical bottlenecks and high production costs associated with hydride materials.

Hydride materials are highly sensitive to moisture and oxygen, making them prone to decomposition reactions. For instance, when exposed to air, LiBH<sub>4</sub> rapidly absorbs moisture and decomposes into LiOH and B<sub>2</sub>O<sub>3</sub>, significantly reducing its ionic conductivity and compromising the structural integrity of the material. This moisture and oxygen sensitivity not only degrades electrochemical performance but also substantially increases production and storage costs. To prevent decomposition, the synthesis, storage, and application of hydride materials must be conducted under strictly controlled anhydrous and oxygen-free conditions, imposing higher requirements on equipment and production environment control, further escalating overall production costs.

Moreover, the synthesis of hydride materials is complex and energy-intensive. Common synthesis methods such as high-temperature hydrogenation, solvothermal methods, and mechanical alloying require stringent control over hydrogen purity, temperature, and pressure. These processes not only increase equipment and energy costs but also demand higher precision in reaction environment control. Compared to conventional carbon-based or silicon-based anode materials, the sensitivity of hydride materials to reaction atmospheres significantly increases production complexity, posing substantial challenges to large-scale production.

As a result, the market price of hydride materials remains relatively high. As shown in Figure 23e, the commercial price of MgH<sub>2</sub> is ~16 USD kg<sup>-1</sup>, significantly higher than the more mature silicon anode (14.29 USD kg<sup>-1</sup>) and graphite anode (5.00 USD kg<sup>-1</sup>).<sup>[224]</sup> Although the raw material cost of MgH<sub>2</sub> is relatively low, the high-temperature hydrogenation and

environmental control required during synthesis considerably drive up the overall cost. For  $\text{LiBH}_4$  electrolytes, there is currently no clear large-scale production price data. However, based on existing research estimates, the large-scale production cost of  $\text{LiBH}_4$  may reach 300–400 USD  $\text{kg}^{-1}$ , a price significantly higher than sulfide electrolytes (200 USD  $\text{kg}^{-1}$ ),<sup>[225]</sup> LLZ (50 USD  $\text{kg}^{-1}$ ),<sup>[226]</sup> and polymer electrolytes (18.57 USD  $\text{kg}^{-1}$ ). To further compare the costs of different electrolytes, we analyzed the prices of precursor materials based on data from Aladdin Reagent. The results show that while the cost of  $\text{LiBH}_4$  precursors is lower than that of sulfide electrolyte precursors such as  $\text{Li}_2\text{S}$ , it is still significantly higher than that of  $\text{La}_2\text{O}_3$  in LLZ and PEO in polymer electrolytes (Figure 23f). This indicates that even though  $\text{LiBH}_4$  may have certain cost advantages in raw materials, its complex synthesis process and strict environmental requirements still limit the potential for cost reduction, making it difficult to compete with established technologies under current conditions.

To achieve the commercialization of hydrides, the establishment of a comprehensive large-scale production system is essential, with quality control being a critical factor. In addition to optimizing synthesis processes and reducing energy consumption, it is also crucial to strictly control material consistency to ensure stable electrochemical performance across different production batches. Furthermore, the practical application of hydride materials is hindered by challenges such as volume expansion and poor conductivity, which necessitate further optimization through process improvements and structural design.

In summary, while hydride materials exhibit notable advantages in terms of high energy density and low weight, they still face significant challenges in terms of market availability and cost control. If production costs can be effectively reduced, synthesis processes optimized, and cycle stability enhanced, hydride materials have the potential to become strong contenders for next-generation high-energy-density energy storage systems.

## 5. Conclusion

This paper provides a comprehensive overview of the recent advancements, challenges, and future prospects in the development of Li/Mg-based hydrides for both hydrogen and lithium storage applications. For hydrogen storage, advances in catalytic modification, including multi-component and nanosized catalysts, have significantly improved performance. However, challenges remain in generalizing catalytic mechanisms and optimizing structure–performance relationships. Thermodynamic regulation strategies, such as alloying and destabilized composite systems, have effectively enhanced reversible hydrogen storage reaction pathways, but careful balancing is needed to maintain high hydrogen storage capacity. Nanostructuring has delivered remarkable performance improvements, yet the synthesis of free-standing ultrafine nanoparticles and a deeper understanding of size-dependent effects require further investigation. Additionally, emerging external field-driven methods, particularly electromagnetic wave-driven techniques, show great potential for enabling hydrogen storage under milder conditions. Further research is needed to optimize conversion efficiency and ensure scalability for practical applications.

For lithium storage, Li/Mg-based borohydrides, such as  $\text{LiBH}_4$  and  $\text{Mg}(\text{BH}_4)_2$ , have shown considerable potential as

solid-state electrolytes due to their enhanced ionic conductivity and electrochemical stability. Modification strategies, including cation/anion substitution, composition tuning, and nanoconfinement, have optimized ion transport pathways and lowered migration barriers, while composite designs further enhance ionic conductivity, effectively suppress dendrite growth, improve mechanical strength, and promote interfacial stability and electrode compatibility to varying degrees. Similarly,  $\text{MgH}_2$  and  $\text{LiAlH}_4$  are promising anode materials for LIBs, with nanosizing and catalyst incorporation improving specific surface areas, ion diffusion, and reaction kinetics. Additionally, confinement strategies have significantly enhanced the reversibility of the electrodes. Combining hydride anodes with hydride electrolytes in all-solid-state batteries offers a promising route to enhance energy density and safety. However, the preparation of thin, large, and uniform solid-state hydride films, and the realization of large-scale film fabrication, remain significant challenges. Future research should focus on optimizing structural features at both macro and nanoscale levels, advancing doping techniques, and developing thin-film novel hydride materials to enable the industrial application of high-energy-density hydride batteries, improving the performance and scalability of next-generation lithium storage systems.

In addition, the commercialization of hydride-based energy storage systems still faces significant challenges, including high synthesis costs, complex manufacturing processes, and limited large-scale production capacity. These barriers must be addressed through technological innovation, cost reduction strategies, and enhanced support from both policy frameworks and industrial stakeholders.

## Acknowledgements

P.G., X.Z., and X.H. contributed equally to this work. This work was financially supported by the National Key R&D Program of China (No. 2022YFB40043002), the National Natural Science Foundation of China (Nos. U2130208 and 22279020), and the Science and Technology Commission of Shanghai Municipality (No. 23ZR1406500).

## Conflict of Interest

The authors declare no conflict of interest.

## Keywords

borohydrides, hydrides, hydrogen storage, Li/Mg-based hydrides, lithium storage

Received: December 19, 2024

Revised: May 12, 2025

Published online:

- [1] a) C. B. Farias, R. C. S. Barreiros, M. F. da Silva, A. A. Casazza, A. Converti, L. A. Sarubbo, *Energies* **2022**, *15*, 311; b) M. S. Dresselhaus, I. Thomas, *Nature* **2001**, *414*, 332; c) E. A. Al-Harathi, M. S. Rashid, M. Imran, M. A. Shaker, A. A. Yakouta, A. Asghar, A. Khan, *J. Alloys Compd.* **2025**, *1016*, 179026.

- [2] a) J. Yang, A. Sudik, C. Wolverton, D. J. Siegel, *Chem. Soc. Rev.* **2010**, 39, 656; b) J. Mitali, S. Dhinakaran, A. Mohamad, *Energy Storage Sav.* **2022**, 1, 166; c) A. Khan, R. R. Kumar, J. Cong, M. Imran, D. Yang, X. Yu, *Adv. Mater. Interfaces* **2022**, 9, 2100977.
- [3] a) M. Li, J. Lu, Z. Chen, K. Amine, *Adv. Mater.* **2018**, 30, 1800561; b) V. Etacheri, R. Marom, R. Elazari, G. Salitra, D. Aurbach, *Energy Environ. Sci.* **2011**, 4, 3243; c) F. Zheng, M. Kotobuki, S. Song, M. O. Lai, L. Lu, *J. Power Sources* **2018**, 389, 198.
- [4] a) Y. Liu, H. Pan, M. Gao, Q. Wang, *J. Mater. Chem.* **2011**, 21, 4743; b) S. Sartori, F. Cuevas, M. Latroche, *Appl. Phys. A* **2016**, 122, 135; c) T. Yi, E. Zhao, Y. He, T. Liang, H. Wang, *eScience* **2024**, 4, 100182; d) Z. Wu, S. He, C. Zheng, J. Gan, L. She, M. Zhang, Y. Gao, Y. Yang, H. Pan, *eScience* **2024**, 4, 100247.
- [5] X. Zhang, Z. Lou, M. Gao, H. Pan, Y. Liu, *Acc. Mater. Res.* **2024**, 5, 371.
- [6] S. Brutti, G. Mulas, E. Piciollo, S. Panero, P. Reale, *J. Mater. Chem.* **2012**, 22, 14531.
- [7] a) Y. Wei, Z. Li, Z. Chen, P. Gao, M. Gao, C. Yan, Z. Wu, Q. Ma, Y. Jiang, X. Yu, *Energy Environ. Sci.* **2023**, 16, 4679; b) Y. Pang, J. Pan, J. Yang, S. Zheng, C. Wang, *Electrochem. Energy Rev.* **2021**, 4, 169; c) H. Liu, Z. Ren, X. Zhang, J. Hu, M. Gao, H. Pan, Y. Liu, *Chem. Mater.* **2019**, 32, 671; d) R. Wang, W. Feng, X. Yu, Q. Shi, P. Wang, Y. Liu, J. Zhang, Y. Zhao, *eScience* **2024**, 4, 100274.
- [8] a) L. Schlappbach, A. Züttel, *Nature* **2001**, 414, 353; b) T. He, P. Pachfule, H. Wu, Q. Xu, P. Chen, *Nat. Rev. Mater.* **2016**, 1, 16059; c) I. Hassan, H. S. Ramadan, M. A. Saleh, D. Hissel, *Renewable Sustainable Energy Rev.* **2021**, 149, 111311.
- [9] a) M. R. Usman, *Renewable Sustainable Energy Rev.* **2022**, 167, 112743; b) P. Preuster, A. Alekseev, P. Wasserscheid, *Annu. Rev. Chem. Biomol. Eng.* **2017**, 8, 445.
- [10] a) L. Ouyang, K. Chen, J. Jiang, X.-S. Yang, M. Zhu, *J. Alloys Compd.* **2020**, 829, 154597; b) N. Rusman, M. Dahari, *Int. J. Hydrogen Energy* **2016**, 41, 12108; c) B. Sakintuna, F. Lamari-Darkrim, M. Hirscher, *Int. J. Hydrogen Energy* **2007**, 32, 1121.
- [11] a) X. Zhang, Y. Liu, X. Zhang, J. Hu, M. Gao, H. Pan, *Mater. Today Nano* **2020**, 9, 100064; b) H.-W. Li, Y. Yan, S.-i. Orimo, A. Züttel, C. M. Jensen, *Energies* **2011**, 4, 185; c) Y. Sun, C. Shen, Q. Lai, W. Liu, D.-W. Wang, K.-F. Aguey-Zinsou, *Energy Storage Mater.* **2018**, 10, 168; d) J. Hu, Y. Liu, G. Wu, Z. Xiong, Y. S. Chua, P. Chen, *Chem. Mater.* **2008**, 20, 4398.
- [12] a) A. Züttel, P. Wenger, S. Rentsch, P. Sudan, P. Mauron, C. Emmenegger, *J. Power Sources* **2003**, 118, 1; b) W. Zhang, X. Zhang, Z. Huang, H.-W. Li, M. Gao, H. Pan, Y. Liu, *Adv. Energy Sustainability Res.* **2021**, 2, 2100073.
- [13] a) X. Zhang, Y. Sun, G. Xia, X. Yu, *J. Alloys Compd.* **2022**, 899, 163254; b) X. Yu, Z. Tang, D. Sun, L. Ouyang, M. Zhu, *Prog. Mater. Sci.* **2017**, 88, 1; c) Y. Liu, W. Zhang, X. Zhang, L. Yang, Z. Huang, F. Fang, W. Sun, M. Gao, H. Pan, *Renewable Sustainable Energy Rev.* **2023**, 184, 113560.
- [14] a) G. L. Soloveichik, Y. Gao, J. Rijssenbeek, M. Andrus, S. Kniajanski, R. C. Bowman Jr., S.-J. Hwang, J.-C. Zhao, *Int. J. Hydrogen Energy* **2009**, 34, 916; b) B. Zhang, Y. Wu, *Prog. Nat. Sci.: Mater. Int.* **2017**, 27, 21.
- [15] J. Lyu, V. Kudiiarov, L. Svyatkin, A. Lider, K. Dai, *Catalysts* **2023**, 13, 519.
- [16] E. Ivanov, I. Konstanchuk, A. Stepanov, V. Boldyrev, *J. Less-Common Met.* **1987**, 131, 25.
- [17] B. Zhao, F. Fang, D. Sun, Q. Zhang, S. Wei, F. Cao, H. Sun, L. Ouyang, M. Zhu, *J. Solid State Chem.* **2012**, 192, 210.
- [18] Y. Wang, Z. Lan, H. Fu, H. Liu, J. Guo, *Int. J. Hydrogen Energy* **2020**, 45, 13376.
- [19] S. Luo, S. Li, Y. Liu, J. Zhang, Y. Zhu, Y. Zhang, H. Lin, L. Li, *J. Alloys Compd.* **2019**, 806, 370.
- [20] C. Peng, Y. Li, Q. Zhang, *J. Alloys Compd.* **2022**, 900, 163547.
- [21] a) J. Zhang, L. He, Y. Yao, X. J. Zhou, L. P. Yu, X. Z. Lu, D. W. Zhou, *Renewable Energy* **2020**, 154, 1229; b) X. Zhang, S. Ju, C. Li, J. Hao, Y. Sun, X. Hu, W. Chen, J. Chen, L. He, G. Xia, F. Fang, D. Sun, X. Yu, *Nat. Commun.* **2024**, 15, 2815.
- [22] D. Formenti, F. Ferretti, F. K. Scharnagl, M. Beller, *Chem. Rev.* **2019**, 119, 2611.
- [23] W.-Q. Li, M. Xu, J.-S. Chen, T.-N. Ye, *Adv. Mater.* **2024**, 36, 2408434.
- [24] H. Gasan, O. N. Celik, N. Aydinbeyli, Y. M. Yaman, *Int. J. Hydrogen Energy* **2012**, 37, 1912.
- [25] G. Liang, J. Huot, S. Boily, A. Van Neste, R. Schulz, *J. Alloys Compd.* **1999**, 292, 247.
- [26] W. Zhu, L. Ren, C. Lu, H. Xu, F. Sun, Z. Ma, J. Zou, *ACS Nano* **2021**, 15, 18494.
- [27] N. Xu, H. Zhou, M. Zhang, Y. Ye, K. Wang, Y. Zhou, Y. Zhu, Y. Zhang, *J. Mater. Sci. Technol.* **2024**, 191, 49.
- [28] Y. K. Gautam, A. Sanger, A. Kumar, R. Chandra, *Int. J. Hydrogen Energy* **2015**, 40, 15549.
- [29] N. Xu, K. Wang, Y. Zhu, Y. Zhang, *Adv. Mater.* **2023**, 35, 2303173.
- [30] a) M. Song, R. Xie, L. Zhang, X. Wang, Z. Yao, T. Wei, D. Shang, *Int. J. Miner., Metall. Mater.* **2023**, 30, 970; b) X. Yang, L. Ji, N. Yan, Z. Sun, X. Lu, L. Zhang, X. Zhu, L. Chen, *Dalton Trans.* **2019**, 48, 12699; c) X. Lu, L. Zhang, H. Yu, Z. Lu, J. He, J. Zheng, F. Wu, L. Chen, *Chem. Eng. J.* **2021**, 422, 130101; d) L. Zhang, Z. Cai, X. Zhu, Z. Yao, Z. Sun, L. Ji, N. Yan, B. Xiao, L. Chen, *J. Alloys Compd.* **2019**, 805, 295.
- [31] a) J. Cermak, L. Kral, P. Roupčova, *Renewable Energy* **2022**, 188, 411; b) T. Zhong, H. Zhang, M. Song, Y. Jiang, D. Shang, F. Wu, L. Zhang, *Int. J. Miner., Metall. Mater.* **2023**, 30, 2270.
- [32] J. Zhang, H. Liu, C. Zhou, P. Sun, X. Guo, Z. Z. Fang, *J. Mater. Chem. A* **2023**, 11, 4789.
- [33] a) J. Cui, H. Wang, J. Liu, L. Ouyang, Q. Zhang, D. Sun, X. Yao, M. Zhu, *J. Mater. Chem. A* **2013**, 1, 5603; b) X. Wang, X. Xiao, J. Zheng, Z. Hang, W. Lin, Z. Yao, M. Zhang, L. Chen, *Int. J. Hydrogen Energy* **2021**, 46, 23737.
- [34] H. Wang, J. Li, X. Wei, Y. Zheng, S. Yang, Y. Lu, Z. Ding, Q. Luo, Q. Li, F. Pan, *Adv. Funct. Mater.* **2024**, 34, 2406639.
- [35] H. Guan, J. Liu, Q. Li, Y. Lu, F. Pan, *J. Magnesium Alloys* **2025**, <https://doi.org/10.1016/j.jma.2025.02.032>.
- [36] H. Guan, J. Liu, X. Sun, Y. Lu, H. Wang, Q. Luo, Q. Li, F. Pan, *Adv. Mater.* **2025**, <https://doi.org/10.1002/adma.202500178>.
- [37] Y. Meng, S. Ju, W. Chen, X. Chen, G. Xia, D. Sun, X. Yu, *Small Struct.* **2022**, 3, 2200119.
- [38] a) Y. H. Guo, X. B. Yu, L. Gao, G. L. Xia, Z. P. Guo, H. K. Liu, *Energy Environ. Sci.* **2010**, 3, 465; b) Y. Li, J. S. Chung, S. G. Kang, *Int. J. Hydrogen Energy* **2019**, 44, 6065.
- [39] M. Au, A. R. Jurgensen, W. A. Spencer, D. L. Anton, F. E. Pinkerton, S.-J. Hwang, C. Kim, R. C. Bowman, Jr., *J. Phys. Chem. C* **2008**, 112, 18661.
- [40] W. Cai, H. Wang, J. Liu, L. Jiao, Y. Wang, L. Ouyang, T. Sun, D. Sun, H. Wang, X. Yao, M. Zhu, *Nano Energy* **2014**, 10, 235.
- [41] W. Cai, Y. Yang, P. Tao, L. Ouyang, H. Wang, *Dalton Trans.* **2018**, 47, 4987.
- [42] M. G. Kim, S. Kang, B. C. Wood, E. S. Cho, *J. Mater. Chem. A* **2024**, 12, 27212.
- [43] H. Lu, J. Li, K. Nie, R. Zhang, Y. a. Chen, F. Pan, *J. Phys. Chem. Lett.* **2025**, 16, 3525.
- [44] X. Zhou, H. Guan, H. Lu, Y. Lu, J. Li, J. Wang, Y. a. Chen, Q. Li, F. Pan, *J. Magnesium Alloys* **2025**, 13, 571.
- [45] L. Zang, W. Sun, S. Liu, Y. Huang, H. Yuan, Z. Tao, Y. Wang, *ACS Appl. Mater. Interfaces* **2018**, 10, 19598.
- [46] Y. Fan, D. Chen, X. Liu, G. Fan, B. Liu, *Int. J. Hydrogen Energy* **2019**, 44, 29297.
- [47] X. Zhang, X. Zhang, L. Zhang, Z. Huang, L. Yang, M. Gao, C. Gu, W. Sun, H. Pan, Y. Liu, *ACS Appl. Nano Mater.* **2023**, 6, 14527.

- [48] a) S. Wang, M. Gao, Z. Yao, K. Xian, M. Wu, Y. Liu, W. Sun, H. Pan, *J. Magnesium Alloys* **2022**, *10*, 3354; b) K. Wang, X. Zhang, Y. Liu, Z. Ren, X. Zhang, J. Hu, M. Gao, H. Pan, *Chem. Eng. J.* **2021**, *406*, 126831; c) Q. Meng, Y. Huang, J. Ye, G. Xia, G. Wang, L. Dong, Z. Yang, X. Yu, *J. Alloys Compd.* **2021**, *851*, 156874.
- [49] M. Chen, X. Xiao, X. Wang, Y. Lu, M. Zhang, J. Zheng, L. Chen, *Carbon* **2020**, *166*, 46.
- [50] Y. Huang, C. An, Q. Zhang, L. Zang, H. Shao, Y. Liu, Y. Zhang, H. Yuan, C. Wang, Y. Wang, *Nano Energy* **2021**, *80*, 105535.
- [51] J. Xu, Y. Li, J. Cao, R. Meng, W. Wang, Z. Chen, *Catal. Sci. Technol.* **2015**, *5*, 1821.
- [52] a) Y. Ding, C. Li, X. Zhang, W. Chen, X. Yu, G. Xia, *ACS Appl. Mater. Interfaces* **2024**, *16*, 50717; b) Y. Liu, W. Chen, S. Ju, X. Yu, G. Xia, *J. Mater. Sci. Technol.* **2024**, *202*, 192.
- [53] C. Zhu, M. Chen, M. Hu, D. He, Y. Liu, T. Liu, *Int. J. Hydrogen Energy* **2021**, *46*, 9443.
- [54] Y. Jia, B. Han, J. Wang, S. Yuan, L. Tang, Z. Zhang, Y. Zou, L. Sun, Y. Du, L. Chen, *Adv. Mater.* **2024**, *36*, 2406152.
- [55] a) F. A. Halim Yap, N. S. Mustafa, M. S. Yahya, A. A. Mohamad, M. Ismail, *Int. J. Hydrogen Energy* **2018**, *43*, 8365; b) Y. Pang, Y. Liu, X. Zhang, Q. Li, M. Gao, H. Pan, *Chem. - Asian J.* **2015**, *10*, 2452.
- [56] a) C. N. C. Hitam, M. A. A. Aziz, A. H. Ruhaimi, M. R. Taib, *Int. J. Hydrogen Energy* **2021**, *46*, 31067; b) Y. Lu, H. Kim, K. Sakaki, S. Hayashi, K. Jimura, K. Asano, *Inorg. Chem.* **2019**, *58*, 14600.
- [57] a) P. Dansirima, S. Thiangviriyi, P. Plerdsranoy, N. Chanlek, R. Utke, *RSC Adv.* **2023**, *13*, 16926; b) L. ChitsazKhoji, S. Raygan, M. Pourabdoli, *Int. J. Hydrogen Energy* **2013**, *38*, 6687.
- [58] a) H. C. Zhong, H. Wang, L. Z. Ouyang, *Int. J. Hydrogen Energy* **2014**, *39*, 3320; b) Y. Lu, H. Wang, J. Liu, L. Ouyang, M. Zhu, *J. Power Sources* **2018**, *396*, 796.
- [59] J. J. Reilly Jr., R. H. Wiswall Jr., *Inorg. Chem.* **1968**, *7*, 2254.
- [60] X. Q. Tran, S. D. McDonald, Q. Gu, T. Yamamoto, K. Shigematsu, K. Aso, E. Tanaka, S. Matsumura, K. Nogita, *J. Power Sources* **2017**, *341*, 130.
- [61] a) X. Q. Tran, S. D. McDonald, Q. Gu, X. F. Tan, K. Nogita, *Int. J. Hydrogen Energy* **2017**, *42*, 6851; b) Y. H. Cho, S. Aminorroaya, H. K. Liu, A. K. Dahle, *Int. J. Hydrogen Energy* **2011**, *36*, 4984; c) W. Cao, X. Ding, R. Chen, J. Zhang, Y. Zhang, H. Shen, H. Fu, *Chem. Eng. J.* **2023**, *475*, 146252.
- [62] X. Liu, S. Wu, X. Cai, L. Zhou, *Int. J. Hydrogen Energy* **2023**, *48*, 17202.
- [63] J. J. Vajo, F. Mertens, C. C. Ahn, R. C. Bowman Jr., B. Fultz, *J. Phys. Chem. B* **2004**, *108*, 13977.
- [64] A.-L. Chaudhary, M. Paskevicius, D. A. Sheppard, C. E. Buckley, *J. Alloys Compd.* **2015**, *623*, 109.
- [65] a) L. Z. Ouyang, Z. J. Cao, H. Wang, J. W. Liu, D. L. Sun, Q. A. Zhang, M. Zhu, *Int. J. Hydrogen Energy* **2013**, *38*, 8881; b) Z. Ma, Z. Huang, Z. Li, G. Chen, Y. Li, W. Zhu, W. Zhao, H. Ji, H. Fang, W. Wen, W. Yin, J. Zou, Y. Xiao, *Energy Storage Mater.* **2023**, *56*, 432.
- [66] H. C. Zhong, H. Wang, J. W. Liu, D. L. Sun, M. Zhu, *Scr. Mater.* **2011**, *65*, 285.
- [67] Y. Xu, C. Peng, Q. Zhang, *Dalton Trans.* **2024**, *53*, 12494.
- [68] T. Si, Y. Cao, Q. Zhang, D. Sun, L. Ouyang, M. Zhu, *J. Mater. Chem. A* **2015**, *3*, 8581.
- [69] J. Qin, X. Zhou, Y. Fu, J. Liu, H. Wang, L. Ouyang, M. Zeng, Y.-J. Zhao, M. Zhu, *Acta Mater.* **2024**, *263*, 119470.
- [70] C. Lu, J. Zou, X. Shi, X. Zeng, W. Ding, *Int. J. Hydrogen Energy* **2017**, *42*, 2239.
- [71] G. Xia, Y. Tan, X. Chen, D. Sun, Z. Guo, H. Liu, L. Ouyang, M. Zhu, X. Yu, *Adv. Mater.* **2015**, *27*, 5981.
- [72] W. Grochala, P. P. Edwards, *Chem. Rev.* **2004**, *104*, 1283.
- [73] X. Yang, J. Kong, X. Lu, J. Su, Q. Hou, W. Li, *Int. J. Hydrogen Energy* **2024**, *60*, 308.
- [74] a) H. W. Li, S. Orimo, Y. Nakamori, K. Miwa, N. Ohba, S. Towata, A. Züttel, *J. Alloys Compd.* **2007**, *446–447*, 315; b) D. B. Ravnsbæk, C. Frommen, D. Reed, Y. Filinchuk, M. Sørby, B. C. Hauback, H. J. Jakobsen, D. Book, F. Besenbacher, J. Skibsted, T. R. Jensen, *J. Alloys Compd.* **2011**, *509*, S698.
- [75] P. Choudhury, S. S. Srinivasan, V. R. Bhethanabotla, Y. Goswami, K. McGrath, E. K. Stefanakos, *Int. J. Hydrogen Energy* **2009**, *34*, 6325.
- [76] a) S. Hino, J. E. Fonnelløp, M. Corno, O. Zavorotynska, A. Damin, B. Richter, M. Baricco, T. R. Jensen, M. H. Sørby, B. C. Hauback, J. Phys. Chem. C **2012**, *116*, 12482; b) L. M. Arnbjerg, D. B. Ravnsbæk, Y. Filinchuk, R. T. Vang, Y. Cerenius, F. Besenbacher, J.-E. Jørgensen, H. J. Jakobsen, T. R. Jensen, *Chem. Mater.* **2009**, *21*, 5772.
- [77] L. Yin, P. Wang, Z. Fang, H. Cheng, *Chem. Phys. Lett.* **2008**, *450*, 318.
- [78] F. Fang, Y. Li, Y. Song, D. Sun, Q. Zhang, L. Ouyang, M. Zhu, *J. Phys. Chem. C* **2011**, *115*, 13528.
- [79] Y. Huang, X. Mo, C. Hu, Y. Ma, X. Zuo, R. Zhou, W. Jiang, *Int. J. Hydrogen Energy* **2024**, *50*, 148.
- [80] J. J. Vajo, S. L. Skeith, F. Mertens, *J. Phys. Chem. B* **2005**, *109*, 3719.
- [81] L. L. Shaw, X. Wan, J. Z. Hu, J. H. Kwak, Z. Yang, *J. Phys. Chem. C* **2010**, *114*, 8089.
- [82] U. Bösenberg, D. B. Ravnsbæk, H. Hagemann, V. D'Anna, C. B. Minella, C. Pistidda, W. van Beek, T. R. Jensen, R. Bormann, M. Dornheim, *J. Phys. Chem. C* **2010**, *114*, 15212.
- [83] W. Chen, Y.-H. Sun, T. Xu, X.-B. Yu, G.-L. Xia, *Rare Met.* **2024**, *43*, 4367.
- [84] a) W. Chen, Y. Sun, T. Xu, J. Ye, G. Xia, D. Sun, X. Yu, *ACS Appl. Energy Mater.* **2022**, *5*, 10501; b) X. Fan, X. Xiao, L. Chen, X. Wang, S. Li, H. Ge, Q. Wang, *J. Mater. Chem. A* **2013**, *1*, 11368.
- [85] Y.-K. Liu, Y.-C. Pang, C.-Q. Li, X.-Y. Zhang, X.-C. Hu, W. Chen, X.-B. Yu, G.-L. Xia, *Rare Met.* **2025**, <https://doi.org/10.1007/s12598-025-03327-6>.
- [86] L.-W. Lu, H. Luo, G.-X. Li, Y. Li, X.-H. Wang, C.-K. Huang, Z.-Q. Lan, W.-Z. Zhou, J. Guo, M. Ismail, *Rare Met.* **2024**, *43*, 1153.
- [87] Z. Ma, J. Zhang, W. Hu, Q. Wang, Z. Sun, F. Fang, Y. Song, D. Sun, *Adv. Energy Mater.* **2024**, *14*, 2401156.
- [88] a) J.-H. Lim, J.-H. Shim, Y.-S. Lee, J.-Y. Suh, Y. W. Cho, J. Lee, *Int. J. Hydrogen Energy* **2010**, *35*, 6578; b) J. Zheng, X. Xiao, L. Zhang, Y. He, S. Li, H. Ge, L. Chen, *Int. J. Hydrogen Energy* **2017**, *42*, 8050.
- [89] H. W. Li, K. Kikuchi, Y. Nakamori, K. Miwa, S. Towata, S. Orimo, *Scr. Mater.* **2007**, *57*, 679.
- [90] P. Chen, Z. Xiong, J. Luo, J. Lin, K. L. Tan, *Nature* **2002**, *420*, 302.
- [91] a) T. Ichikawa, H. Y. Leng, S. Isobe, N. Hanada, H. Fujii, *J. Power Sources* **2006**, *159*, 126; b) M. H. Park, H. Kim, J. J. Urm, J. H. Lee, Y.-K. Han, Y. S. Lee, *J. Mol. Struct.: THEOCHEM* **2010**, *962*, 68.
- [92] H. Li, Z. Li, M. Luo, H. Yuan, Y. Wu, X. Guo, L. Hao, *J. Mater. Sci.* **2023**, *58*, 16269.
- [93] a) C. Liang, Y. Liu, H. Fu, Y. Ding, M. Gao, H. Pan, *J. Alloys Compd.* **2011**, *509*, 7844; b) H. Leng, T. Ichikawa, H. Fujii, *J. Phys. Chem. B* **2006**, *110*, 12964.
- [94] J. H. Jung, D. Kim, J. Hwang, Y.-L. Lee, J. Ihm, *Int. J. Hydrogen Energy* **2016**, *41*, 17506.
- [95] J. Wang, P. Chen, H. Pan, Z. Xiong, M. Gao, G. Wu, C. Liang, C. Li, B. Li, J. Wang, *ChemSusChem* **2013**, *6*, 2181.
- [96] J. Wang, G. Wu, Y. S. Chua, J. Guo, Z. Xiong, Y. Zhang, M. Gao, H. Pan, P. Chen, *ChemSusChem* **2011**, *4*, 1622.
- [97] B. Li, Y. Liu, C. Li, M. Gao, H. Pan, *J. Mater. Chem. A* **2014**, *2*, 3155.
- [98] a) X. Wang, X. Xiao, Z. Liang, S. Zhang, J. Qi, L. Lv, M. Piao, J. Zheng, L. Chen, *Chem. Eng. J.* **2022**, *433*, 134482; b) Z. Li, K. Xian, M. Gao, S. Wang, S. Qu, M. Wu, J. Gan, Y. Yang, X. Zhang, W. Sun, Y. Liu, H. Pan, *ACS Appl. Mater. Interfaces* **2024**, *16*, 47571.
- [99] a) Y. Liu, K. Zhong, K. Luo, M. Gao, H. Pan, Q. Wang, *J. Am. Chem. Soc.* **2009**, *131*, 1862; b) G. Xia, X. Chen, C. Zhou, C. Zhang, D. Li, Q. Gu, Z. Guo, H. Liu, Z. Liu, X. Yu, *J. Mater. Chem. A* **2015**, *3*, 12646.
- [100] W. Yunting, X. Yudong, Z. Andreas, *Chem. Soc. Rev.* **2024**, *53*, 972.

- [101] A. Schneemann, J. L. White, S. Kang, S. Jeong, L. F. Wan, E. S. Cho, T. W. Heo, D. Prendergast, J. J. Urban, B. C. Wood, *Chem. Rev.* **2018**, *118*, 10775.
- [102] P. Balaya, *Energy Environ. Sci.* **2008**, *1*, 645.
- [103] A. Zaluska, L. Zaluski, J. Ström-Olsen, *J. Alloys Compd.* **1999**, *288*, 217.
- [104] R. Schulz, J. Huot, G. Liang, S. Boily, G. Lalande, M. Denis, J. Dodelet, *Mater. Sci. Eng., A* **1999**, *267*, 240.
- [105] J. Huot, D. B. Ravnsbæk, J. Zhang, F. Cuevas, M. Latroche, T. R. Jensen, *Prog. Mater. Sci.* **2013**, *58*, 30.
- [106] M. Paskevicius, D. A. Sheppard, C. E. Buckley, *J. Am. Chem. Soc.* **2010**, *132*, 5077.
- [107] C. Suryanarayana, *Research* **2019**, *2019*, 4219812.
- [108] R. Zou, W. Zhang, M. Dai, G. Lei, Q. Jiang, H. Cao, P. Chen, *Small* **2023**, *19*, 2206518.
- [109] W. Li, C. Li, H. Ma, J. Chen, *J. Am. Chem. Soc.* **2007**, *129*, 6710.
- [110] a) A. Léon, E. Knystautas, J. Huot, R. Schulz, *J. Alloys Compd.* **2002**, *345*, 158; b) A. Léon, E. Knystautas, J. Huot, R. Schulz, *Thin Solid Films* **2006**, *496*, 683.
- [111] R. Shimizu, T. Kakinokizono, I. Gu, T. Hitosugi, *Inorg. Chem.* **2019**, *58*, 15354.
- [112] L. Jinzhe, A. M. Lider, V. N. Kudiiarov, *Chin. Phys. B* **2019**, *28*, 098801.
- [113] K. Higuchi, H. Kajioaka, K. Toiyama, H. Fujii, S. Orimo, Y. Kikuchi, *J. Alloys Compd.* **1999**, *293*, 484.
- [114] A. Krozer, B. Kasemo, *J. Less-Common Met.* **1990**, *160*, 323.
- [115] a) L. Ouyang, H. Wang, M. Zhu, J. Zou, C. Chung, *J. Alloys Compd.* **2005**, *404*, 485; b) H. Wang, L. Ouyang, M. Zeng, M. Zhu, *J. Alloys Compd.* **2004**, *375*, 313; c) M. Zhu, Y. Gao, X. Che, Y. Yang, C. Chung, *J. Alloys Compd.* **2002**, *330*, 708.
- [116] C. Shen, K.-F. Aguey-Zinsou, *Int. J. Hydrogen Energy* **2018**, *43*, 22385.
- [117] S. Makridis, E. I. Gkanas, G. Panagakos, E. Kikkinides, A. Stubos, P. Wagener, S. Barcikowski, *Int. J. Hydrogen Energy* **2013**, *38*, 11530.
- [118] I. Saita, T. Toshima, S. Tanda, T. Akiyama, *J. Alloys Compd.* **2007**, *446*, 80.
- [119] a) C. Zhu, H. Hayashi, I. Saita, T. Akiyama, *Int. J. Hydrogen Energy* **2009**, *34*, 7283; b) C. Zhu, S. Hosokai, I. Matsumoto, T. Akiyama, *Cryst. Growth Des.* **2010**, *10*, 5123.
- [120] C. Zhu, S. Hosokai, T. Akiyama, *Int. J. Hydrogen Energy* **2012**, *37*, 8379.
- [121] N. S. Norberg, T. S. Arthur, S. J. Fredrick, A. L. Prieto, *J. Am. Chem. Soc.* **2011**, *133*, 10679.
- [122] W. Liu, K.-F. Aguey-Zinsou, *J. Mater. Chem. A* **2014**, *2*, 9718.
- [123] E. J. Setijadi, C. Boyer, K.-F. Aguey-Zinsou, *Phys. Chem. Chem. Phys.* **2012**, *14*, 11386.
- [124] N. Rambhujun, K.-F. Aguey-Zinsou, *Int. J. Hydrogen Energy* **2021**, *46*, 28675.
- [125] P. E. de Jongh, P. Adelhelm, *ChemSusChem* **2010**, *3*, 1332.
- [126] a) H. Wang, S. Zhang, J. Liu, L. Ouyang, M. Zhu, *Mater. Chem. Phys.* **2012**, *136*, 146; b) D. W. Lim, J. W. Yoon, K. Y. Ryu, M. P. Suh, *Angew. Chem., Int. Ed.* **2012**, *51*, 9814; c) A. F. Gross, C. C. Ahn, S. L. Van Atta, P. Liu, J. J. Vajo, *Nanotechnology* **2009**, *20*, 204005; d) Y. Jia, X. Yao, *Int. J. Hydrogen Energy* **2017**, *42*, 22933.
- [127] a) P. E. de Jongh, R. W. Wagemans, T. M. Eggenhuisen, B. S. Dauvillier, P. B. Radstake, J. D. Meeldijk, J. W. Geus, K. P. de Jong, *Chem. Mater.* **2007**, *19*, 6052; b) K.-J. Jeon, H. R. Moon, A. M. Ruminski, B. Jiang, C. Kisielowski, R. Bardhan, J. J. Urban, *Nat. Mater.* **2011**, *10*, 286.
- [128] G. Xia, Y. Tan, X. Chen, D. Sun, Z. Guo, H. Liu, L. Ouyang, M. Zhu, X. Yu, *Adv. Mater.* **2015**, *27*, 5981.
- [129] X. Zhang, Y. Liu, Z. Ren, X. Zhang, J. Hu, Z. Huang, Y. Lu, M. Gao, H. Pan, *Energy Environ. Sci.* **2021**, *14*, 2302.
- [130] J. L. White, N. A. Strange, J. D. Sugar, J. L. Snider, A. Schneemann, A. S. Lipton, M. F. Toney, M. D. Allendorf, V. Stavila, *Chem. Mater.* **2020**, *32*, 5604.
- [131] X. Liu, D. Peaslee, C. Z. Jost, T. F. Baumann, E. H. Majzoub, *Chem. Mater.* **2011**, *23*, 1331.
- [132] L. Guo, Y. Li, Y. Ma, Y. Liu, D. Peng, L. Zhang, S. Han, *Int. J. Hydrogen Energy* **2017**, *42*, 2215.
- [133] P. Plerdsranoy, D. Kaewsuwan, N. Chanlek, R. Utke, *Int. J. Hydrogen Energy* **2017**, *42*, 6189.
- [134] R. Wu, X. Zhang, Y. Liu, L. Zhang, J. Hu, M. Gao, H. Pan, *Small* **2020**, *16*, 2001963.
- [135] Z. Fang, P. Wang, T. Rufford, X. Kang, G. Lu, H. Cheng, *Acta Mater.* **2008**, *56*, 6257.
- [136] M. Fichtner, Z. Zhao-Karger, J. Hu, A. Roth, P. Weidler, *Nanotechnology* **2009**, *20*, 204029.
- [137] Q. Lai, Y. Yang, K.-F. Aguey-Zinsou, *Int. J. Hydrogen Energy* **2019**, *44*, 23225.
- [138] a) X. Xu, L. Zang, Y. Zhao, Y. Liu, Y. Wang, L. Jiao, *Int. J. Hydrogen Energy* **2017**, *42*, 25824; b) H. Zhou, L. Zhang, S. Gao, H. Liu, L. Xu, X. Wang, M. Yan, *Int. J. Hydrogen Energy* **2017**, *42*, 23010; c) M. A. Wahab, Y. A. Jia, D. Yang, H. Zhao, X. Yao, *J. Mater. Chem. A* **2013**, *1*, 3471.
- [139] G. Xia, Y. Tan, X. Chen, F. Fang, D. Sun, X. Li, Z. Guo, X. Yu, *Adv. Sci.* **2017**, *4*, 1600257.
- [140] H. Zhang, G. Xia, J. Zhang, D. Sun, Z. Guo, X. Yu, *Adv. Energy Mater.* **2018**, *8*, 1702975.
- [141] Y. Wang, X. Chen, H. Zhang, G. Xia, D. Sun, X. Yu, *Adv. Mater.* **2020**, *32*, 2002647.
- [142] W. Zhang, L. Zhou, X. Zhang, Z. Huang, F. Fang, Z. Hong, J. Li, M. Gao, W. Sun, H. Pan, *Small* **2024**, *20*, 2400965.
- [143] W. Zhang, L. Zhou, X. Zhang, L. Zhang, Z. Lou, B. Guo, Z. Hong, M. Gao, W. Sun, Y. Liu, *Nano Energy* **2024**, *130*, 110128.
- [144] X. Zhang, L. Zhang, W. Zhang, Z. Ren, Z. Huang, J. Hu, M. Gao, H. Pan, Y. Liu, *Nano Energy* **2021**, *83*, 105839.
- [145] Y. Pang, Y. Liu, M. Gao, L. Ouyang, J. Liu, H. Wang, M. Zhu, H. Pan, *Nat. Commun.* **2014**, *5*, 3519.
- [146] T. Wang, K. F. Aguey-Zinsou, *Energy Technol.* **2019**, *7*, 1801159.
- [147] X. Zhang, W. Zhang, L. Zhang, Z. Huang, J. Hu, M. Gao, H. Pan, Y. Liu, *Chem. Eng. J.* **2022**, *428*, 132566.
- [148] J. Yang, D. Li, H. Fu, G. Xin, J. Zheng, X. Li, *Phys. Chem. Chem. Phys.* **2012**, *14*, 2857.
- [149] B. C. Wood, V. Stavila, N. Poonyayant, T. W. Heo, K. G. Ray, L. E. Klebanoff, T. J. Udovic, J. R. Lee, N. Angboonpong, J. D. Sugar, *Adv. Mater. Interfaces* **2017**, *4*, 1600803.
- [150] G. Xia, D. Li, X. Chen, Y. Tan, Z. Tang, Z. Guo, H. Liu, Z. Liu, X. Yu, *Adv. Mater.* **2013**, *25*, 6238.
- [151] G. Xia, Y. Tan, D. Li, Z. Guo, H. Liu, Z. Liu, X. Yu, *Sci. Rep.* **2014**, *4*, 6599.
- [152] A. Ishimaru, *Electromagnetic Wave Propagation, Radiation, and Scattering: From Fundamentals to Applications*, 2nd ed., John Wiley & Sons, New York **2017**.
- [153] G. Bekefi, A. H. Barrett, *Electromagnetic Vibrations, Waves, and Radiation*, 3rd ed., MIT Press, Cambridge, MA **1977**.
- [154] a) O. Morton, *Nature* **2006**, *443*, 19; b) N. Kannan, D. Vakeesan, *Renewable Sustainable Energy Rev.* **2016**, *62*, 1092.
- [155] D. Dougherty, P. Herley, *J. Less-Common Met.* **1980**, *73*, 97.
- [156] Z. Cheng, Y. Guan, H. Wen, Z. Li, K. Cui, Q. Pei, S. Wang, C. Pistidda, J. Guo, H. Cao, *J. Phys. Chem. Lett.* **2024**, *15*, 6662.
- [157] X. Zhang, C. Li, J. Ye, X. Hu, W. Chen, F. Fang, D. Sun, Y. Liu, X. Yu, G. Xia, *J. Am. Chem. Soc.* **2025**, *147*, 2786.
- [158] Y. Guan, H. Wen, K. Cui, Q. Wang, W. Gao, Y. Cai, Z. Cheng, Q. Pei, Z. Li, H. Cao, *Nat. Chem.* **2024**, *16*, 373.
- [159] Y. Sun, K. F. Aguey-Zinsou, *ChemPlusChem* **2018**, *83*, 904.

- [160] Y. Sun, X. Zhang, W. Chen, J. Ye, S. Ju, K. F. Aguey-Zinsou, G. Xia, D. Sun, X. Yu, *Small* **2022**, *18*, 2202978.
- [161] L. Feng, Y. Liu, Y. Jiang, Y. Guo, Y. Sun, Y. Wang, *J. Alloys Compd.* **2025**, *1010*, 176848.
- [162] X. Zhang, Y. Sun, S. Ju, J. Ye, X. Hu, W. Chen, L. Yao, G. Xia, F. Fang, D. Sun, *Adv. Mater.* **2023**, *35*, 2206946.
- [163] X. Hu, X. Chen, X. Zhang, Y. Meng, G. Xia, X. Yu, D. Sun, F. Fang, *Adv. Sci.* **2024**, *11*, 2400274.
- [164] N. Scriven, G. Thoburn, N. Tanbouza, C. Darby, E. Carlisle, H. Hamilton, E. Otumudia, I. S. M. Santos, M. Spencelayh, C. Woof, *Image* **2023**, *10*, 3012.
- [165] a) Y. Nakamori, S.-i. Orimo, T. Tsutaoka, *Appl. Phys. Lett.* **2006**, *88*, 112104; b) Y. Nakamori, M. Matsuo, K. Yamada, T. Tsutaoka, S.-i. Orimo, *J. Alloys Compd.* **2007**, *446*, 698.
- [166] M. Matsuo, Y. Nakamori, K. Yamada, S.-i. Orimo, *Appl. Phys. Lett.* **2007**, *90*, 232907.
- [167] R. Zou, J. A. Bolarin, G. T. Lei, W. B. Gao, Z. Li, H. J. Cao, P. Chen, *Chem. Eng. J.* **2022**, *450*, 138072.
- [168] H. Zhang, H. Geerlings, J. Lin, W. S. Chin, *Int. J. Hydrogen Energy* **2011**, *36*, 7580.
- [169] a) L. Ouyang, J. Huang, H. Wang, J. Liu, M. Zhu, *Mater. Chem. Phys.* **2017**, *200*, 164; b) Y. Liu, Y. Cao, L. Huang, M. Gao, H. Pan, *J. Alloys Compd.* **2011**, *509*, 675.
- [170] a) E. Deprez, A. Justo, T. Rojas, C. López-Cartés, C. B. Minella, U. Bösenberg, M. Dornheim, R. Bormann, A. Fernández, *Acta Mater.* **2010**, *58*, 5683; b) S. D. House, X. Liu, A. A. Rockett, E. H. Majzoub, I. M. Robertson, *J. Phys. Chem. C* **2014**, *118*, 8843; c) V. Bhosle, E. Baburaj, M. Miranova, K. Salama, *Mater. Sci. Eng., A* **2003**, *356*, 190.
- [171] A. Surrey, L. Schultz, B. Rellinghaus, *Adv. Struct. Chem. Imaging* **2016**, *2*, 7.
- [172] R. Nevshupa, J. R. Ares, J. F. Fernández, A. Del Campo, E. Roman, *J. Phys. Chem. Lett.* **2015**, *6*, 2780.
- [173] R. Nevshupa, *J. Frict. Wear* **2009**, *30*, 118.
- [174] a) J. Cuan, Y. Zhou, T. Zhou, S. Ling, K. Rui, Z. Guo, H. Liu, X. Yu, *Adv. Mater.* **2019**, *31*, 1803533; b) A. Manthiram, X. Yu, S. Wang, *Nat. Rev. Mater.* **2017**, *2*, 16103.
- [175] a) B. Boukamp, R. Huggins, *Phys. Lett. A* **1979**, *72*, 464; b) M. Matsuo, Y. Nakamori, S.-i. Orimo, H. Maekawa, H. Takamura, *Appl. Phys. Lett.* **2007**, *91*, 224037.
- [176] a) Y. Pang, Y. Zhu, F. Fang, D. Sun, S. Zheng, *J. Mater. Sci. Technol.* **2023**, *161*, 136; b) H. Wang, H. Man, J. Yang, J. Zang, R. Che, F. Wang, D. Sun, F. Fang, *Adv. Funct. Mater.* **2022**, *32*, 2109887.
- [177] H. Maekawa, M. Matsuo, H. Takamura, M. Ando, Y. Noda, T. Karahashi, S.-i. Orimo, *J. Am. Chem. Soc.* **2009**, *131*, 894.
- [178] Y. Yan, R. S. Kühnel, A. Remhof, L. Duchêne, E. C. Reyes, D. Rentsch, Z. Łodziana, C. Battaglia, *Adv. Energy Mater.* **2017**, *7*, 1700294.
- [179] T. Burankova, L. Duchêne, Z. Łodziana, B. Frick, Y. Yan, R.-S. Kühnel, H. Hagemann, A. Remhof, J. P. Embs, *J. Phys. Chem. C* **2017**, *121*, 17693.
- [180] a) Y. Pang, X. Wang, X. Shi, F. Xu, L. Sun, J. Yang, S. Zheng, *Adv. Energy Mater.* **2020**, *10*, 1902795; b) R. Mohtadi, *Chem* **2018**, *4*, 1770.
- [181] a) N. Berti, E. Hadjixenophontos, F. Cuevas, J. Zhang, A. Lacoste, P. Dubot, G. Schmitz, M. Latroche, *J. Power Sources* **2018**, *402*, 99; b) T. Zhang, Y. Wang, T. Song, H. Miyaoka, K. Shinzato, H. Miyaoka, T. Ichikawa, S. Shi, X. Zhang, S. Isobe, *Joule* **2018**, *2*, 1522.
- [182] S. Higashi, K. Miwa, M. Aoki, K. Takechi, *Chem. Commun.* **2014**, *50*, 1320.
- [183] a) Y. Yan, W. Dononelli, M. Jørgensen, J. B. Grinderslev, Y.-S. Lee, Y. W. Cho, R. Černý, B. Hammer, T. R. Jensen, *Phys. Chem. Chem. Phys.* **2020**, *22*, 9204; b) Y. Pang, Z. Nie, F. Xu, L. Sun, J. Yang, D. Sun, F. Fang, S. Zheng, *Energy Environ. Mater.* **2024**, *7*, 12527.
- [184] M. B. Ley, D. B. Ravnsbæk, Y. Filinchuk, Y.-S. Lee, R. Janot, Y. W. Cho, J. Skibsted, T. R. Jensen, *Chem. Mater.* **2012**, *24*, 1654.
- [185] M. Xiang, Y. Zhang, H. Lin, Y. Zhu, X. Guo, J. Chen, L. Li, J. *Alloys Compd.* **2018**, *764*, 307.
- [186] P. Ngene, M. H. Verkuiljen, Q. Zheng, J. Kragten, P. J. M. van Bentum, J. H. Bitter, P. E. de Jongh, *Faraday Discuss.* **2011**, *151*, 47.
- [187] D. Blanchard, A. Nale, D. Sveinbjörnsson, T. M. Eggenhuisen, M. H. Verkuiljen, Suwarno, A. P. Kentgens, P. E. de Jongh, *Adv. Funct. Mater.* **2015**, *25*, 184.
- [188] S. F. Lambregts, E. R. Van Eck, P. N. Suwarno, P. E. de Jongh, A. P. Kentgens, *J. Phys. Chem. C* **2019**, *123*, 25559.
- [189] M. Zhu, Y. Pang, F. Lu, X. Shi, J. Yang, S. Zheng, *ACS Appl. Mater. Interfaces* **2019**, *11*, 14136.
- [190] Z. Liu, T. Zhang, S. Ju, Y. Ji, Z. Hu, Y. Lv, G. Xia, X. Yu, *ACS Appl. Energy Mater.* **2022**, *5*, 14301.
- [191] a) Y. Sadikin, R. V. Skoryunov, O. A. Babanova, A. V. Soloninin, Z. Łodziana, M. Brighi, A. V. Skripov, R. Cerny, *J. Phys. Chem. C* **2017**, *121*, 5503; b) J.-H. Her, W. Zhou, V. Stavila, C. M. Brown, T. J. Udovic, *J. Phys. Chem. C* **2009**, *113*, 11187; c) N. Verdál, T. J. Udovic, J. J. Rush, H. Wu, A. V. Skripov, *J. Phys. Chem. C* **2013**, *117*, 12010.
- [192] a) M. Paskevicius, M. P. Pitt, D. H. Brown, D. A. Sheppard, S. Chumphongphan, C. E. Buckley, *Phys. Chem. Chem. Phys.* **2013**, *15*, 15825; b) N. Verdál, J.-H. Her, V. Stavila, A. V. Soloninin, O. A. Babanova, A. V. Skripov, T. J. Udovic, J. J. Rush, *J. Solid State Chem.* **2014**, *212*, 81.
- [193] J. A. Teprovich Jr., J. Zhang, H. Colón-Mercado, F. Cuevas, B. Peters, S. Greenway, R. Zidan, M. Latroche, *J. Phys. Chem. C* **2015**, *119*, 4666.
- [194] W. S. Tang, A. Unemoto, W. Zhou, V. Stavila, M. Matsuo, H. Wu, S.-i. Orimo, T. J. Udovic, *Energy Environ. Sci.* **2015**, *8*, 3637.
- [195] N. Verdál, T. J. Udovic, V. Stavila, W. S. Tang, J. J. Rush, A. V. Skripov, *J. Phys. Chem. C* **2014**, *118*, 17483.
- [196] W. S. Tang, M. Matsuo, H. Wu, V. Stavila, W. Zhou, A. A. Talin, A. V. Soloninin, R. V. Skoryunov, O. A. Babanova, A. V. Skripov, *Adv. Energy Mater.* **2016**, *6*, 1502237.
- [197] S. Kim, H. Oguchi, N. Toyama, T. Sato, S. Takagi, T. Otomo, D. Arunkumar, N. Kuwata, J. Kawamura, S.-i. Orimo, *Nat. Commun.* **2019**, *10*, 1081.
- [198] V. Gulino, L. Barberis, P. Ngene, M. Baricco, P. E. De Jongh, *ACS Appl. Energy Mater.* **2020**, *3*, 4941.
- [199] Y. Yan, J. B. Grinderslev, T. Burankova, S. Wei, J. P. Embs, J. Skibsted, T. R. Jensen, *J. Phys. Chem. Lett.* **2022**, *13*, 2211.
- [200] Y. Gao, S. Sun, X. Zhang, Y. Liu, J. Hu, Z. Huang, M. Gao, H. Pan, *Adv. Funct. Mater.* **2021**, *31*, 2009692.
- [201] Y.-T. Lv, T.-F. Zhang, Z.-T. Hu, G.-L. Xia, Z.-Y. Huang, Z.-H. Liu, L.-H. Que, C.-T. Yuan, F.-Q. Guo, T. Ichikawa, *Rare Met.* **2024**, *43*, 692.
- [202] Y. Oumellal, A. Rougier, G. Nazri, J. Tarascon, L. Aymard, *Nat. Mater.* **2008**, *7*, 916.
- [203] L. Silvestri, S. Forgia, L. Farina, D. Meggiolaro, S. Panero, A. La Barbera, S. Brutti, P. Reale, *ChemElectroChem* **2015**, *2*, 877.
- [204] L. Huang, L. Aymard, J.-P. Bonnet, *J. Mater. Chem. A* **2015**, *3*, 15091.
- [205] a) D. Borsa, R. Gremaud, A. Baldi, H. Schreuders, J. Rector, B. Kooi, P. Vermeulen, P. Notten, B. Dam, R. Griessen, *Phys. Rev. B: Condens. Matter Mater. Phys.* **2007**, *75*, 205408; b) A. Baldi, R. Gremaud, D. Borsa, C. Baldé, A. Van der Eerden, G. Kruijtzter, P. De Jongh, B. Dam, R. Griessen, *Int. J. Hydrogen Energy* **2009**, *34*, 1450.
- [206] F. Lu, Y. Pang, M. Zhu, F. Han, J. Yang, F. Fang, D. Sun, S. Zheng, C. Wang, *Adv. Funct. Mater.* **2019**, *29*, 1809219.
- [207] Y. Pang, Y. Liu, J. Yang, S. Zheng, C. Wang, *Mater. Today Nano* **2022**, *18*, 100194.
- [208] Y. Kim, C. Juarez-Yescas, D. W. Liao, M. K. Jangid, P. Joshi, H. Yang, B. Zahiri, P. V. Braun, N. P. Dasgupta, *ACS Energy Lett.* **2024**, *9*, 1353.
- [209] A. H. Dao, N. Berti, P. López-Aranguren, J. Zhang, F. Cuevas, C. Jordy, M. Latroche, *J. Power Sources* **2018**, *397*, 143.
- [210] L. Zeng, K. Kawahito, S. Ikeda, T. Ichikawa, H. Miyaoka, Y. Kojima, *Chem. Commun.* **2015**, *51*, 9773.

- [211] A. El Kharbachi, H. Uesato, H. Kawai, S. Wenner, H. Miyaoka, M. H. Sørby, H. Fjellvåg, T. Ichikawa, B. C. Hauback, *RSC Adv.* **2018**, *8*, 23468.
- [212] P. Poizot, S. Laruelle, S. Grugeon, L. Dupont, J. Tarascon, *Nature* **2000**, *407*, 496.
- [213] Y. Oumellal, C. Zlotea, S. Bastide, C. Cachet-Vivier, E. Léonel, S. Sengmany, E. Leroy, L. Aymard, J.-P. Bonnet, M. Latroche, *Nanoscale* **2014**, *6*, 14459.
- [214] Y.-H. Lee, I.-C. Leu, S.-T. Chang, C.-L. Liao, K.-Z. Fung, *Electrochim. Acta* **2004**, *50*, 553.
- [215] P. Huen, D. B. Ravnsbaek, *J. Electrochem. Soc.* **2017**, *164*, A3138.
- [216] B. Zhang, Y. Si, Q. Gu, M. Chen, X. Yu, *ACS Appl. Mater. Interfaces* **2019**, *11*, 28987.
- [217] P. Gao, S. Ju, Z. Liu, G. Xia, D. Sun, X. Yu, *ACS Nano* **2022**, *16*, 8040.
- [218] Y. Huang, P. Gao, T. Zhang, X. Zhang, G. Xia, F. Fang, D. Sun, Z. Guo, X. Yu, *Small* **2023**, *19*, 2207210.
- [219] M. Jehan, D. Fruchart, *J. Alloys Compd.* **2013**, *580*, S343.
- [220] D. Fruchart, M. Jehan, N. Skryabina, P. de Rango, *Metals* **2023**, *13*, 992.
- [221] L. Ren, Y. Li, X. Lin, W. Ding, J. Zou, *Front. Energy* **2023**, *17*, 320.
- [222] X. Wang, L. Shao, S. Hu, Z. Li, H. Guo, J. Zhang, Y. Zhao, X. Lin, B. Nie, Z. Hu, *Energy Environ. Sci.* **2024**, *17*, 8429.
- [223] G. Amica, P. A. Larochette, F. C. Gennari, *Int. J. Hydrogen Energy* **2020**, *45*, 18789.
- [224] H. Li, H. Li, Y. Lai, Z. Yang, Q. Yang, Y. Liu, Z. Zheng, Y. Liu, Y. Sun, B. Zhong, *Adv. Energy Mater.* **2022**, *12*, 2102181.
- [225] L. Zhou, X. Wei, J. Zhang, X. Mei, Y. Li, C. Zheng, F. Zhang, A. Wen, B. Wang, *ACS Appl. Energy Mater.* **2024**, *8*, 473.
- [226] J. Schnell, F. Tietz, C. Singer, A. Hofer, N. Billot, G. Reinhart, *Energy Environ. Sci.* **2019**, *12*, 1818.
- [227] a) E. Wiberg, H. Goeltzer, R. Bauer, *Zeitschrift für Naturforschung B* **1951**, *6*, 394; b) Y. Kume, A. Weiss, *J. Less-Common Met.* **1987**, *136*, 51; c) A. Inoue, K. Nakano, Y. Bizen, T. Masumoto, H. S. Chen, *Jpn. J. Appl. Phys.* **1988**, *27*, L944; d) Y. Nakamori, M. Matsuo, K. Yamada, T. Tsutaoka, S. Orimo, *J. Alloys Compd.* **2007**, *446–447*, 698; e) A. F. Gross, J. J. Vajo, S. L. Van Atta, G. L. Olson, *J. Phys. Chem. C* **2008**, *112*, 5651;
- [228] Y. Jia, B. Han, J. Wang, S. Yuan, L. Tang, Z. Zhang, Y. Zou, L. Sun, Y. Du, L. Chen, X. Xiao, *Adv. Mater.* **2024**, *36*, 2406152.
- [229] J. Zhang, D. W. Zhou, L. P. He, P. Peng, J. S. Liu, *J. Phys. Chem. Solids* **2009**, *70*, 32.
- [230] S. Nayeboassadri, K. F. Aguey-Zinsou, Z. X. Guo, *Int. J. Hydrogen Energy* **2011**, *36*, 7920.
- [231] a) M. Matsuo, Y. Nakamori, S.-i. Orimo, H. Maekawa, H. Takamura, *Appl. Phys. Lett.* **2007**, *91*, 224103; b) J. A. Teprovich, H. Colón-Mercado, A. L. Washington II, P. A. Ward, S. Greenway, D. M. Missimer, H. Hartman, J. Velten, J. H. Christian, R. Zidan, *J. Mater. Chem. A* **2015**, *3*, 22853.
- [232] M. Matsuo, S. i. Orimo, *Adv. Energy Mater.* **2011**, *1*, 161.
- [233] C. Lu, S. Panda, W. Zhu, Y. Ma, J. Zou, *Int. J. Hydrogen Energy* **2024**, *50*, 979.
- [234] Y. Liu, J. Zou, X. Zeng, W. Ding, *RSC Adv.* **2014**, *4*, 42764.
- [235] L. Zhang, L. Ji, Z. Yao, N. Yan, Z. Sun, X. Yang, X. Zhu, S. Hu, L. Chen, *Int. J. Hydrogen Energy* **2019**, *44*, 21955.
- [236] C. Yang, C. Hu, X. Wu, Y. Pang, X. Liu, J. Shui, *J. Energy Chem.* **2025**, *105*, 185.
- [237] L. Zhang, K. Wang, Y. Liu, X. Zhang, J. Hu, M. Gao, H. Pan, *Nano Res.* **2021**, *14*, 148.
- [238] W. Hu, J. Zang, Q. Wang, S. Xiao, J. Zhang, F. Fang, Z. Ma, D. Sun, Y. Song, *Adv. Energy Mater.* **2025**, *15*, 2404650.
- [239] L. Wang, T. Zhong, F. Wu, D. Chen, Z. Yao, L. Chen, L. Zhang, *Chem. Eng. J.* **2025**, *505*, 159591.
- [240] Y. Zheng, L. Zhang, H. Zheng, J. Chen, Z. Chen, Y. Liu, J. Tu, C. Gu, *J. Colloid Interface Sci.* **2025**, *685*, 65.
- [241] R. A. Ocampo, J. Arias-Velandia, J. A. Lenis, A. A. Zuleta Gil, S. Bello, E. Correa, C. Arrieta, F. J. Bolívar, F. E. Echeverría, *Int. J. Hydrogen Energy* **2025**, *129*, 91.
- [242] Y. Liu, M. Yue, Y. Guo, Y. Jiang, Y. Sun, L. Feng, Y. Wang, *J. Magnesium Alloys* **2025**, *13*, 1232.
- [243] Z. Li, M. Gao, S. Wang, X. Zhang, P. Gao, Y. Yang, W. Sun, Y. Liu, H. Pan, *Chem. Eng. J.* **2022**, *433*, 134485.
- [244] T. J. Udovic, M. Matsuo, A. Unemoto, N. Verdal, V. Stavila, A. V. Skripov, J. J. Rush, H. Takamura, S.-i. Orimo, *Chem. Commun.* **2014**, *50*, 3750.
- [245] X. Wang, X. Xiao, J. Zheng, X. Huang, M. Chen, L. Chen, *Int. J. Hydrogen Energy* **2020**, *45*, 2044.
- [246] J. Zheng, X. Wang, X. Xiao, H. Cheng, L. Zhang, L. Chen, *Chem. Eng. J.* **2021**, *412*, 128738.
- [247] A. Xia, J.-G. Zheng, Q.-B. Zhang, Y.-G. Shu, C.-G. Yan, L.-T. Zhang, Z.-L. Tao, L.-X. Chen, *Rare Met.* **2024**, *43*, 4387.
- [248] Z. Zhang, D. Gao, J. Zheng, A. Xia, Q. Zhang, L. Wang, L. Zhang, *Chem. Eng. J.* **2023**, *460*, 141690.
- [249] K. Bohmhammel, U. Wolf, G. Wolf, E. Königsberger, *Thermochim. Acta* **1999**, *337*, 195.
- [250] H. Shao, Y. Wang, H. Xu, X. Li, *J. Solid State Chem.* **2005**, *178*, 2211.
- [251] F. C. Gennari, F. J. Castro, *J. Alloys Compd.* **2005**, *396*, 182.
- [252] J. C. Crivello, T. Nobuki, T. Kuji, *Int. J. Hydrogen Energy* **2009**, *34*, 1937.
- [253] L. Z. Ouyang, F. X. Qin, M. Zhu, *Scr. Mater.* **2006**, *55*, 1075.
- [254] F.-g. Meng, H.-s. Liu, L.-b. Liu, Z.-p. Jin, *Trans. Nonferrous Met. Soc. China* **2007**, *17*, 77.
- [255] E. A. Nickels, M. O. Jones, W. I. F. David, S. R. Johnson, R. L. Lowton, M. Sommariva, P. P. Edwards, *Angew. Chem., Int. Ed.* **2008**, *47*, 2817.
- [256] a) J. Yang, A. Sudik, C. Wolverton, *J. Phys. Chem. C* **2007**, *111*, 19134; b) J. Ye, G. Xia, X. Yu, *Mater. Today Energy* **2021**, *22*, 100885.
- [257] Q. He, D. Zhu, X. Wu, D. Dong, M. Xu, Z. Tong, *Molecules* **2019**, *24*, 1861.
- [258] A. H. Dao, *ECS Meet. Abstr.* **2016**, *MA2016-01*, 131.
- [259] A. Nale, M. Catti, E. G. Bardají, M. Fichtner, *Int. J. Hydrogen Energy* **2011**, *36*, 13676.
- [260] K. Tokoyoda, T. Ichikawa, H. Miyaoka, *Int. J. Hydrogen Energy* **2015**, *40*, 1516.
- [261] Z. Xiong, G. Wu, J. Hu, Y. Liu, P. Chen, W. Luo, J. Wang, *Adv. Funct. Mater.* **2007**, *17*, 1137.
- [262] J. Hu, Z. Xiong, G. Wu, P. Chen, K. Murata, K. Sakata, *J. Power Sources* **2006**, *159*, 116.
- [263] A. Sudik, J. Yang, D. J. Siegel, C. Wolverton, R. O. Carter III, A. R. Drews, *J. Phys. Chem. C* **2009**, *113*, 2004.
- [264] W. S. Tang, M. Matsuo, H. Wu, V. Stavila, W. Zhou, A. A. Talin, A. V. Soloninin, R. V. Skoryunov, O. A. Babanova, A. V. Skripov, *Adv. Energy Mater.* **2016**, *6*, 1614.
- [265] L. Zeng, T. Ichikawa, K. Kawahito, H. Miyaoka, Y. Kojima, *ACS Appl. Mater. Interfaces* **2017**, *9*, 2261.
- [266] X. Zhuang, H. Chen, S. He, L. Hu, H. Wang, R. Hu, *Mater. Adv.* **2024**, *5*, 4131.
- [267] Z. Wu, K. Wang, W. Sun, Z. Li, Z. Ma, Y. Zhu, Y. Zou, Y. Zhang, *Adv. Funct. Mater.* **2022**, *32*, 2205677.
- [268] Y. S. Choi, Y.-S. Lee, D.-J. Choi, K. H. Chae, K. H. Oh, Y. W. Cho, *J. Phys. Chem. C* **2017**, *121*, 26209.
- [269] S. Zeng, M. Zhao, C. Xie, J. Li, X. Ding, L. He, Y. Li, Q. Zhang, H.-W. Li, *Inorg. Chem. Front.* **2024**, *11*, 3323.
- [270] Y. Lv, X. Zhang, W. Chen, S. Ju, Z. Liu, G. Xia, T. Ichikawa, T. Zhang, X. Yu, *J. Mater. Sci. Technol.* **2023**, *155*, 47.
- [271] L. M. De Kort, J. Harmel, P. E. De Jongh, P. Ngene, *J. Mater. Chem. A* **2020**, *8*, 20687.
- [272] T. Scheiber, B. Gadermaier, K. Hogrefe, R. Zettl, H. M. R. Wilkening, *Chem. Mater.* **2023**, *35*, 10504.

- [273] Y. Wei, Z. Li, Z. Chen, P. Gao, Q. Ma, M. Gao, C. Yan, J. Chen, Z. Wu, Y. Jiang, *ACS Nano* **2024**, *18*, 5965.
- [274] C. Zhou, Y. Yan, T. R. Jensen, *ACS Appl. Energy Mater.* **2023**, *6*, 7346.
- [275] S. Yang, H. Wang, L. Ouyang, J. Liu, M. Zhu, *Inorganics* **2017**, *6*, 2.
- [276] T. J. Udovic, M. Matsuo, A. Unemoto, N. Verdál, V. Stavila, A. V. Skripov, J. J. Rush, H. Takamura, S.-i. Orimo, *Chem. Commun.* **2014**, *50*, 3750.
- [277] E. Roedern, R.-S. Kühnel, A. Remhof, C. Battaglia, *Sci. Rep.* **2017**, *7*, 46189.
- [278] K. Kisu, S. Kim, M. Inukai, H. Oguchi, S. Takagi, S.-i. Orimo, *ACS Appl. Energy Mater.* **2020**, *3*, 3174.
- [279] P. Dansirima, L. G. Kristensen, J. B. Grinderslev, J. Skibsted, R. Utke, T. R. Jensen, *Commun. Mater.* **2024**, *5*, 160.
- [280] M. B. Amdisen, J. B. Grinderslev, L. N. Skov, T. R. Jensen, *Chem. Mater.* **2023**, *35*, 1440.
- [281] Q. Wang, H. Li, R. Zhang, Z. Liu, H. Deng, W. Cen, Y. Yan, Y. Chen, *Energy Storage Mater.* **2022**, *51*, 630.
- [282] S. Zhong, S. Ju, Y. Shao, W. Chen, T. Zhang, Y. Huang, H. Zhang, G. Xia, X. Yu, *J. Energy Chem.* **2021**, *62*, 431.
- [283] P. Gao, S. Ju, Y. Huang, G. Xia, D. Sun, X. Yu, *Small Struct.* **2024**, *5*, 2300365.
- [284] F. Cano-Banda, A. Gallardo-Gutierrez, L. Luviano-Ortiz, A. Hernandez-Guerrero, A. Jain, T. Ichikawa, *Int. J. Hydrogen Energy* **2021**, *46*, 1030.
- [285] S. Ikeda, T. Ichikawa, K. Kawahito, K. Hirabayashi, H. Miyaoka, Y. Kojima, *Chem. Commun.* **2013**, *49*, 7174.
- [286] Y. Chen, A. Inoishi, S. Okada, H. Sakaebe, K. Albrecht, *J. Energy Storage* **2024**, *86*, 111286.



**Panyu Gao** received his B.S. degree from Hebei University of Technology in 2019 and his M.S. degree from Fudan University in 2021. He is currently a Ph.D. candidate at Fudan University under the supervision of Prof. Xuebin Yu and Prof. Guanglin Xia. His research focuses on the development and synthesis of hydride-based electrolytes and electrodes for application in all-solid-state lithium-ion batteries.



**Xiaoyue Zhang** received her B.S. degree from Southwest University in 2020. She is currently pursuing her Ph.D. in the Department of Materials Science at Fudan University under the supervision of Prof. Xuebin Yu and Prof. Guanglin Xia. Her research interests focus on light-weight solid-state hydrogen storage materials.



**Xuechun Hu** received her B.S. degree from Soochow University in 2021. She is currently a Ph.D. student in the Department of Materials Science at Fudan University under the supervision of Prof. Fang Fang and Prof. Guanglin Xia. Her research focuses on external field-driven techniques and the kinetic modification of Mg-based solid hydrogen storage materials.



**Xuebin Yu** is a professor in the Department of Materials at Fudan University. He received his Ph.D. from the Shanghai Institute of Microsystem and Information Technology, Chinese Academy of Sciences, in 2004. His research interests include hydrogen storage, hydride-based solid-state electrolytes, secondary ion batteries, and nanomaterials for energy storage.



**Dalin Sun** is a professor in the Department of Materials Science at Fudan University. He received his Ph.D. in materials science and engineering from Zhejiang University in 1992. His research focuses on hydrogen and electrochemical energy storage materials, as well as advanced characterization techniques, including neutron diffraction and synchrotron radiation.



**Fang Fang** is a professor in the Department of Materials Science at Fudan University. He earned his Ph.D. in materials science from Fudan University in 2009 and subsequently joined the faculty. His research interests encompass both fundamental studies and industrial applications of new energy storage materials, with a particular emphasis on hydrogen storage materials and secondary ion batteries.



**Guanglin Xia** is a professor in the Department of Materials Science at Fudan University. He received his Ph.D. from the University of Wollongong in 2015 and subsequently worked as a postdoctoral fellow there from 2016 to 2018. His research interests include solid-state hydrogen storage materials and electrochemical energy storage technology.